2014

Modification of Plasmonic Nano Structures' Absorption and Scattering Under Evanescent Wave Illumination Above Optical Waveguides or With the Presence of Different Material Nano Scale Atomic Force Microscope Tips

Gazi Mostafa Huda
University of Kentucky, sumit128@gmail.com

Recommended Citation

Huda, Gazi Mostafa, "Modification of Plasmonic Nano Structures' Absorption and Scattering Under Evanescent Wave Illumination Above Optical Waveguides or With the Presence of Different Material Nano Scale Atomic Force Microscope Tips" (2014). *Theses and Dissertations--Electrical and Computer Engineering*. Paper 43.
http://uknowledge.uky.edu/ece_etds/43

STUDENT AGREEMENT:

I represent that my thesis or dissertation and abstract are my original work. Proper attribution has been given to all outside sources. I understand that I am solely responsible for obtaining any needed copyright permissions. I have obtained and attached hereto needed written permission statement(s) from the owner(s) of each third-party copyrighted matter to be included in my work, allowing electronic distribution (if such use is not permitted by the fair use doctrine).

I hereby grant to The University of Kentucky and its agents the irrevocable, non-exclusive, and royalty-free license to archive and make accessible my work in whole or in part in all forms of media, now or hereafter known. I agree that the document mentioned above may be made available immediately for worldwide access unless a preapproved embargo applies. I retain all other ownership rights to the copyright of my work. I also retain the right to use in future works (such as articles or books) all or part of my work. I understand that I am free to register the copyright to my work.

REVIEW, APPROVAL AND ACCEPTANCE

The document mentioned above has been reviewed and accepted by the student's advisor, on behalf of the advisory committee, and by the Director of Graduate Studies (DGS), on behalf of the program; we verify that this is the final, approved version of the student's dissertation including all changes required by the advisory committee. The undersigned agree to abide by the statements above.

Gazi Mostafa Huda, Student

Dr. J. Todd Hastings, Major Professor

Dr. Cai-Cheng Lu, Director of Graduate Studies

MODIFICATION OF PLASMONIC NANO STRUCTURES' ABSORPTION AND SCATTERING UNDER EVANESCENT WAVE ILLUMINATION ABOVE OPTICAL WAVEGUIDES OR WITH THE PRESENCE OF DIFFERENT MATERIAL NANO SCALE ATOMIC FORCE MICROSCOPE TIPS

Dissertation

A dissertation submitted in partial fulfillment of the requirements
for the degree of Doctor of Philosophy in the College of Engineering
at the University of Kentucky

By

Gazi M. Huda

Lexington, Kentucky

Director: Dr. J. Todd Hastings, Gill Associate Professor
Electrical Engineering

Lexington, Kentucky

2014

Abstract of Dissertation

The interaction of an evanescent wave and plasmonic nanostructures are simulated in Finite Element Method. Specifically, the optical absorption cross section (C_{abs}) of a silver nanoparticle (AgNP) and a gold nanoparticle (AuNP) in the presence of metallic (gold) and dielectric (silicon) atomic force microscope (AFM) probes are numerically calculated in COMSOL. The system was illuminated by a transverse magnetic polarized, total internally reflected (TIR) waves or propagating surface plasmon (SP) wave. Both material nanoscale probes localize and enhance the field between the apex of the tip and the particle. Based on the absorption cross section equation the author was able to demonstrate the increment of absorption cross section when the Si tip was brought closer to the AuNP, or when the Si tip apex was made larger. However, the equation was not enough to predict the absorption modification under metallic tips, especially for a AgNP's C_{abs}; neither it was possible to estimate the optical absorption based on the localized enhanced field caused by a gold tip. With the help of the driven damped harmonic oscillator equation, the C_{abs} of nanoparticles was explained. In addition, this model was applicable for both TIR and Surface Plasmon Polaritons illuminations. Fitting the numerical absorption data to a driven damped harmonic oscillator (HO) model revealed that the AFM tip modifies both the driving force (F_0), consisting of the free carrier charge and the driving field, and the overall damping of the oscillator (β). An increased F_0 or a decreased β will result in an increased C_{abs} and vice versa. Moreover, these effects of F_0 and β can be complementary or competing, and they combine to either enhance or suppress absorption. Hence, a significantly higher β with a small increment in F_0 will result in an absorption suppression. Therefore, under a Si tip, C_{abs} of a AuNP is enhanced while C_{abs} of a AgNP is suppressed. In contrast, a Au tip suppresses the C_{abs} for both Au and Ag NPs. As an extension of this absorption model, further investigation of the guided mode and a close by nanostructure is proposed, where the scattered wave off the structure attenuates the guided mode with destructive interference.

Keywords: Nano particle, optical waveguide, atomic force microscope tip, nano plasmonics, computational electromagnetic methods.

Gazi M. Huda

Author

December 3rd, 2013

Date

MODIFICATION OF PLASMONIC NANO STRUCTURES' ABSORPTION AND SCATTERING UNDER EVANESCENT WAVE ILLUMINATION ABOVE OPTICAL WAVEGUIDES OR WITH THE PRESENCE OF DIFFERENT MATERIAL NANO SCALE ATOMIC FORCE MICROSCOPE TIPS

By

Gazi M. Huda

Dr. J. Todd Hastings

Director of Dissertation

Dr. Cai-Cheng Lu

Director of Graduate Studies

December 3rd, 2013

Date

To all my S&Ss
Shawon, Shama, Shuvo, and Swad

When the oppressed people's wail on the sky and air will not resound
The tyrant's dreadful sword will not flash on the battle ground
I, the Rebel, tired of battle, shall be quite on that day.

....Kazi Nazrul Islam

Acknowledgements

What appeared to be a far-fetched possibility only a few years ago is now a reality within a touching distance. It has been an honor to be a part of the University of Kentucky, and to work in the Electrical and Computer Engineering Department. In pursuit of this accomplishment, a few great people encouraged me not only to push further the frontier of science and engineering, but also to be a better individual.

I take tremendous pride in having Prof. Todd Hastings as my mentor. He consistently maintained an extremely productive environment in the lab, and led by his own word and deeds. My heartiest gratitude to him for the stimulating intellectual discussions, endless inspiration to complete this astronomical task in time, generous graduate assistantship support, and numerous letters of recommendation. He is and will always be my role model.

Prof. Stephen Gedney has been an outstanding motivation throughout my graduate career. I greatly appreciate him advising my research as well as his availability outside of the classroom. Thanks to Profs. Pinar Mengüç and Janet Lumpp for being part of my PhD advisory committee and for their invaluable guidance. It has been an exciting and rewarding experience learning from you.

My success would have never been possible without the splendid support from my parents Dr. Gazi Shamsul Huda and Sufia Khatun, who trusted me with my dreams and aspirations. I am deeply grateful for my loving wife Sabrina Hussain and her willingness to set aside her career for my graduate studies, and endless help in reaching this milestone. I am indebted to my siblings Gazi Saiful Huda, and Drs. Sharmila Huda and Shanjida Huda for believing in me. I would also like to take this opportunity to acknowledge the moral support from my in-laws. Thanks to Almighty for blessing me with such a great family and to provide me with the strength, wisdom, and courage to achieve my long cherished goal.

I am very fortunate to be a graduate from Bangladesh University of Engineering Technology and from Mirzapur Cadet College. These two great institutions have equipped me with world-class education and gifted me with lifetime friends around the world. Having colleagues and friends such as Drs. Carlos Jarro and Neha Nehru, have made this adventure many times easier. Not only have they shared experimental expertise, but also have made lunch times much more pleasant. Thanks to Drs. Eugene Donev and Matthew Bresin for their advice and encouragement. I would like to acknowledge the help from Amber Troxell for proofreading this dissertation. Last but not the least, this work would not have been possible without the generous support from the National Science Foundation of Grant No. CMMI-0800658.

TABLE OF CONTENTS

LIST OF TABLES

LIST OF FIGURES

Chapter 1

Introduction

With the relentless efforts of the scientists, nanotechnology is currently at the edge of the atomic scale. According to the physicists' predictions, if Moore's law [1] really falters within a decade, nanotechnology may have the answer for further miniaturization. Soon chemists might be able to order any chemical structure they want by manipulating single atoms. It might even be possible to insert nano machines in our bodies which can be controlled by the external electric signals and locate the cancer cells to destroy them cleanly, avoiding the side effects of conventional chemotherapy. Particularly, the nanoparticles between 10 to 100 nm can deliver medicine more effectively. As Kaku depicted in his book, these particles can safely bounce off of the blood cells because of their large sizes and can penetrate the irregular pores of the cancerous cells [2].

Breaking the diffraction limit of light has resulted in microscopy with extremely high resolution [3] and in super dense data storage [4]. As early as 1928, E. H. Synge first proposed the concept of near field optical microscopy, where the detector is placed very close to the object and the resolution is limited by the numerical aperture and not by the wavelength [5]. Over the years, many techniques were developed to confine light in the nanoscale and to use it for different imaging purposes, such as scanning probe microscope, scanning tunneling microscope, and near-field reflection microscope. Many of these techniques rely on the enhanced field at the apex of a sharply pointed metal tip. Atomic Force Microscope (AFM) is one of the most popular imaging tools and is widely used for imaging samples with resolution as high as a few nanometers. Our group's recent work using a nanoscale tip to locally modify nanoparticles [6] led the author to merge these lines of investigation and to study the effects of a nanoscale tip in proximity to a metal nanoparticle on a substrate.

Material size can influence the optical properties of nanoparticles, where a small modification to the shape or to the surrounding medium affects the optical response. For a specific size, shape, geometric setup, and illumination condition, a specific material will absorb and/or scatter a significantly higher optical energy compared to the rest of the materials present in that sample. For sensing applications, the general idea is to facilitate biomolecule attachment to the metallic nanostructures. Depending on specific molecular characteristics, the scattered signal off the nanostructure is detected to identify the molecular signature. As Figure 1.1 shows, however, the sensing takes bulk optics components to analyze the scattered signal. For example, Raman scattering is a weak signal, and needs significant enhancement for accurate detection. This mechanism requires a large optical setup.

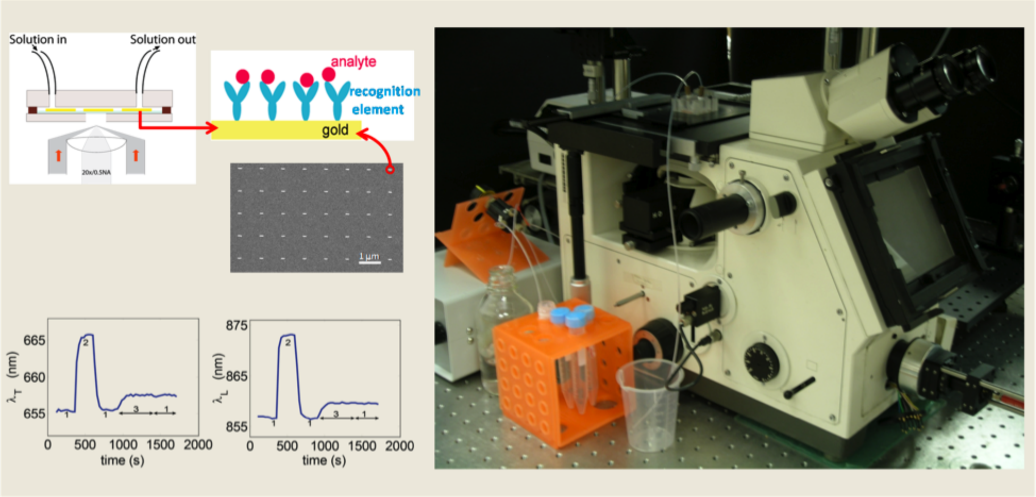

Figure 1.1: General description of the current technology for detection. For this example, a gold nanorod array is used on which the solution to be investigated is flowing. The scattered light is collected through the dark field objective, as is drawn on the top left corner segment. In the adjacent segment, where the analyte is bound with the recognition element, the detected scattered signal experiences a shift, depending on the refractive index variation caused by the binding of the analyte. The photograph on the right shows the experimental setup used in this process, which consists the sample (inside the flow-cell) and the microscope. Although the spectrometer and the camera are not included in this photograph, the intention is to show the untransportable components of traditional sensing techniques. Figure courtesy of Neha Nehru.

Waveguides are an essential component for integrated optics. The intricacies of light propagation at different modes through optical fibers have been thoroughly studied over last few decades [7]. From a biomedical standpoint, sensing plays a major role in accurate detection of biomolecules through attachment to metallic structures, such as nanoparticles or nano rods [8]. One of the widely used techniques that the scientific community uses is Raman Scattering. For decades, scattering techniques have been used to detect the existence of specific materials in a given sample. Since many biomolecules have a natural affinity to attach with gold or silver, scientists and engineers have mastered the usage of nanoparticles (along with nanorods, nanodisks, and nanoshells) to accurately "sense" certain types of biomolecules. Furthermore, along with the scattering mechanism, nanostructures also absorb optical energy.

In the fast growing field of nanophotonics, chemical detection and biomolecule sensing play major roles in terms of application. Different spectroscopies depend largely on one primary phenomena: measuring the change in the permittivity by looking at the altered electric field, caused by the introduction of the biological agent [9]. Using the same principle, optical waveguides sensors have been developed over the last decade for monitoring environmental pollution and industrial processes. In general, the evanescent wave of the waveguide is used to detect perturbation of the electromagnetic waves of a guided mode caused by optical absorptions, fluorescence, or refractive index change of measurands [10]. One can build antennas at optical frequencies to couple electromagnetic waves into and out of optical waveguides as well. For example, a nanostructure placed in the evanescent field of a guided mode can act as such an antenna. These structures can simultaneously serve as sensors in which changes in dielectric constant are detected by the efficiency of with which power in the waveguide is absorbed and/or scattered. As Figure 2.1 shows, the advantage of using nano shells is that one can tune the resonant frequency by the ratio of the radii of the core and the shell in a wide frequency range [11].

There have been many attempts to study and understand the behavior of nanoparticles in numerous different conditions. Motivating applications range from communication, computing, and data storage to medical diagnostics and therapies. The enhanced absorption, scattering, and electric fields associated with nanoparticles' localized surface plasmon resonances find application in information processing [12], sensing [13], microscopy [6, 14], lithography [15, 16], materials processing [6, 17, 18], optical sources and detectors, and photovoltaics [19]. In many of these applications, nanoparticles are immobilized on substrates that strongly influence their optical behavior [15, 16]. In addition, several studies have been conducted on the optical properties of nanoscale probes or tips [14, 20, 21]. These have largely addressed applications in near-field microscopy and enhanced Raman scattering [22, 23] and have focused on metal or metal-coated tips.

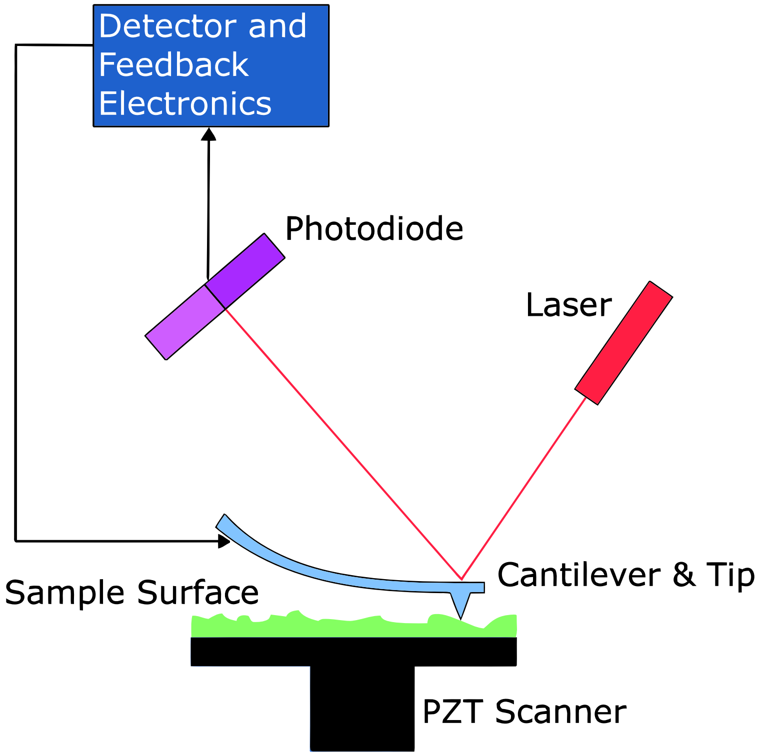

Figure 1.2: Operational diagram of an Atomic Force Microscope (AFM). Force between the cantilever and sample lead to a deflection [24].

This dissertation focuses primarily on how the light interacts with a nanostructure. With regard to the noble metals, the most exciting phenomena at nanoscale are the size and shape dependent properties, because the dominant physical phenomena change from scale to scale. A gold nanoparticle, for example, will not melt as a bulk piece of gold; its color would be different, and even the thermal expansion would not be the same. The significance of noble metals lies on the fact that these metals can accommodate surface plasmon, a special optical property. With the ultra-fast computation power developed in last few decades, the study of these optical properties for numerous different applications has been possible.

Experimentally, like many other groups, ours has been interested in understanding the interaction of an AFM tip with nanoparticles. AFM is widely used for nano patterning (e.g. scratching), and in manipulation, imaging and measurement of nanoparticles. Using its precise control, AFM can be used to repair photomask. AFM can also be used as a Scanning Near-field Optical Microscopy (SNOM), where the tip apex works as a light source or scatterer, and can be used to remove material from a sample in a controlled way. To store data, IBM has used multiple heated

AFM tips to write (scratch), read (image), erase (melt) data (nano holes) on a very thin polymar film [25]. This research, however, has been focused more on selective heating, melting, evaporation and deposition of nanoparticles on a substrate. The general idea is to bring a very sharp nanoscale probe [26], shown in Figure 1.2, close to the nanoparticle(s) to sense the topography and to create an enhanced field around the nanoparticle. This setup gives rise to effective and important changes in different aspects of nanoparticles, such as Localized Surface Plasmon Resonance (LSPR), enhanced Raman scattering, and greater extinction cross section. Typically, the probes are metallic, metal coated, or dielectric, causing the localization of the electric field around the apex. The advantage of AFM over Scanning Tunneling Microscope (STM) is that STM needs a conducting surface in a vacuum environment; whereas, AFM can be performed on both conducting and non conducting surfaces at room environment [25]. Analytically, it is difficult to quantify the interaction between the probe and the particle with respect to the absorption, scattering, change of resultant field, etc. Hence, it is imperative to numerically simulate the interaction of nanoparticles with the AFM probe to gain insight into the fundamental physics taking place, especially in the context of our group's experimental experience [6].

Most commonly, the particle is assumed to be spherical. Although particles have different facets in their topography, a sphere is the closest shape and can be assumed in a given sample or solution. Furthermore, section 2.11 discusses a sphere being the most thermodynamically stable shape. By having the analytical solution of Lorenz-Mie, as stated in [27], simulating a spherical particle is easier geometrically and provides a good starting point. As is shown in Figure 1.3, the effects of a dielectric or metal tip on the absorption cross section (C_{abs}) and electric field enhancement of different sized and different material nanoparticles resting on a BK7 glass or gold substrate are investigated in this report. Additionally, how the presence of a tip changes the frequency of the LSPR of nanoparticles is investigated. Wave illumination originates from below the AuNP under total internal reflection (TIR) conditions or through surface plasmon polaritons. Both transverse electric (TE) and transverse magnetic (TM) excitations are considered, and the tip is suspended 5 nm above the particle.

This dissertation will show that a high dielectric constant tip can selectively enhance nanoparticle absorption at length scales far below the diffraction limit of light, whereas a metal tip may enhance or suppress the absorption of the particle. In addition, this research will show that polariza-

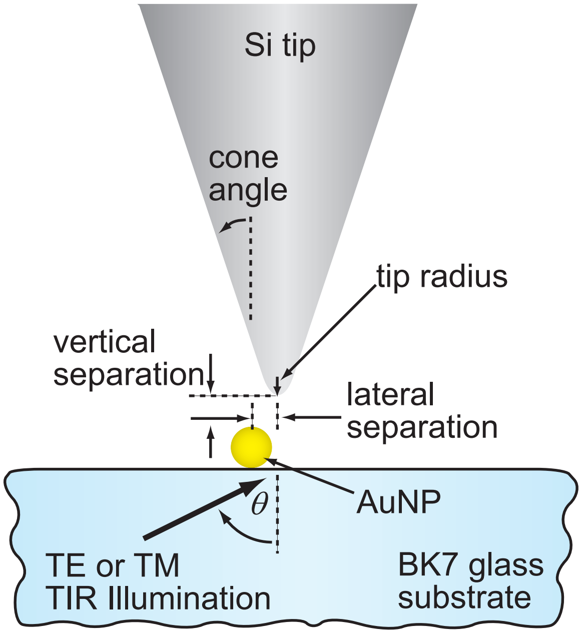

Figure 1.3: Cross-sectional schematic of the geometry of interest. A silicon (Si) tip (length =370 nm, radius= 10 nm, cone angle = 10°), is illuminated at an angle, θ of 50° with total internal reflection (TIR) illumination.

tion and material influence the effect of the tip on the particle. Apart from that, this dissertation will project on the connection of the absorption cross section with the temperature and shape modification. In two parallel works, this report includes the benchmarking of Discrete Dipole Approximation with Surface Interaction (DDA-SI) with Finite Element Method (FEM), and the simulation of LSPR Sensors for an enhanced performance.

As a continuation the author intends to combine the study of electromagnetic wave propagation inside of an optical waveguide along with nanoparticle optical absorption to devise compact and reliable sensors. This sensor would be easy to use and should alleviate the usage of bulk optical components. The key point of this investigation is to capture the refractive index change near the nanostructure by looking at the output light of the waveguide.

The first three chapters of this dissertation include a brief introduction, relevant background, and the status of the contemporary research. Chapters four and five describe the detailed simulation setup, geometry, formulation, and validation with respect to different standards. These are followed by obtained results and necessary discussions in chapter six. The last chapter is dedicated to the notable conclusions and future works.

Chapter 2

Background Information

This chapter introduces some core concepts directly relevant to this dissertation.

2.1 Electromagnetic fields

In the context of this investigation, a field means a function of time and three dimensional space. An electric field can be produced by a static charged particle, and a magnetic field is generated by a moving charge, more commonly viewed as a current. Both of these field components affect any charged particle nearby as well as interact with each other. According to classical physics, electromagnetic radiation carries energy from the source in a continuous wave like nature, where electric and magnetic field components are at a fixed ratio of intensity, oscillating in phase, and perpendicular to the direction of propagation. According to the discrete structure, electromagnetic energy can be viewed as a transportation of packets, more commonly known as photon, with a fixed frequency. The behavior of electric and magnetic field in vacuum is governed by Maxwells equations. Although there are equivalent integral forms, here only the differential forms are listed:

$$\nabla \times \mathbf{E} = -\frac{\partial \mathbf{B}}{\partial \mathbf{t}} \text{ (Faraday)}, \tag{2.1}$$

$$\nabla \times \mathbf{H} = \frac{\partial \mathbf{D}}{\partial \mathbf{t}} + \mathbf{J} \text{ (Maxwell − Ampere)}, \tag{2.2}$$

$$\nabla \cdot \mathbf{B} = \mathbf{0} \text{ (Gauss − magnetism), and} \tag{2.3}$$

$$\nabla \cdot \mathbf{D} = \rho \text{ (Gauss)}. \tag{2.4}$$

Where

$\mathbf{B}$ = the magnetic flux density (Wb/m^2)

$\mathbf{D}$ = the electric flux density (C/m^2)

$\mathbf{E}$ = the electric field intensity (V/m)

$\mathbf{H}$ = the magnetic field intensity (A/m)

ρ =charge density (C/m^3),

ϵ_0 = permittivity of free space, 8.854 $\times 10^{-12}$ F/m , and

$\mathbf{J}$ = current density vector (A/m^2) [28].

For these expressions to be valid, it is assumed that the fields are single valued, bounded, and continuous functions of both time and space, and exhibit continuous derivatives. The linearity of these equations allow the Fourier transform of these equations to express them in frequency domain. Although non linearity rarely occurs in electromagnetic problems, the effects are amplified with smaller wavelengths (i.e. at higher frequencies) [29]. Most of the problems addressed in this dissertation are formulated using Maxwells equations. Below are brief explanations of these individual equations:

2.1.1 Maxwell-Faraday equation

Equation 2.1 states that a time varying magnetic field is always associated with a spatial varying electric field. This spatial variation, as captured by the curl operator, projects the results in orthogonal direction that can be detected by right hand rule (i.e. thumb would indicate the direction while aligning the remaining fingers with the field lines). The negative sign indicates that the induced electric field, when acting on charge, would produce a current that opposes the change in magnetic flux, also referred to as Lenz's law.

2.1.2 Ampere's circuital law

Equation 2.2 relates the magnetic field with current. Here, $\mathbf{J}$ includes the magnetization, polarization, and conduction current densities. The lines of $\mathbf{D}$ starts from positive charge, and ends in negative charge. Another important connection denoted by this equation is that the source of magnetic field can be a free current source, $\mathbf{J}$ or a displacement current $\dfrac{\partial \mathbf{D}}{\partial t}$ that associates with the variation of electric field and not with the moving charges.

2.1.3 Gauss law

Equation 2.4 indicates that the total outward normal flux coming out of a given volume is proportional to the charge densities enclosed by that volume. In this equation, the gradient operator determines if a given points acts as a source or a sink. Therefore, having a zero gradient value implies having zero "outgoing" normal flux. The result should always be a scalar.

2.1.4 Gauss law for magnetism

Equation 2.3 means that no total "magnetic charge" can build up in any space. In other words, there is no such thing as magnetic monopoles in nature. Therefore there are no source or sinks for the $\mathbf{B}$ lines to start or finish, hence $\mathbf{B}$ field lines are closed [30].

2.1.5 Boundary conditions

These fields and flux densities are subject to boundary conditions. A current and charge free boundary surface s, separating two regions 1 and 2, will obey the following boundary conditions:

$$\hat{n} \times (\mathbf{E}_1 - \mathbf{E}_2)|_{\mathrm{s}} = \mathbf{0}, \tag{2.5}$$

$$\hat{n} \times (\mathbf{H}_1 - \mathbf{H}_2)|_{\mathrm{s}} = \mathbf{0}, \tag{2.6}$$

$$\hat{n} \cdot (\mathbf{D}_1 - \mathbf{D}_2)|_{\mathrm{s}} = \mathbf{0}, \text{and} \tag{2.7}$$

$$\hat{n} \cdot (\mathbf{B}_1 - \mathbf{B}_2)|_{\mathrm{s}} = \mathbf{0}, \tag{2.8}$$

where,

$n =$ the unit vector [31].

Only two sets boundary conditions are sufficient, but they are not arbitrary. Section 4.3 will describe how these boundary conditions are utilized.

2.2 Polarization

For this dissertation, the polarization is determined with respect to the optical plane. In most of the cases, the transverse electric (TE) or transverse magnetic (TM) polarization can be understood by looking into the plane of symmetry, which is defined by the plane that contains the axis of the cone and the propagation vector. With regard to Figure 1.3, for TE/TM polarization, the electric/magnetic field is orthogonal to the cross sectional plane. Since most of the geometries in this dissertation are drawn in x-y plane, for the convenience of the readers who are more familiar with different notation, a comparison is shown in Table 2.1. For those geometries, $\mathrm{H_z} = 0$ for TE modes, and $\mathrm{E_z} = 0$ for TM modes.

Table 2.1: Comparison of different polarization notation, for a geometry, drawn in the x-y plane.

Notation commonly used by computational electromagnetic community	Notation used in this dissertation	Equivalent experimental notation
$\mathrm{TE_z}$	TM	p (parallel)
$\mathrm{TM_z}$	TE	s (from German “senkrecht”)

The only exception will be Figure 4.4, where the geometry is in the x-z plane, but the reader may understand the polarization as it previously described. Although waveguides support hybrid modes, often one component dominates others to act as a quasi-TE or quasi-TM.

When an electromagnetic field interacts with a rough metallic surface, the localized field is enhanced relative to the incident field. Primarily, there are two reasons for this:

- Lightning rod effect due to the charge accumulation at the surface. For example, at a sharp nanoscale tip, there would be a large overlap of field lines, resulting in a strong localized field,
- Amplification of fluorescence and second harmonic generation for thin film, especially when a surface plasmon is excited [9].

2.3 Evanescent wave

At an interface, light will refract depending on the difference of the refractive indices. For a larger difference, the “light bending” will be larger. Critical angle (θ_c) is defined by the incident angle in one medium for which the transmitted angle in an adjacent medium is $90°$. An incident angle higher than the critical angle creates an evanescent wave (EW). For the EW, the energy circulates back and forth giving rise to a zero net flow of energy across the boundary. If the EW interacts with another medium such that the incident wave is partially transmitted, frustrated total internal reflection takes place. The decay length of the EW depends on the surface, and is defined by the distance where the surface field is reduced by 1/e. For a larger angle of incidence, the decay of the wave is faster. From Snell's law, one can derive the critical angle for a glass-air interface, which is $\theta_\text{c} = 41.8°$. As Section 4.3.1 describes, the angle of illumination ($\theta = 50°$) is greater than θ_c for most of the simulations described in this research. The angle in the second medium, air in most cases, is therefore going to be a complex number. It means that the phase of the reflected and transmitted wave will shift relative to the incident wave. Although the polarization remains the same for TE, the TM polarization transforms into an elliptic polarization with the field vector rotating in the plane of incidence [3]. At the interface of the two media, the electric field is strongly enhanced, which peaks at the critical angle of incidence. Researchers have been using this strong field for numerous different studies; Renger et al. e.g. have analyzed the local electric field enhancement of nanosized silver ellipsoids placed in the evanescent field near a glass surface [32]. The study of this dissertation heavily refers to the strong field at the interface of substrate-air. Section 3.3.1 describes a few application examples of evanescent field, and Section 4.3 depicts the formulation used in the simulation setup to excite the evanescent field.

2.4 Optical Waveguide

As the name suggests, optical waveguides guide electromagnetic waves of visible frequencies. A simple waveguide may be made of two parallel lossless mirrors, which is impractical primarily due to the difficulty and fabrication cost of low loss mirrors. The wave launched from one side with any angle should propagate along the direction of the waveguide. Upon each reflection, however, there would be a π phase shift, but the amplitude and polarization would not change. Thus, the phase shift ensures the total field to be zero at the mirror, because the incident and reflected wave would cancel each other [33].

2.4.1 Optical fiber

Today, optical fiber (OF) plays a major role in transferring data over a long distance. With the advent of laser optics, sending information over long range became feasible. The general idea of OF is to surround a high dielectric medium (core) with a low dielectric medium (cladding). Generally, there are two types of OF: step index fibers have step rise and fall of refractive indices as one measures across the diameters, and graded index fibers have sloping increase and decrease across the diameters of the OFs. The light travels through the fiber reflecting off of the core-clad boundary at a super critical angle. As was described in Section 2.3, there is an exponentially decaying wave past the core, which facilitates light coupling into another neighboring waveguide, depending on the propagation constant matching. That is why the cladding needs to be sufficiently thick to prevent any possible cross-talk between adjacent cores. If the clad has an asymmetry in its refractive index, the field will shift toward to the higher index material [33].

The reason OF is discussed in this dissertation is because OF has a strong contribution in making sensors. As was described in the previous paragraph, the evanescent tails coming off the OF core can be used to detect nearby structures, and hence, the change in those nearby structures (e.g. change in permittivity) can be calibrated as a “detection” of a specific material. Moreover, the optical fiber laid the foundation for the on-chip dielectric waveguides on which our sensor design is based.

2.4.2 Material dispersion in optics

The velocity of wave inside a medium depends on the material properties of the media. In general, the phase velocity v_p inside a medium having refractive index *n* is formulated as

$$v_p = \frac{c}{n}, \tag{2.9}$$

where c is the velocity of light in free space. As was described in Section 2.5, the refractive index is a function of frequency. Therefore, v_p depends on the frequency as well. Since the velocity is the multiplication of frequency and wavelength, one can conclude that the wavelength changes as the wave goes from one medium to another.

2.5 Light-matter interaction at different wavelengths

At low frequencies (much smaller than the visible range), the metals are highly reflective; and can be safely used as the cladding layers of the waveguides and resonators for electromagnetic radiation at microwave and far-infrared frequencies. At this "low frequency" regime, most metals approximate good conductors, as most of the impinging waves reflect off of the metal's surfaces. At near-infrared and visible frequencies, however, the penetration depth increases significantly, leading to an increased dissipation. Finally, at ultra violet frequencies, metal acquires dielectric properties, and allows propagation of electromagnetic waves with different attenuation depending on its own band structure.

This report will describe the time harmonic field as $\exp^{\jmath\omega t}$ and the corresponding relative permittivity of the metal. Permittivity (ε) determines the ability of a material to polarize in response to the impinging E field, and thereby reduces the total electric field inside the material. Permittivity is a material's ability to transmit or "permit" electric field and is a complex valued function of frequency, ω:

$$\varepsilon(\omega) = \varepsilon_1(\omega) + \jmath\varepsilon_2(\omega), \tag{2.10}$$

where,

ε_1 = real part of the permittivity, which is related to the stored energy in the corresponding medium, and

ε_2 = imaginary part of the permittivity, where a negative quantity indicates dissipated energy in the corresponding medium (also referred to as loss).

At optical frequencies, the complex refractive index, $\tilde{n}$ can be determined as

$$\tilde{n}(\omega) = n(\omega) + \jmath\kappa(\omega), \tag{2.11}$$

where,

$n(\omega)$ = the real part, relates to the phase speed at the corresponding medium, and

κ = the imaginary part that determines the absorption of an electromagnetic wave, propagating through the medium [34].

From the relation of $\tilde{n} = \sqrt{\varepsilon}$, one can derive

$$\varepsilon_1 = n^2 - \kappa^2, \tag{2.12}$$

$$\varepsilon_2 = 2n\kappa, \tag{2.13}$$

$$n^2 = \frac{\varepsilon_1}{2} + \frac{1}{2}\sqrt{\varepsilon_1^2 + \varepsilon_2^2}, \text{ and} \tag{2.14}$$

$$\kappa = \frac{\varepsilon_2}{2n}. \tag{2.15}$$

This dissertation focuses on the optical response of the noble metals at visible frequencies. In this range of frequencies, the magnetic permeability, $\mu \approx 1$. Similar to the permittivity, permeability defines the material's ability to transmit magnetic field. Since the materials of interest are linear and not Bi-isotropic (i.e. magneto-electric coupled), all of the following studies are focused on the electric field only; such as, how much the incident field would decay, once entered the material.

2.5.1 Skin depth

The skin depth is defined by the distance inside a material from a boundary, where the field is reduced by a factor of 1/e. Table 2.2 lists the skin depth of gold and silver, which are extensively studied in this dissertation.

Table 2.2: Skin depth in nanometers, for selected materials as a function of photon energy [35].

Photon energy, δ	Ag (nm)	Au (nm)
2 eV	24	31
3 eV	29	27
4 eV	82	27

The equation for the intensity as a function of the normal axis of the material boundary states

$$I = I_0 e^{-\gamma z} \tag{2.16}$$

where, the extinction coefficient, $\gamma = 2/\delta$, and

$$\delta = \frac{c}{\omega k} = \frac{\lambda}{2\pi\kappa}.$$

At 273 K, the mean free path of the conduction electron of silver and gold are 52 nm and 42 nm, respectively [35]. These parameters are important because most of the gold and silver nanoparticles investigated in this dissertation are of 50 nm in diameter. The surface electrons of these material geometries play the most significant role of various applications.

2.5.2 Plasmon and plasmonics

Plasmon is the quantized charge density wave often found in plasmas or metals. [36]. In other words, it is the collective oscillation of free electron gas density. Just as photon and phonon are the quantization of electromagnetic and mechanical vibration, respectively, plasmon is a quasiparticle, resulting from the quantization of plasma oscillation. This oscillation occurs around the fixed positive ions in metal [24].

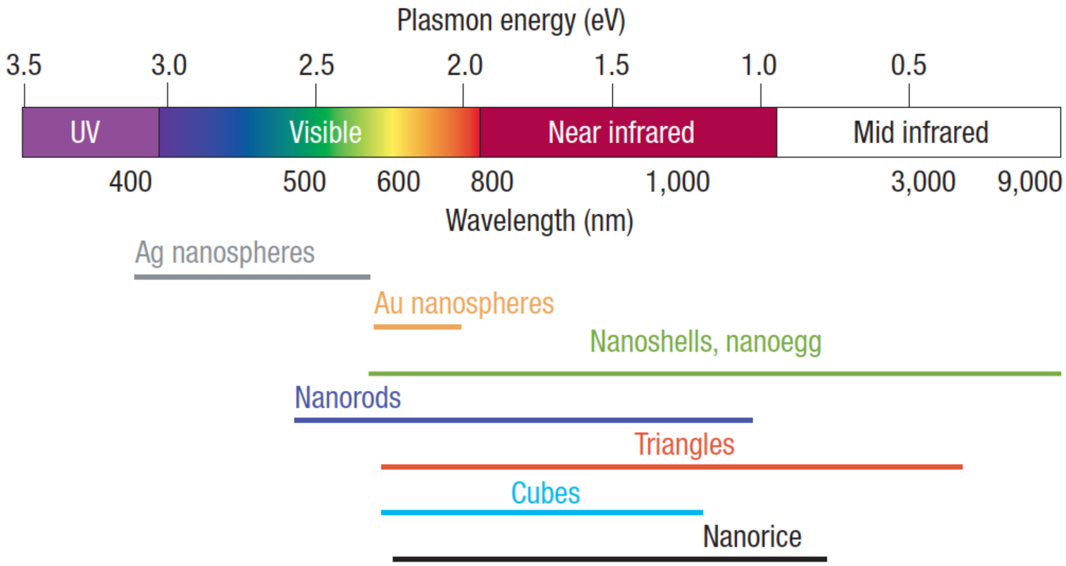

Figure 2.1: Relative position of different shaped nanostructure resonances. Most of the nano structures in this study have resonances at or near visible wavelengths. Reprinted by permission from Macmillan Publishers Ltd: [Nature Photonics] [9], copyright (2007)

Plasmonics or nanoplasmonics is the study of the electromagnetic response of metals, that is the interaction of free or nearly free electrons with light. It is a rapidly growing sub discipline of photonics. Noble metals commonly have one conduction electron per atom, corresponding to a full d band and one electron in s band [37]. Metals having free electrons, such as gold, silver, and copper, show plasmon resonances at visible wavelengths and intense colors. Gold and silver are extensively used for most studies in this dissertation because one can use the standard optics and methods to excite the surface plasmons in these materials [9]. This phenomenon can not be reproduced at other spectral ranges since the material properties change significantly with wavelength. For example, the Drude-Sommerfeld model applies to a few metals at certain wavelengths assuming free electron gas:

$$m_{\mathrm{e}} \frac{\partial^2 \mathbf{r}}{\partial t^2} + m_{\mathrm{e}} \Gamma \frac{\partial \mathbf{r}}{\partial t} = e \mathbf{E}_0 e^{-\jmath \omega t}, \tag{2.17}$$

where,

$\mathbf{r}$ = time dependent electron wave function,

e = charge of the free electrons,

m_{e} = effective mass of the free electrons,

$\mathbf{E}_0$ = amplitude of the applied electric field,

ω = frequency of the applied electric field,

the damping, $\Gamma \propto \frac{\nu_{\mathrm{F}}}{l}$, where,

ν_{F} = Fermi velocity, and

l = electron mean free path between scattering events [3].

Using an educated guess of $\mathbf{r}(t) = \mathbf{r}_0 e^{-\jmath \omega t}$, (2.17) can be solved and one can get:

$$\varepsilon_{\mathrm{Drude}}(\omega) = 1 - \frac{\omega_{\mathrm{p}}^2}{\omega^2 + \jmath \Gamma \omega}, \tag{2.18}$$

where, the volume plasma frequency, $\omega_{\mathrm{p}} = \sqrt{\frac{n e^2}{m_{\mathrm{e}} \varepsilon_0}}$ [38].

One can simplify (2.18) by ignoring Γ, because at high frequency the electrons will undergo many oscillations between each collision. Thus the significance of plasma frequency is understandable: below ω_{p} the corresponding refractive index, $n = \sqrt{\varepsilon}$ becomes complex, and the penetrating wave drops off exponentially from the boundary. Above the ω_{p} the refractive index becomes real, and the material becomes transparent to the incident wave. Along with the description in Section 2.5, one common example is that metals are fairly transparent to X- rays [39]. Table 2.3 shows the free electron density and plasma properties of gold and silver; λ_{p} is the corresponding wavelength to the plasma frequency, ω_{p}. With regard to Figure 2.5, Section 2.5.2 and Figure 2.2 will explain the significance of the threshold energy for inter band transition.

Table 2.3: Threshold energy for inter band transition [35], and free electron density, plasma frequency, and corresponding wavelength of silver and gold [40].

Metal	Threshold energy [eV]	$N(10^{28}m^{-3})$	$\frac{\omega_\mathrm{p}}{2\pi}(10^{15}Hz)$	λ_p nm
Ag	~ 3.89	5.86	2.17	138
Au	~ 2.4	5.90	2.18	138

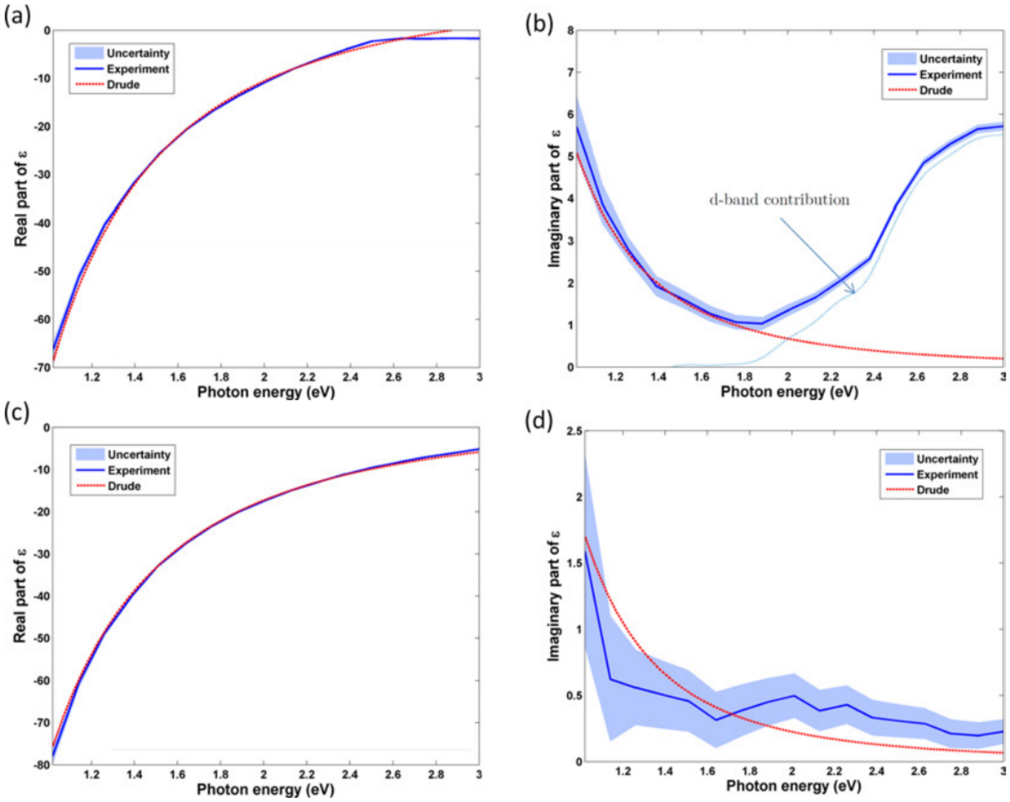

Figure 2.2: Real components of the complex dielectric permittivity of Au and Ag in (a) and (c), and corresponding imaginary components in (b) and (d), respectively. Results for silver are least accurate with an uncertainty in *n* about ±40% of its value. The experimental data, along with the instrumental error, have been taken from Johnson and Christy [37]. Figure courtesy of Andreas Trügler [38].

One can not use the Drude model to predict the material property of gold or silver for all frequencies. This is because above a certain photon energy the inter-band transition takes place, making particularly the imaginary permittivity significantly different than that of the Drude model, as Figure 2.2 shows. This inter band transition is the reason why gold has a distinctive yellowish color. For silver, however, the inter band absorption edge is around 4 eV, as was shown in Table 2.3. Hence, silver remains highly reflective throughout the visible spectrum, and is widely used as a mirror. Gold can be used for mirrors but only at infrared wavelengths [40]. The deviation in Figure 2.2 is more evident for the wavelengths range from 550 nm to 650 nm. That is why this investigation relies on experimental values obtained by Johnson and Christy to interpolate the complex permittivities of gold and silver [37].

Most metals at optical wavelengths (400 - 750 nm) have negative dielectric constants which causes the strong reflection of light. At these optical wavelengths, surfaces can sustain surface charge density oscillations with specific resonant frequencies, named Surface Plasmon Resonances (SPR).

2.5.3 Localized Surface Plasmon Resonance (LSPR)

One could confine the electron oscillation spatially in all three dimensions (3D), resulting in a Localized Surface Plasmon (LSP). LSP arises naturally due to the curved surface of a sub-wavelength metallic nanostructure [34]. Along with the sensing application, surface plasmon waveguides can be used in on chip optical data transfer where the metal structure can be an order of magnitude smaller than the optical fiber [9]. LSP has been widely used in spectroscopy and sensing [41]. The properties of LSP largely depends on the material characteristics, particle geometry (size-shape), and inter particle coupling; leading to a modification of near field enhancement and frequency dependent absorption and scattering. The wet chemical synthesis have made it possible to have a variety of shapes, such as spheres, traingles, prisms, rods and cubes [9]. For an isolated homogenous particle, a gold sphere in this case, charges build up at the surface due to the incident wave. Thus the incident wave induces a dipole moment, proportional to the applied field, and both point in same direction. In a medium with permittivity, ε_{m}, the dipole moment is a measure of the charge system's polarity and defined as:

$$P = \varepsilon_{\mathrm{m}} \alpha E_0 \tag{2.19}$$

where,

ε_{m} = metal permittivity,

E_0 = the applied uniform static electric field, and

the polarizability is defined as:

$$\alpha = 4\pi a^3 \frac{\varepsilon_1 - \varepsilon_2}{\varepsilon_1 + 2\varepsilon_2} \tag{2.20}$$

where,

ε_1 = permittivity of the spherical particle,

ε_2 = permittivity of the surrounding medium, and

a = the radius of the particle [36].

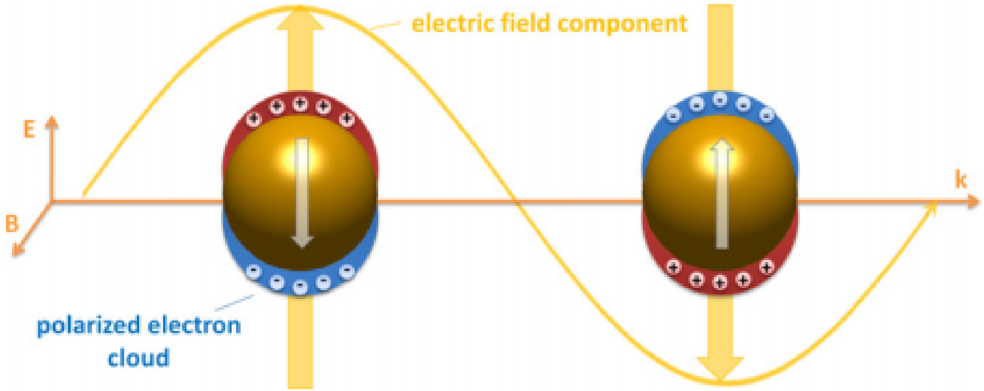

Figure 2.3: Accumulation of charge in response to the applied field in electrostatic approximation (which is more appropriate for smaller particle where all molecules act in unison to the applied excitation) at resonance. As was mentioned in Section 2.5.2, above the resonant frequency, the oscillating electrons will eventually be 180° out of phase of the incident electric field. Figure reproduced with the permission of Andreas Trügler [38].

At a lower frequency (longer wavelength) the electron oscillation is close to being in phase with the incident field wave, as is shown in Figure 2.3. In higher frequency (shorter wavelength), the electron cloud oscillates 180° out of phase. At resonance, the phase difference is approximately 90°. This dissertation discusses in Sections 2.9.2 and 2.9.3 that the initial incident field is distorted by the introduction of the particle, and one can manipulate a number of variables to modify the resultant field. A couple of examples for this manipulation are: changing the frequency of the incident light to change the permittivities of the particle and the surrounding media, and changing the radius of the particle ‘a’ [36]. The resonant condition of LSP in a particle has been explored in this work.

Usually, the spectral position of the resonance is red shifted as the particle gets larger. It can be visualized as due to an increased particle volume, the distance between the opposite interfaces increase; and the corresponding charges realize a smaller restoring force, resulting in a lower resonant frequency. The non radiative decay is due to the creation of electron hole pairs via either intraband excitation at the conduction band or inter band transitions from lower lying d-band to the s-p conduction band in noble metals. As will be shown in Section 2.9.2, for a larger particle, the optical absorption, also known as non radiative decay, does not increase as much as the scattering. Because the larger surface area provides more direct radiative decay route of the coherent electron oscillation into photons, as will be shown in Section 2.6. Despite the reduced absorption efficiency, a significant broadening of plasmon resonance sets in. These two competing damping of radiative and non radiative processes will be explained in details in Section 5.1.2 [34]. When two particles are brought close to each other, so that their scattered field lines overlap with each other, one may find that affecting the individual resonance, such as splitting of the plasmons: one at a lower and another at a higher frequency.

2.5.4 Coupling between localized plasmon

For closely placed particles, where the diameter of the nanoparticles are much larger than the gap between the particles, the near field interaction with a distance dependence of d^{-3} dominates, and the particle array can be understood as an array of point dipoles interacting via the near field. In these cases, the field is localized in nano sized gaps between adjacent particles. The field localization is due to the suppression of scattering into the far field via excitation of plasmon modes in particle along the particle-chain axis. Also, spectral shift of the plasmon resonance will take place, compared to that of isolated particle [34]. As [19] showed, when SP of gold nanoparticle (AuNP) is excited, which are deposited on a semiconductor surface, the optical absorption and photocurrent of the semiconductor is enhanced. Furthermore, as can be seen from Figure 2.9 (b), the nanoparticles can be used as optical antennas to effectively coupling to the semiconductor, increasing its effective absorption cross section [42]. These have the potential to improve the performance of photodetectors and photovoltaics. As an application example of solar cells, Lim et al. found through experimental investigation and Finite Element Method (FEM) simulation that, when gold nanoparticles are deposited on silicon photo diode, the photo current is increased at the wavelengths above the surface plasmon resonance (SPR) of the particle. The electromagnetic amplitude and hence the photo current is actually reduced at the wavelength below the SPR of AuNP [43].

There is also an "unconfined" version of plasmon: a specific type of Polariton.

2.5.5 Surface Plasmon Polariton (SPP)

A Polariton is the coupling between light and charge, in this case coupling between plasmon and photon. A surface plasmon is the coherent electron charge oscillation at the interface of a metal and a dielectric. This surface plasmon oscillation is naturally coupled to Electro Magnetic (EM) waves to give rise to a confined, evanescent EM wave at the interface of a metal and dielectric, which can be exploited to bridge the gap between micro scale optics and the nanoscale structure [36]. At a planar surface the propagating surface plasmon is referred to as a surface plasmon polariton (SPP). The strong interaction between the SPP and the metal surface is widely used in sensors, because a tiny modification of the dielectric of the surrounding media, caused by a specific molecule could significantly alter the evanescent field. Strictly speaking, a SPP propagates at an interface of two materials having real permittivities of opposite sign. An example is given in the Appendix A.1. The fields are maximum at the interface and decay exponentially away from the interface in both of the materials, as is shown in Figure 2.4, corresponding to Figure A.1.1. This decay is faster in metals than in dielectrics and a sizable amount of SPP field can penetrate through a thin enough metal film. Thus, the EM wave can be confined to a much smaller scale than the incident wavelength. This surface mode, however, does not exist for TE polarization. The thickness of the metal layer plays an important role: for a too thin layer, the SPP will be strongly damped due to the radiation damping in the dielectric. Likewise, for a metal layer that is too thick, the absorption inside the metal would cause inefficient excitation of a SPP [3]. Apart from the widely used sensing applications, SPP is used to increase the light trapping of the solar cell, as is shown in Figure 2.9 (c). The advantage of the LSP over the SPP is that it could be used in a much smaller scale. Since the resonance is based upon the surrounding material, as in (2.26), the target material could be as small as a specific kind of molecule [3].

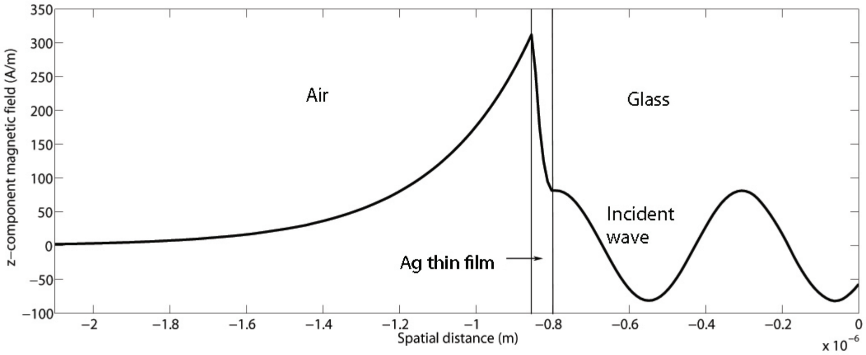

Figure 2.4: Field distribution corresponding to Figure A.1.1 with respect to the distance normal to the Ag film.

Figure 2.4 plots the magnetic field associated with a plane wave, incident from inside glass, striking a 50-nm thick silver film. A surface plasmon polariton is excited at the silver-air interface. The sinusoidal oscillation on the glass side is due to the incident wave. The decay of the field inside metal is notably faster than air. The maximum field is at the interface between metal and dielectric (air) on the opposite side of the film from the incident wave. For a detailed figure of the geometry used for this simulation, refer to Appendix A.1.

As (2.21) indicates, the effective refractive index, n_{eff}, can be large and thus surface-plasmon polaritons (SPP) can travel slowly

$$n_{\mathrm{eff}} = \sqrt{\frac{\varepsilon_{\mathrm{m}}\varepsilon_{\mathrm{d}}}{\varepsilon_{\mathrm{m}} + \varepsilon_{\mathrm{d}}}} \tag{2.21}$$

where, ε_{m} and ε_{d} are the complex valued dielectric constants of metal and dielectric respectively. However, high values of n_{eff} are accompanied by large losses and SPP sometimes travel no more than a few micrometers. In Section 4.3.3, detailed analytic formulation is provided.

The n_{eff} can be very high if ε_{d} is close to -ε_{m}. As is mentioned in (2.18). Since ε_{d} is real, one could attain a resonant condition of $\varepsilon_{\mathrm{d}} = -\operatorname{Re}(\varepsilon_{\mathrm{m}})$ by tuning ε_{m} via changing the frequency. This condition corresponds to the surface plasmon resonance (SPR). Appendix A.2 lists the comparison of LSPR and SPR sensors. All these phenomena, corresponding to the electron oscillation, change the surrounding electric field, which can be quantified in terms of cross sections.

2.6 Interactions between photons and electrons

According to classical physics, photons are the charge-mass less transportation of electromagnetic (EM) energy, whereas electrons are the charged particles that have a specific mass. The associated wavelength of electrons being much smaller than that of photons result in a significantly better resolution of an electron microscope over an optical microscope. In addition, electrons produce a scaler field, where as photons create a vector field; light, for example, is polarized. Electron distribution, possessing a spin, is described by Fermi- Dirac statistics, whereas photon distribution, having no spin, is understood by Bose- Einstein statistics. A quantum description, however, shows many similarities between photons and electrons, as can be seen in Table 2.4 [44]. Confinement of electron and photons to dimensions comparable to their wavelength produces quantization, where only certain discrete values of energy (for photons), and field distribution (for electrons) are permissible. Regions out of these certain values are defined as forbidden zone.

Table 2.4: Similarities in characteristics between photons and electrons. Table reproduced with the permission from Wiley Interscience [44].

Characteristics	Photons	Electrons
Wavelength	$\lambda = \frac{h}{p} = \frac{c}{\nu}$	$\lambda = \frac{h}{p} = \frac{h}{mv}$
Eigenvalue (Wave) equation	$\{\nabla \times \frac{1}{\varepsilon(r)}\nabla\times\}\mathbf{B}(r) = (\frac{\omega}{c})^2\mathbf{B}(r)$	$\hat{H}\Psi(r) = -\frac{\hbar^2}{2m}(\nabla.\nabla + V(r))\Psi(r) = E\Psi$
Free-Space propagation (wave vector)	A real quantity	A real quantity
Interaction potential in a medium	Dielectric constant (refractive index)	Coulomb interactions
Propagation through a classically forbidden zone	Photon tunneling (evanescent wave) with an imaginary wave vector; amplitude decays exponentially in the forbidden zone	Electron tunneling with the amplitude (probability) decaying exponentially in the forbidden zone
Localization	Strong scattering derived from large variations in dielectric constant	Strong scattering derived from a large variation in Coulomb interactions

In this dissertation, the interaction of photons and electrons will be used to explain many optical phenomena of noble metals, such as inter-band transition, nanostructure deformation, and optical interference. Interference is a non-localized phenomenon which can not happen in only one single point in space; rather, it takes place in an extended region of space in a coordinated fashion that leaves the total amount of radiant energy unchanged [39]. The interaction of photons and electrons can be further clarified by Figure 2.5. Section 2.5.3 will discuss this interaction in more details, but the discussion will begin by explaining different kinds of photon emission after excitation.

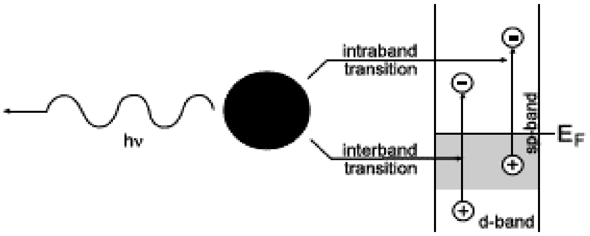

Figure 2.5: Radiative and non radiative decay of particle plasmon. E_{F} indicates the fermi level. Figure reproduced with the permission from Springer [34].

2.7 Raman scattering

A Photon's momentum does not depend upon its speed; rather, it depends on the wavelength and hence, a blue photon has more energy than a red photon [39]. When the photon is incident on an atom or molecule, most likely it will excite and emit another photon of the same energy, as is shown in Figure 2.6. It is possible that some of the emitted photons will be of different energy than the incident photons. This inelastic scattering associated with molecular polarizability is called Raman scattering. George Stokes studied an interim state of atom, where it emits less energy compared to the absorbed energy. Alternatively, for an excited initial state, such as a heated sample, after absorption and reemission, the atom may drop down to a lower state. This is called an anti-Stokes transition. These processes take place in random time intervals and called spontaneous emissions. Apart from this spontaneous Raman scattering, one can excite a stimulated Raman scattering with significant power. Along with the most probable Rayleigh scattering, there are weak additional components of Stokes and anti-Stokes, which appear as side bands in frequency spectrum and are characteristic of the material. Hence, Raman spectroscopy is a unique and powerful analytical tool due to the small sample requirement, spectra details, and environmental sensitivity. Raman scattering is used in biochemistry, chemical manufacturing, environmental detection, and forensics. Since

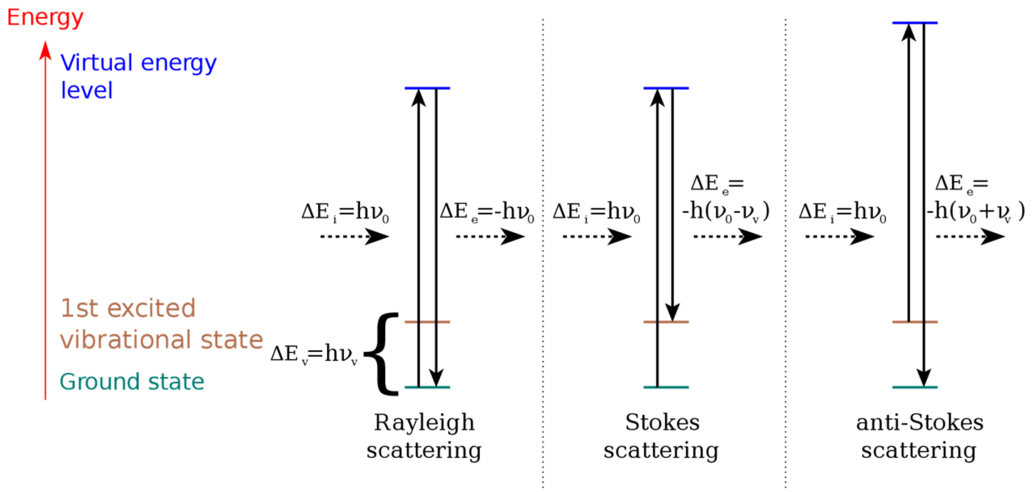

Figure 2.6: Rayleigh and Spontaneous Raman Scattering. Most of the time incident and the emitted photon has the same energy, resulting in the Rayleigh scattering. When the atom or molecule absorbs energy and emits a reduced energy photon, Stokes scattering takes place. Similarly for the anti Stokes scattering, the emitted photon has more energy than the absorbed photon [24].

water does not cause interference, the Raman spectra can be obtained from an aqueous solution as well [39].

The Stokes component (red shift) is temperature independent, but the anti-Stokes component is proportional to the excited state electron population of the material, and thus depends on the temperature. Equation (2.22) shows a direct measurement of temperature [45]:

$$\frac{n_{\mathrm{S}}}{n_{\mathrm{aS}}} \propto \exp\left(\frac{h\Delta\nu}{kT}\right), \tag{2.22}$$

where,

h = Planck's constant,

k = Boltzman constant,

n_{S} = Stokes intensity, and

n_{aS} = anti Stokes intensity.

Since the Raman signal is 0.001% at the highest, there are different techniques to enhance this scattering. Low power lasers and low magnification optics are suitable to acquire Surface-Enhanced Raman Scattering (SERS) spectra in an acquisition time as little as 10 seconds. There are two primary theories: according to electromagnetic theory, SERS arises from the presence of surface plasmon on the substrate; the chemical theory states that SERS involves charge transfer between the chemisorbed species and the metal surface. For a detailed study of temperature dependent anti-Stokes/Stokes ratio under SERS, readers may consult the investigation conducted by Maher et al.[46]. Section 3.3.3 briefly describes how this concept could be used to measure the temperature modification caused by a tip.

2.8 Nanoscale thermometry

Since this dissertation is heavily focused on the optical absorption, it is important to discuss the temperature measurement at the nanoscale. Conventional thermometry is incapable of providing accurate measurement at a sub-micron scale. To capture the miniaturized optoelectronic devices' temperature, scientists have been using different methods, such as infrared thermography, thermoreflectance, micro thermocoupling, Raman, SNOM, TEM, liquid crystal thermography, and many more. Table 2.5 shows the different techniques, along with their corresponding advantages and disadvantages.

2.9 Cross Section

Optical cross section is the maximum value of the incident flux that an object reflects back to the source. For a 3D object, for example, the unit of cross section would be in m^2, because the reflected flux is "imaged" on a 2D surface. Similarly, a 2D circle should have a "cross section" with a unit of m, because in this case, the cross section is simply the length of the imaged line.

2.9.1 Extinction cross section (C_{ext})

Metals have a large concentration of free electrons that scatter light effectively and vibrate with stronger amplitude than those of bound electrons [39]. Hence, a metal particle partially extinguishes the incoming EM energy through absorption and scattering. If the particle were perfectly absorbing and there were no diffraction, the extinction cross section would be the geometrical cross section (i.e. πa^2 for a sphere). Instead, the incoming field is distorted by the presence of a particle, often

Table 2.5: Summary of the advantages, disadvantages and applications of high-resolution electrical, near and far field thermal techniques. Table reproduced with the permission of The Royal Society of Chemistry [47].

		Typical resolution				
Method	Principle	δx(μm)	δT(K)	δt(μs)	Advantages	Disadvantages
Infrared thermography	Planck blackbody emission	10	10^{-1}	10	•Well implemented commercial technique •Provides temperature image profile of the surface	•Detector saturation at high temperatures •Difficulties on the precise estimation of the emissivity of the surface materials
Thermo reflectance	Temperature dependence of the reflection	10^{-1}	10^{-2}	10^{-1}	•High thermal and temporal resolution •Quantitative and qualitative measurement	•Requires the calibration of the reflectivity index •Spatial resolution limited by the diffraction limit
Raman	Inelastic scattering of monochromatic light	1	10^{-1}	10^{6}	•No sample preparation needed •Works in solids and liquids •Small volumes ($<$ 1μm diameter) can be produced	•Highly time-consuming technique implying image point analysis as slow as 0.5 point s^{-1} •Low signal and crosstalk with fluorescent molecule
Near-field scanning optical microscopy	Use near field to improve optical resolution	10^{-2}	10^{-1}	10	•Spatial resolution below the Rayleigh limit (100 nm)	•Depends on the surface characteristics •Only access to surface temperature •Slow temperature acquisition •Vacuum and/or cryogenic temperatures required
Scanning thermal microscopy	AFM with thermocouple or Pt thermistor tip	10^{-1}	10^{-1}	10^{2}	•Use AFM tips to simultaneously measure temperature and determine the surface roughness •Sub-micrometric spatial resolution	•Slow acquisition times •Limited to solid samples •Requires fundamental knowledge of tip-sample heat transfer
Transmission electron microscopy	Thermal expansion	10^{-2}	10^{-1}	10	•High spatial resolution •Compatible with different CNTs	•Vacuum required •Difficult to transpose for practical applications •Temperature determination by image analysis
Optical interferometry	Thermal expansion or refractive index change	1	10^{-5}	10^{-3}	•Can be integrated in remote detection systems •All optical temperature determination	•Crosstalk with other stimulus as strain/stress and bending •Low spatial resolution in the transverse direction

considered as a point dipole, and the extinction cross section is given by:

$$C_{\text{ext}} = 4\pi a^2 x \ \text{Im}\left\{\frac{\varepsilon_1 - \varepsilon_2}{\varepsilon_1 + 2\varepsilon_2}\right\}, \tag{2.23}$$

where,

$\varepsilon_1 =$ the permittivity of the sphere,

$\varepsilon_2 =$ the permittivity of the surrounding medium,

$x = ka$, where,

$a =$ the radius of the particle, and

$k =$ the wave vector [36].

The scattered field interacts with the incident field and results in a net energy flow, giving rise to the actual absorption and scattering. Hence, a strong absorber (with higher imaginary refractive index) is a strong reflector as well [39]. As will be seen from Figures 2.7, 2.8, and Appendix A.3, scattering, and hence extinction, depends on the shape, size, material properties and composition of the particle, the surrounding media, and on the frequency and polarization of the incident light [36].

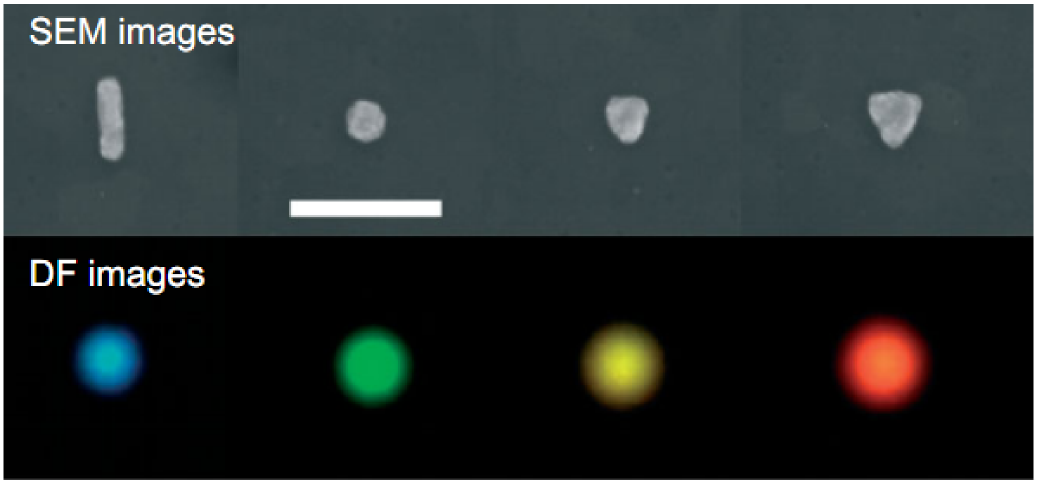

Figure 2.7: Scanning electron micrographs (top) and dark-field images (bottom) of several metallic nanoparticles made by e-beam lithography. From left to right the shapes are, a rod, a disc, and two triangles (the right hand one being the larger of the two). The thickness of these particles was 30 nm and the substrates were made of silica glass coated with 20 nm of ITO. The scale bar in the top figure is 300 nm. This figure is reproduced with permission from Wiley [48].

If the diameter of the particle is much smaller than the wavelength, all the regions in and near the particle respond simultaneously to the incident field. One can then solve for the electric field based on Laplace equation with a quasi-static approximation. In a quasi-static approximation, the solution of electric field inside the particle ($r < a$) would be:

$$E_1 = E_0 \, \frac{3\varepsilon_2}{\varepsilon_1 + 2\varepsilon_2} \; \mathbf{n}_\mathrm{x}, \tag{2.24}$$

where,

E_0 = the amplitude of the applied electric field,

ε_1 = permittivity of the sphere,

ε_2 = permittivity of the surrounding media, and

the unit vector in x direction, $\mathbf{n}_\mathrm{x} = \cos\theta \, \mathbf{n}_\mathrm{r} - \sin\theta \, \mathbf{n}_\theta$ [3].

The solution for electric field outside the sphere ($r > a$) is

$$E_2 = E_0(\cos\theta \, \mathbf{n}_\mathrm{r} - \sin\theta \, \mathbf{n}_\theta) + \frac{\varepsilon_1 - \varepsilon_2}{\varepsilon_1 + 2\varepsilon_2} \, \frac{a^3}{r^3} \, (2 \, \cos\theta \, \mathbf{n}_\mathrm{r} + \sin\theta \, \mathbf{n}_\theta). \tag{2.25}$$

It can be seen from (2.25) that the field is maximum at $r = a$, i.e. at the surface, and decays as r is greater than a. Also, one can see that the field peaks when the resonance condition is reached, i.e. when $\mathrm{Re}(\varepsilon_1) = -2\varepsilon_2$, where ε_2 is already real, being the permittivity of perhaps glass, air, or water. Besides, both (2.24) and (2.25) are independent of ϕ, meaning the solutions are azimuthally symmetric [3]. Section 4.2 will describe how the symmetrical planes help to reduce the computational domain, and thereby, result in time efficient simulations. Numerically, extinction cross section is the summation of absorption and scattering cross sections.

2.9.2 Absorption Cross Section (C_abs)

Even for a similar shape, the size of the nanoparticle determines the wavelength of absorption, as is shown in Figure 2.8. The absorption cross section C_abs is the effective area of a perfectly opaque object that gives the same amount of absorption as the real object. C_abs is a measure of the probablity of the absorption, and the cross sections of a number of particles are additive. It is defined as:

$$C_\mathrm{abs} = k_0 \ \mathrm{Im} \left\{ 4\pi a^3 \frac{\varepsilon_1 - \varepsilon_2}{\varepsilon_1 + 2\varepsilon_2} \right\} \tag{2.26}$$

where k_0 is the wave vector. Section 3.3.1 will discuss that by changing the position of the silicon tip, one can effectively change the ε_2 of (2.26) and thereby, the C_abs. With regard to the description

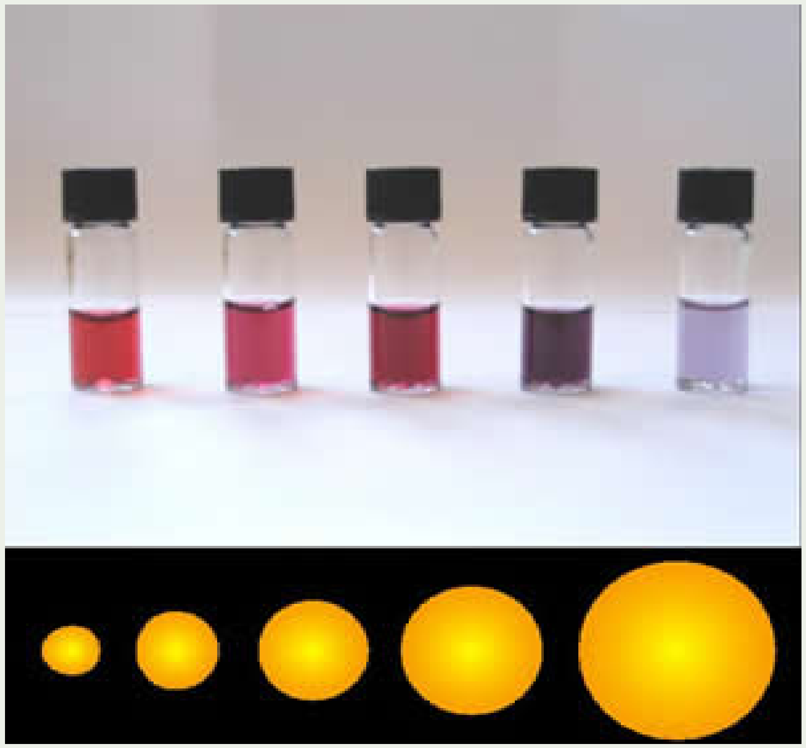

Figure 2.8: Color of the different sized gold nanoparticles, from WebExhibits.org

in Section 2.5.2, when the plasmon is excited at resonant condition, the C_{abs} tend to peak at the same wavelength.

One important note is that the absorption cross section can very well be greater than geometrical cross section. With regard to Section 2.9.1, it can be visualized that the perturbation of the field around the nanostructure causes the electromagnetic energy to funnel in the nanostructure. Additionally, the absorption of radiant energy is a function of the conductivity, which may be zero for a dielectric but nonzero for a metal. For a sphere, the C_{abs} should not depend on polarization. However, as will be discussed in this dissertation, it is the presence of substrate and/or tip that makes the difference for different polarization. For an infinitely large sphere (much larger than the skin depth), the incident energy is primarily absorbed in the outer surface. The inner region of that large sphere, on the other hand, plays almost no role in the absorption. In other words, the absorption is proportional to the area and not proportional to the volume [36].

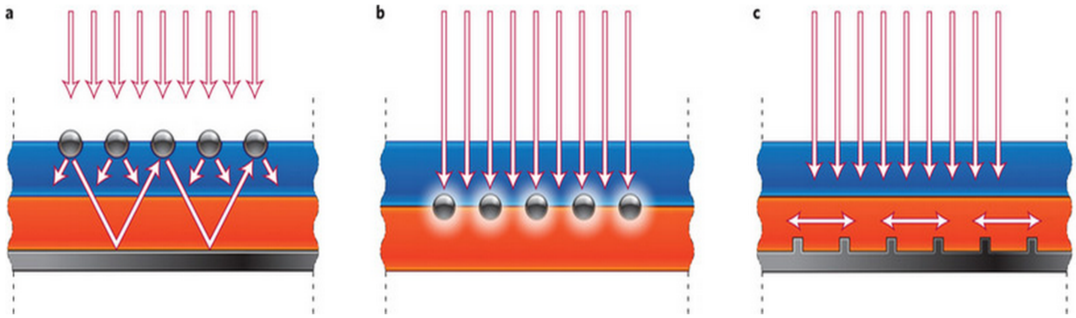

Figure 2.9: Usage of plasmonics for increasing the photovoltaic absorption: (a) Light trapping by the preferential scattering off of the metal nanoparticles. (b) Light trapping by the excitation of the localized surface plasmon embedded in the semiconductor. (c) Light trapping by exciting surface plasmon polaritons at the metal semiconductor interface. Figure reproduced with the permission from Nature Publishing Group [42].

2.9.3 Scattering cross section (C_{sca})

Scattering is the difference between extinction and absorption, and the scattering cross section, C_{sca} is given by [36]:

$$C_{\mathrm{sca}} = \frac{8}{3} k_0^4 a^6 \pi \left| \frac{\varepsilon_1 - \varepsilon_2}{\varepsilon_1 + 2\varepsilon_2} \right|^2 \tag{2.27}$$

Equation (2.26) indicates that the $C_{\mathrm{abs}} \propto a^3$ and hence, is dominant for small (smaller than the incident wavelength) particles. From (2.27), $C_{\mathrm{sca}} \propto a^6$, i.e. for a larger (compared to the wavelength) particle, the C_{sca} is dominant over the C_{abs}. As the size of the particle increases, the scattering at the longer wavelength increases proportionally. This occurs because there is a thin layer ($\approx \frac{\lambda}{2}$) of unpaired atomic oscillators that contributes to the reflected wave. When longer wavelengths are incident, more of the waves penetrate the material and more of the scatterer acts together to reflect off the wave [39].

In a homogeneous media, the scattered light is nearly symmetric at forward and reverse directions. As will be described in Section 3.2.1, a particle surrounded by a homogeneous media is a comparatively simple problem to solve, and an analytical solution is available to calculate the exact scattering off of a spherical particle. Again, as was described in Section 2.5.3, these problems were formulated with electrostatic approximation, and should not apply to large structures. The denser the medium through which light advances, the less lateral scattering occurs. A perfectly arranged solid will not laterally scatter at all. However, if a particle is placed at or close to the interface between two dielectrics, as is shown in Figure 2.9 (a), it would preferentially scatter more into the medium with the larger permittivity. This phenomenon has been used to increase the optical path length inside a solar cell [36, 42].

2.10 Comparison of Finite Element Method (FEM) with other computational EM methods

There are many ways to solve for the electromagnetic field distribution for a definite geometry. Methods such as multiple multipole (MMP) [50], generalized field propagator technique[51], Finite Difference Time Domain (FDTD) [31], method of moments [52], the boundary element method [53], or discrete dipole approximation [54] have their own advantages and disadvantages, as can be seen in Table 2.6. Several numerical approaches have been used to analyze the optical properties of metal tips for tip-enhanced spectroscopies. With the help of full 3D FDTD simulations, Sukharev et al. explained the significance of the tip geometry and tip material for different mode resonances [55]. Muller et al. associated a 3D FDTD method with a near-field to far-field transformation taking into account the interface near the scattering object, validated by known cases like a dipole, to study the field scattered by a tip in apertureless SNOM [56]. The effects of sample and substrate electrical properties on the field enhancement at the apex of tips have also been studied by Notingher et al.using the finite element method (FEM) [57]. Micic et al. simulated electric field enhancement, around AFM-TERS experiment on silver nanoparticles under different illumination angles, using FEM, and compared the results with MMP and FDTD [58]. Due to the availability of the software, the flexibility to couple with different multi physics modules, and the built-in interface with MATLAB, the research for this dissertation conducted numerical simulations with COMSOL using FEM to understand the effects of dielectric and metallic probes on gold and silver nanoparticles. With regard to Table 2.6 this method does provide sufficient accuracy, and COMSOL software is well suited for the high performance computing.

FEM has a few fundamental steps [59]:

- Discretizing the physical domain (creating the mesh, as will do in Section 4.4),
- Choosing the appropriate interpolation functions (linear or polynomial),

Table 2.6: Comparison of five different techniques to calculate the scattering of the electromagnetic radiation from metallic nanostructure, along with the corresponding advantages, disadvantages, and computational times. The computations were conducted on a Dell Vostro 200 PC, having a dual-core processor (each having a 2.19 GHz clock speed) and 2 Gb of RAM. Table reproduced with permission from Taylor & Francis [49].

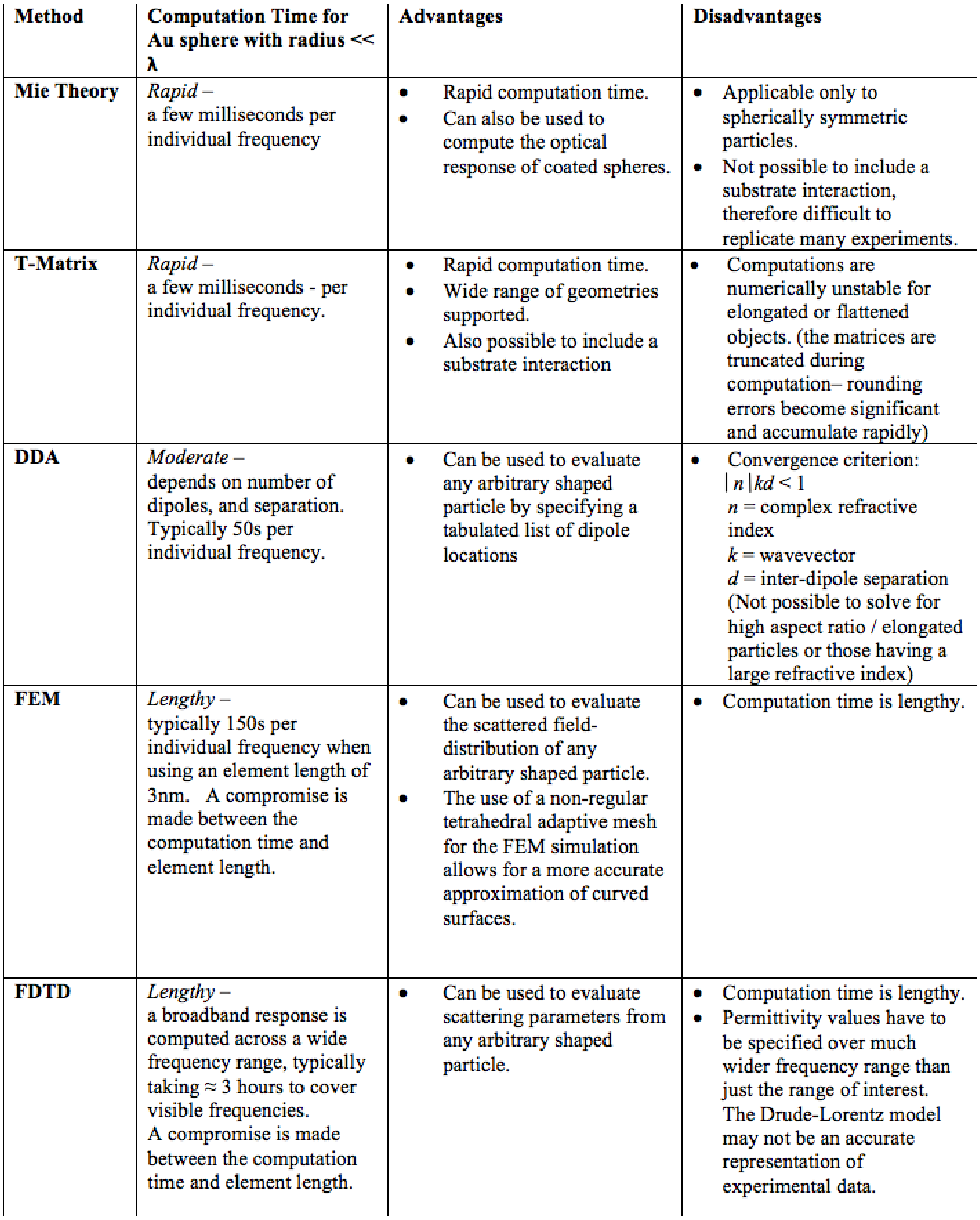

Method	**Computation Time for Au sphere with radius << λ**	**Advantages**	**Disadvantages**
Mie Theory	*Rapid* – a few milliseconds per individual frequency	• Rapid computation time. • Can also be used to compute the optical response of coated spheres.	• Applicable only to spherically symmetric particles. • Not possible to include a substrate interaction, therefore difficult to replicate many experiments.
T-Matrix	*Rapid* – a few milliseconds - per individual frequency.	• Rapid computation time. • Wide range of geometries supported. • Also possible to include a substrate interaction	• Computations are numerically unstable for elongated or flattened objects. (the matrices are truncated during computation– rounding errors become significant and accumulate rapidly)
DDA	*Moderate* – depends on number of dipoles, and separation. Typically 50s per individual frequency.	• Can be used to evaluate any arbitrary shaped particle by specifying a tabulated list of dipole locations	• Convergence criterion: $\lvert n \rvert kd < 1$ n = complex refractive index k = wavevector d = inter-dipole separation (Not possible to solve for high aspect ratio / elongated particles or those having a large refractive index)
FEM	*Lengthy* – typically 150s per individual frequency when using an element length of 3nm. A compromise is made between the computation time and element length.	• Can be used to evaluate the scattered field-distribution of any arbitrary shaped particle. • The use of a non-regular tetrahedral adaptive mesh for the FEM simulation allows for a more accurate approximation of curved surfaces.	• Computation time is lengthy.
FDTD	*Lengthy* – a broadband response is computed across a wide frequency range, typically taking ≈ 3 hours to cover visible frequencies. A compromise is made between the computation time and element length.	• Can be used to evaluate scattering parameters from any arbitrary shaped particle.	• Computation time is lengthy. • Permittivity values have to be specified over much wider frequency range than just the range of interest. The Drude-Lorentz model may not be an accurate representation of experimental data.

- Formulating the system of equation (with the unknowns as the coefficients for each element), and
- Solving the system of equations.

An example is given in Appendix A.4.1 to explain the FEM concept.

2.10.1 FEM comparison with DDA

Grosges et al. previously compared FEM and FDTD with Mie for a suspended particle [60]. This part of the research benchmarked the near field spectroscopic and intensity map computation for particles on a substrate for a Discrete Dipole Approximation with Surface Interaction (DDA-SI) [18] with FEM. Appendix A.4.2 describes the fundamentals of DDA. The purpose of this work is to validate DDA-SI with the help of FEM, FDTD and an analytical method for sphere-planar substrate scattering [61]. For a particle only, one could effectively conduct the analysis using Mie theory. Where there is a high imaginary component in its refractive index, as in AuNP, DDA-SI requires volume correction [62]. Therefore, by shrinking the radius by 3%, the scattering fits nicely. This volume correction is not required if the refractive index has a low imaginary component. Interestingly, when there is a substrate present, a volume correction is not needed, as can be seen from Figure 2.10. Perhaps it reduces the overall contrast in refractive index (i.e. between AuNP and the environment).

The standard DDA was designed for modeling free-space light scattering. Here, discrete dipole approximation with surface interaction (DDA-SI) is used to accommodate the particle sitting on a planar substrate [18, 63]. DDA-SI is a public domain MATLAB toolbox for both free-space and half-space-substrate light scattering calculations [64].

The T-Matrix, which is determined by the scatterer shape and material, relates the expansion coefficients of the incident field to those of the scattered field. One way to calculate the T-Matrix is the Null-Field method (NFM), which states that the electromagnetic fields outside a given volume can be expressed as integrals over the surface that encloses the volume involving only the tangential components of the fields on the surface. If the observation point is located inside this volume, the integrals vanish [24]. Figure 2.11 describes the comparison of absorption and extinction, during

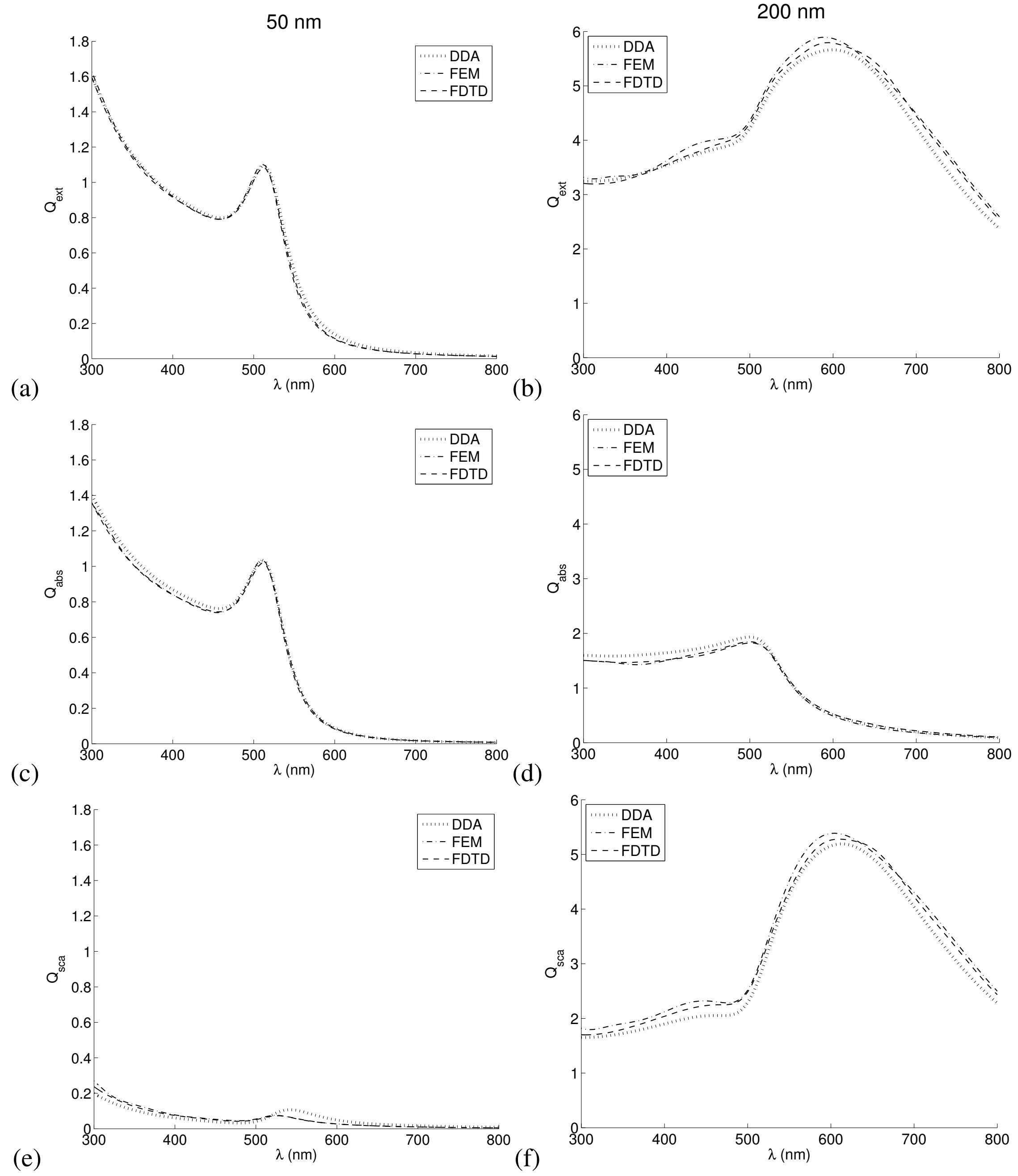

Figure 2.10: $Q_{\rm ext}$, $Q_{\rm abs}$ and $Q_{\rm sca}$ efficiency spectra of the 50 nm (left column) and 200 nm (right column) Au nanosphere sitting on a BK7 glass planar substrate, illuminated by a plane wave propagating in normal to the surface. Figure courtesy of Vincent Loke.

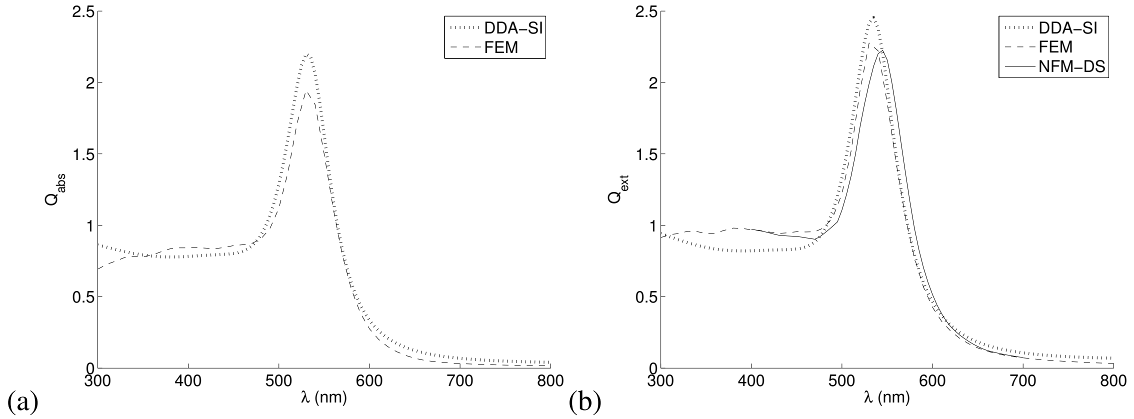

Figure 2.11: The (a) absorption and (b) extinction efficiency spectra of a 50 nm Au nanosphere under evanescent wave illumination (TM), calculated using DDA-SI and FEM, and in b) also compared against the NFM-DS, which is described in Appendix A.4.3. Figure courtesy of Vincent Loke.

evanescent wave illumination, as was in most of the simulations in this dissertation, and compared with Null-field method with discrete sources (NFM-DS). NFM-DS is described in Appendix A.4.3.

2.11 Deformation of nanostructure under laser irradiation

At macro scale under laser illumination, a metal can melt. At nanoscale, however, "melting" is more appropriate to describe as a conformational change of the structure from one shape to another. For example, a sphere is a thermodynamically stable particle shape, which has the lowest surface energy of any shape. If one heats a nanorod with a powerful laser, in an ideal world, the rod should always be deformed to become a nanosphere. In the real world, however, a rod may be fragmented, take a ϕ shape, or just fly off the substrate depending on the laser energy and pulse width [65]. Figure 2.12 shows the time scales of the fundamental processes in ultrafast laser heating of metal nanoparticles before the onset of particle melting or bubble formation in the surrounding aqueous solution. Chapter A.6 will explain the experimental setup of this dissertation to deform a nanorod with a Continuous Wave (CW) laser and Appendix A.7 will show the results. Similar to the Section 2.6, here a photon will be compared with a phonon, which is defined as the particle excitation of a lattice vibration. Although a photon can be considered as either a wave or a particle, a phonon can neither be a wave nor a particle. Unlike light's polarization being transverse to the direction of propagation, as was shown in Section 2.2, a phonon can only polarize along the direction of propagation, which has the speed of sound. After the laser exposure, the free electrons gain kinetic

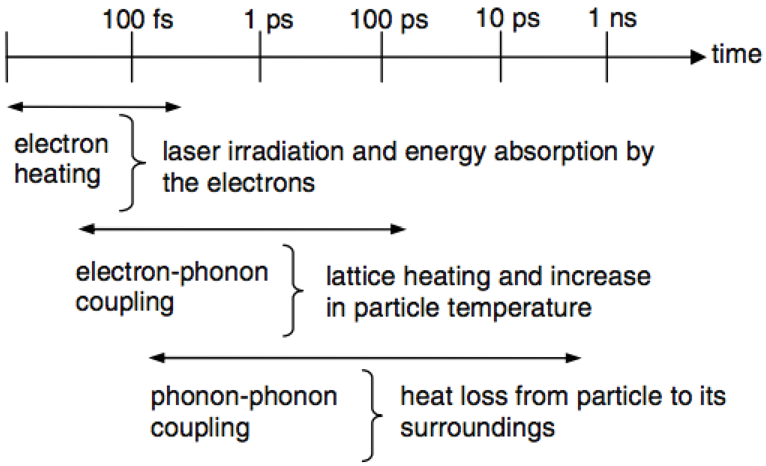

Figure 2.12: Summary of various processes associated during ultrafast laser heating of nanoparticles. Figure reproduced with permission from IOP publishing [66].

energy and are relaxed through electron-electron scattering. The temperature of the lattice starts increasing through electron-phonon interaction. Finally, the heat is transported to the surrounding media by phonon-phonon coupling, as is shown in Figure 2.12 [66].

Chapter 3

Current Research Status

3.1 Optical Wave Guide (OWG)

This report proposes to develop an on-chip sensor utilizing an optical waveguide and to study the effects of nanostructure proximity to the waveguide's guided mode. Being immersed in the evanescent wave of the waveguide, the nanostructure should experience two major effects:

- First, in response to the electromagnetic energy in the waveguide mode, there will be optical absorption inside the structure.
- Second and more importantly, the nanostructure will scatter light, leading to a partial back coupling into the waveguide.

The goal is to tune the nanostructure such that, when a specific analyte becomes attached to the metallic nanostructure, the scattered light would interfere with the propagating wave inside the waveguide destructively. Ideally in such cases, there should be no light to detect at the end of the optical waveguide. This condition would allow for the positive identification of a particular analyte in a sample. Thus, the project should result into a significantly reduced size optical sensor, which would be portable and easy to use. The following two subsections enlists the research that are done in sensing and antenna community using similar structures.

3.1.1 Sensing

As was described in Section 2.3, the evanescent wave at the interface of the core and cladding is used for highly sensitive optical monitoring. Usually the modification of input signal's optical properties, such as phase, intensity, frequency, and polarization are scrutinized to detect a specific component. Furthermore, there are significant advantages of using OWG sensors, such as portability, robustness, immunity against electromagnetic interference, higher sensitivity, short response time, lower cost, and high compatibility with fiber optic networks. The analytical analysis is conducted by Verma et al. [67]. Yimit et al designed and fabricated thin-film composite waveguide, where an additional thin composite layer of K^+ ion-exchanged glass with taper end is deposited on the OWG to enhance the evanescent field [68]. Using the concept of surface plasmon, as was described in Section 2.5.3, Integrated optical waveguide-coupled SPR sensor was devised by Dostálek et al. They reported a bulk sensitivity of 1.2×10^{-6} refractive index unit (RIU) [69].

3.1.2 Antenna Design

The waveguide structure, along with a nanostructure, finds application in antenna design too. The subwavelength plasmonic nanostructures are tuned to radiate or receive signals at or around optical wavelengths. Li et al. showed how to tailor the radiation pattern by placing multiple adjacent structures while feeding the slab waveguide [11]. Using a similar a structure, Chettiar et al. used a coreshell to match the impedance between a guided and radiation mode of a dielectric waveguide in free space. In addition, the setup can "sense" the gap between the waveguide edge and the coreshell by monitoring the waveguide's reflected wave [70]. By adjusting the dimension of a nanowire, Arnaud et al. explained that the radiation pattern from such coupled system can be tuned. The authors found the far-field resonance at 580 nm for the smallest wire and 670 nm for the widest [71]. Through FDTD investigation, Yaacobi et al. proposed the use of deep sub wavelength frequency-chirped elements to enable efficient vertical emission from a dielectric waveguide. The authors used coupled mode theory to describe the interaction between the nanoantenna and the waveguide. The steady state solution of the energy amplitude, a, for the corresponding differential equation is [72]:

$$a = \frac{-\jmath\mu s}{\jmath(\omega - \omega_0) + \frac{1}{\tau}} \equiv sRe^{\jmath\Delta\phi}, \tag{3.1}$$

where,

$\mu =$ coupling efficiency,

$s =$ field amplitude,

$R =$ resonator amplitude,

$\Delta\phi =$ resonator phase, varying in the range $(\pi, 0)$ depending on ω_0 value μ being positive,

$\omega_0 =$ resonance frequency, and

$\tau = \tau_r + \tau_0 + \tau_e =$field decay rate,

where,

τ_r is for radiation loss,

τ_0 is for ohmic loss, and

τ_e is for coupling loss [72].

3.2 Particle without a tip (or tip at infinity)

3.2.1 Particle in isolation: Mie Theory

In 1908, Gustav Mie developed a theory to understand the different colors produced by absorption and scattering of small colloidal gold particles suspended in water [36]. The formulation helps to calculate the electric and magnetic fields inside and outside of a homogenous sphere or an infinite cylinder. Mie theory expresses the wave inside and out of the structure as a summation of vector spherical harmonic basis functions. It can be used to accurately predict the cross sections of a particle suspended in a homogeneous medium. Unlike Rayleigh scattering, Mie theory is valid regardless of the wavelength. It can be effectively used for particles with diameter comparable to or much bigger than the incident wavelengths [73]. Mie theory has been used to validate the simulation setup, as will be explained in Section 4.5.1. Detailed equations about Mie theory are contained in Appendix A.3.

3.2.2 Particle on a substrate

Nordlander and Halas' groups have studied the influence of an adjacent dielectric substrate on an individual plasmonic nanoparticle. They assumed that the change of relative permittivity of the di-

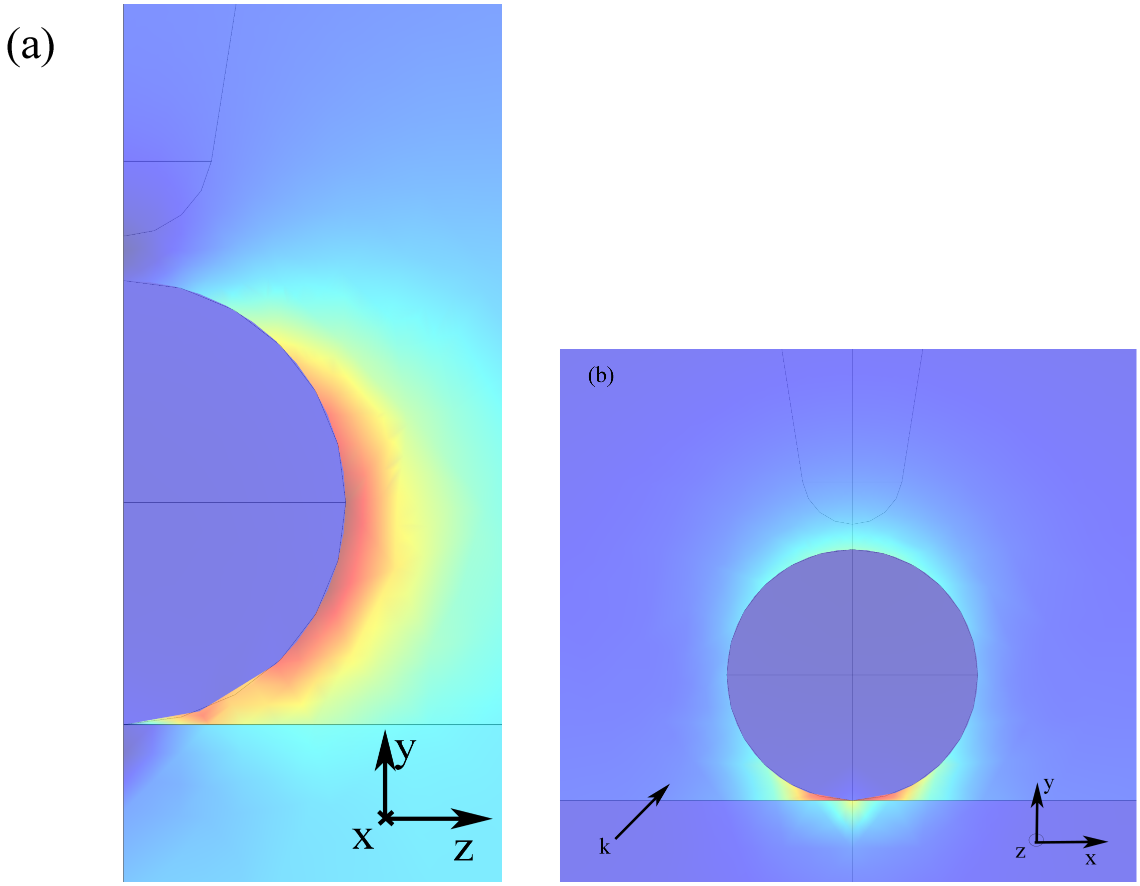

Figure 3.1: (a) Norm of the electric field ($\sqrt{E_{\mathrm{x}}E_{\mathrm{x}}^{*}+E_{\mathrm{y}}E_{\mathrm{y}}^{*}+E_{\mathrm{z}}E_{\mathrm{z}}^{*}}$) for TE illumination of a 50 nm diameter Au particle. (b) norm of the electric field for TM illumination. In both polarization, the incident was at 50°. The tip was defined as air. The strong effect of the substrate for TM polarization in (b) is notable. For TE polarization in (a), the effect of substrate is insignificant.

electric with frequency was not significant. They showed that the dielectric does not directly interact with the metal nanoparticle, except by increasing the effective refractive index of the surrounding media. This increase causes a redshift in the absorption spectra [36]. If one has a substrate with higher permittivity, it will create a stronger image of the particle and yield a stronger interaction. This interaction also depends on the nanoparticle-substrate separation and the polarization of the incident light. This is also shown in this dissertation in Section 3.4. For transverse electric (TE) illumination, where the electric field is normal to the symmetry plane (that contains the axis of the particle and the propagation vector), the resulting particle polarization is parallel to the surface, leading to a weaker interaction. On the same token, transverse magnetic (TM) polarization, where the magnetic field is normal to the symmetry plane, leads to an increased charge density and electric field near the substrate. This leads to a stronger interaction between the particle and substrate. The simulations of this dissertation produced similar results obtained by Nordlander and Halas, as shown in Figure 3.1. Likewise, increasing the permittivity of the substrate increases the relative wavelength shift between the TE and TM incident polarization spectra [15].

3.3 Particle with the presence of a sharp nanoscale tip

Tip based imaging, sensing, and nanofabrication can all benefit from understanding the optical properties of nanostructures, in proximity to an atomic force microscope (AFM) probe [6, 74]. Optical scattering cross sections and electrical field enhancements for particle-probe systems have been previously analyzed to better understand tip enhanced Raman spectroscopy (TERS) and aperture-less scanning near-field optical microscopy (aSNOM) [75, 76]. Typically, for SNOM applications, a plane wave or a total internally reflected wave is used to illuminate the sample, which is in close proximity to a sharp nanoscale probe. In relevant simulation work, Esteban et al. investigated the achievable resolution and contrast for an aSNOM using an embedded gold nanoparticle (AuNP) inside the glass substrate under direct illumination [77].

The effect of the tip can be viewed from two perspectives:

- Even in the absence of a particle, light will evanescently couple, or optically tunnel, from the substrate to the high dielectric constant tip.

- The tip strongly perturbs the nanoparticle's local dielectric environment.

In both cases, one expects the presence of the tip to enhance absorption and scattering for the nanoparticle and to locally enhance the electric field between the tip and particle. Moreover, one would expect the spatial localization of these near-field effects to be governed primarily by the geometry and not by the wavelengths of illumination. Although some experiments are conducted with metal tips to further enhance the field, the dielectric tip allows one to study these effects without introducing additional complexity associated with the localized surface plasmon resonances of the tip itself. Better understanding of this geometry will lead to a better control of selective absorption and field enhancement with possible applications in deterministic patterning, sensing, and imaging.

There have been only a few reports describing the optical phenomenon associated with a tip near a particle. Fikri et al. conducted 2D finite element simulations of scanning probe/particle geometries to study the effect of probe vibration and lock-in detection on scanning near-field optical microscopy [78]. Stiles et al. experimentally studied the effect of a standard AFM tip on optical scattering from nanoparticles [13]. Most recently Sadiq et al. investigated a system in which nanoparticles were probed with a metallic, grating-coupled, near-field optical probe [79]. They used focused scattering type near field scanning optical microscopy (s-NSOM) to demonstrate sub-30 nm resolution of SPP fields.

The behavior of nano-tip under laser irradiation was explored by Chen et al. [21]. The emphasis was on studying the effect of tip radius of curvature, aspect ratio and polarization of the incident laser. They demonstrated that the peak field enhancement decreases exponentially with increased distance between tip and substrate. A similar effect is found in the simulations in Figure 3.10, in which enhancement decreases exponentially as the tip moves away from the particle. Additionally, Chen et al. found from Poynting vector study that the incident light ”bends” around the tip and is confined under the apex, where the field enhancement is the greatest.

In 2010, Loke et al. explored a similar geometrical setup numerically using a version of the Discrete Dipole Approximation (DDA) [18] technique and published a Matlab toolbox with surface interaction (SI) [63]. However, they studied the internal and external field and the focus was on the effect of shaft length of the AFM probe.

Although highly informative, the papers mentioned above do not address the absorption and field enhancement associated with the geometry of interest here: a simple tip near a nanoparticle under TIR or SPP illumination. In addition to the intrinsic interest of this scarcely explored geometry, this configuration also requires addressing several simulation challenges, which should prove useful in addressing a broad range of nanoscale optical problems via the finite element method (FEM).

3.3.1 Effects of a dielectric tip at evanescent field illumination

Evanescent wave illumination

Evanescent wave illumination is a key component in SNOM and photon scanning tunneling microscopy. The scattering caused by aggregates of nanoclusters has been evaluated analytically using the extended Mie theory by Quinten [80]. Benrezzak et al. used an SNOM-AFM combination to prove that the optical image contain near-field information by varying different parameters such as wavelength, amplitude oscillation of the tip, polarization of the light and size of the particles [81]. Using a 2D TM-wave finite difference time domain (FDTD), Hong et al. explored the effect of a metal probe in an evanescent field and concluded that metal probe has a larger field enhancement compared to the nonmetal probe [82]. The evanescent field is also used to excite surface plasmon polariton waves, which are widely used in sensing [83]. Thus, in keeping with important experimental geometries, this investigation illuminates the particles using total-internal reflection. This method uses a TM wave such that a significant electric field component is aligned with the tip, and consider wavelengths near the particles localized surface-plasmon resonance.

As a part of his Masters research, the author of this dissertation explored the effects of a nanoscale tip on the absorption and field enhancement for a metallic nanoparticle illuminated under total internal reflection conditions using the finite element method. For an electric field polarized orthogonal to the tip axis, little effect is observed. If the electric field is partially polarized along the tip axis, then both absorption and electric fields are strongly enhanced. The enhancement is accompanied by a red-shift in the surface-plasmon resonance wavelength of the particle. These effects are observed when the vertical and horizontal separation of the tip and nanoparticle are significantly less than the wavelength of the illuminating light. The technique can be used to selectively excite nanoparticles, and thus drive modification processes, far below the diffraction limit. The change in absorption and field enhancement with particle size indicates that there is likely to be a tradeoff between spatial localization of these effects and their maximum enhancement. Further studies are required to better understand this tradeoff. The results are summarized below.

Effects of a Si tip on Localized Surface Plasmon Resonance (LSPR)

Metal nanoparticles can scatter light over a broad range that can be tuned by the surrounding dielectric, as can be seen from Figure 3.2.

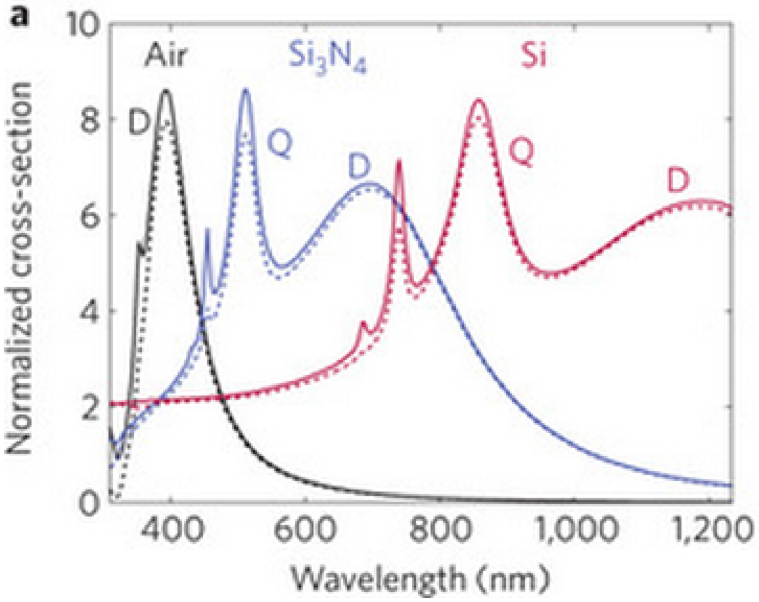

Figure 3.2: Controlling the red shift of the localized surface plasmon resonance of a 100 nm diameter AgNP by changing the surrounding media. Figure reproduced with the permission from Nature Publishing Group [42].

As the resonance condition of an isolated particle depends on the relative permittivity of the surrounding media, the substrate, as a perturbation, causes red shift of the resonant wavelengths [3]. In Section 5.1, the comparison between a tip and a homogeneous medium will be discussed in the context of the setup of Figure 3.3.

It is well established that C_{abs} near the surface-plasmon resonance of nanoparticles increases as the permittivity of the surrounding media increases. The peak absorption wavelength also redshifts as the energy associated with the plasmon resonance decreases in a more strongly polarizable environment [36]. As a result, the presence of a substrate causes a small increase, and red shift, in the absorption resonance with respect to the particle in free space [3]. This can be seen by comparing Figure 3.4 (a), the free space result, with the no tip case in Figure 3.4 (c-d).

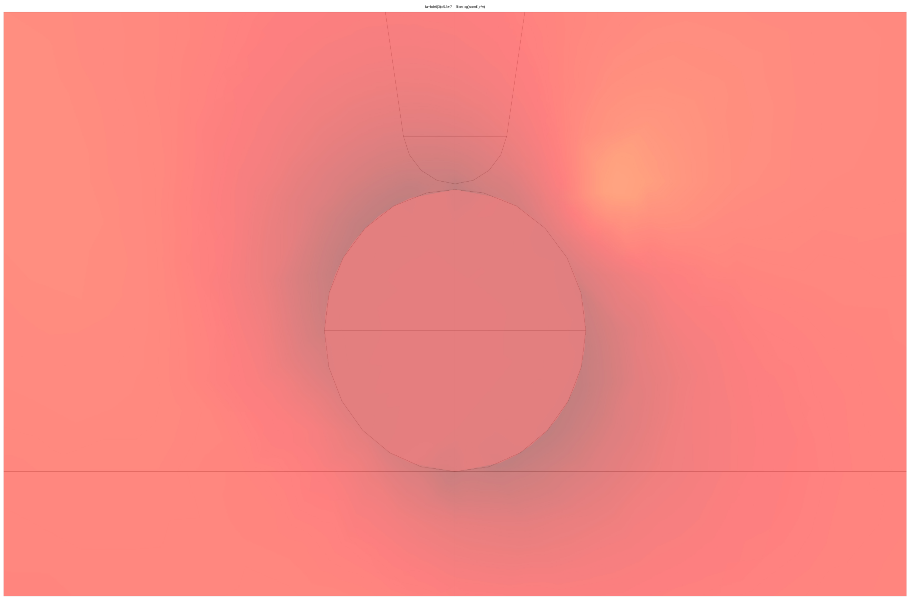

Figure 3.3: Logarithmic plot of the norm of E field around a AuNP, completely embedded in glass (*n*=1.5) at 532 nm wavelength, having a transverse magnetic polarization.

The simulations in Figure 3.4 (d) show further shift in SPR as the Si tip is introduced and is brought closer to the particle. With the decreasing vertical distance between the tip and particle, the opposite charge close to the gap reduces the energy of the configuration [3]. This makes the system resonate at a lower frequency. As is evident from Figure 3.4 (c), the variation in C_{abs} for TE polarization is insignificant with different vertical distance. This is caused by the electric field component in TE polarization being transverse to the tip direction and hence, has less interaction with tip than the parallel E-field component of TM polarization.

More importantly, the high dielectric constant silicon tip can strongly modulate C_{abs}. Figure 3.4 (b) plots the absorption cross-section as a function of tip-particle separation at a fixed wavelength (532 nm). Simulations were conducted down to 1-nm separation; however, it has been established that purely electromagnetic analysis is insufficient to accurately quantify interactions at gaps of $\sim$ 1 nm or less [84]. The 1-nm data point is included here as a reference for future comparison with coupled electromagnetic and quantum mechanical simulations.

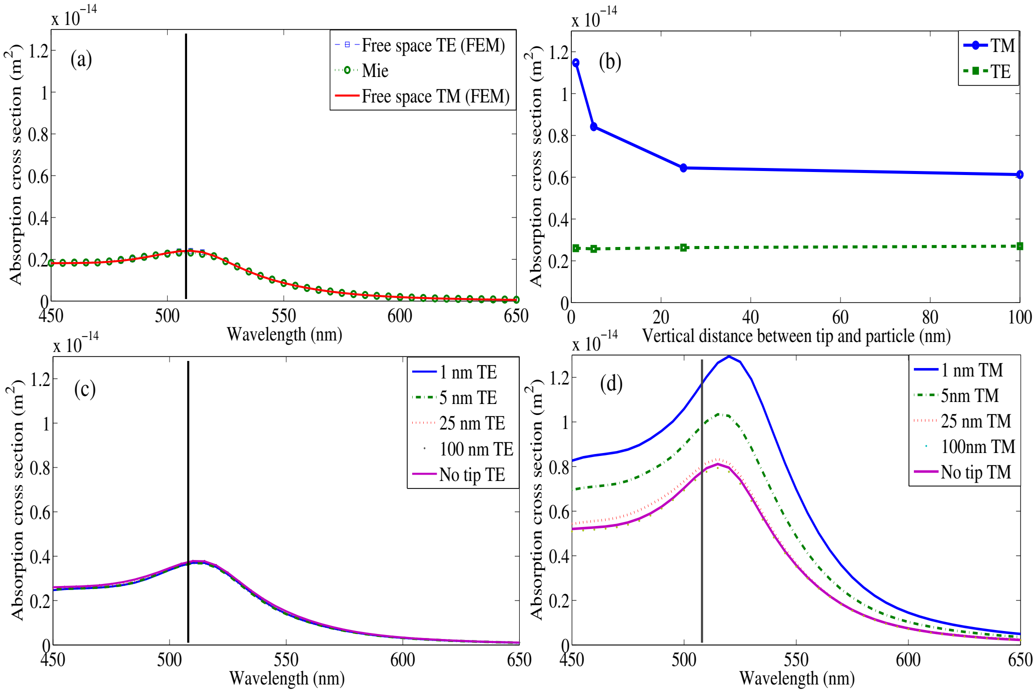

Figure 3.4: (a) Validation against Mie theory for both TM and TE polarization (physically indistinguishable at normal incidence) waves. The worst-case relative error is below 5%. (b) Effect of tip proximity on C_{abs} of AuNP at 532 nm. For TM illumination with a strong electric field component along the tip axis, the absorption increases rapidly as the tip approaches the particle. For TE polarized illumination, the tip has little effect. (c) Under TE polarized illumination, the tip slightly increases and red shifts absorption; however, varying tip-particle separation has little effect. (d) Under TM illumination, the absorption increases and the resonance wavelength red shifts markedly as the tip approaches the particle. In all cases the y-axes were kept consistent to allow direct comparison. The black vertical line indicates the resonant wavelength of AuNP in free space.

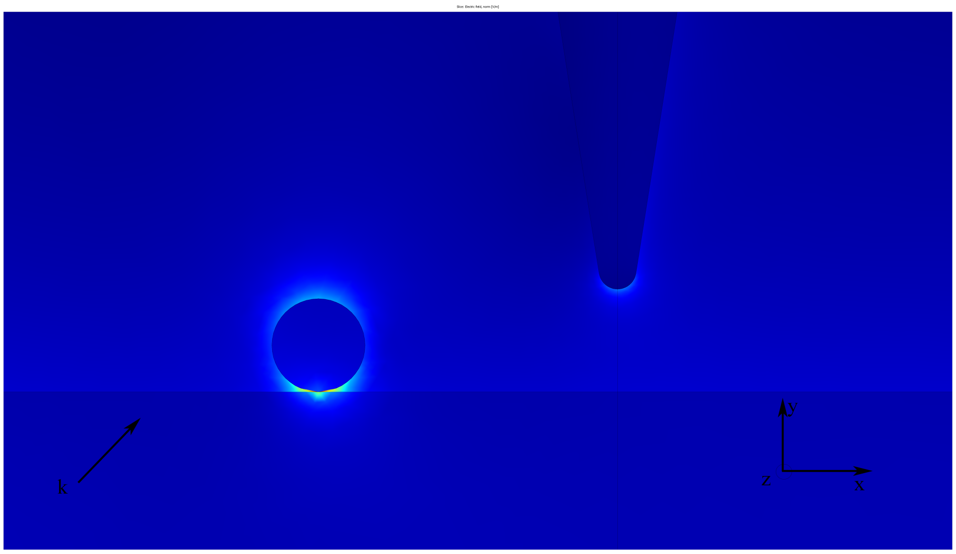

Figure 3.5: Changing the horizontal distance between the tip and particle. The vertical distance between the tip and particle was kept at 5 nm and the incident angle was 50°. In this case, the particle is 160 nm left to the tip.

Changing the lateral distance between the Si tip and the AuNP:

The dependence of absorption on lateral separation between the tip and the particle is investigated. In this case, the separation is along the direction of illumination, as depicted in Figure 4.2. To simplify the design of the simulation geometry, the particle was moved in the simulation domain rather than the tip. A positive lateral offset indicates that the tip is located to the left of the particle, according to the view in Figure 4.2. The vertical separation between the tip apex and the topmost point of the AuNP was kept constant at 5 nm. As the tip is brought closer to the particle laterally, C_{abs} is enhanced under 50° TM illumination at 532 nm, as depicted in Figure 3.6 (a) . The maximum C_{abs} occurs when the tip is located 5 nm to the left of the particle based on the perspective of Figure 4.2. Asymmetry in the relationship between absorption cross-section and position is not surprising given the asymmetric illumination. The lower, broader peak, that occurs when the tip is to the right of the particle, is attributed to interference effects resulting from reflection and scattering from the tip. Once again, the tip has little effect for the TE polarization case. Importantly, the absorption enhancement is spatially localized at the scale of the tip-particle geometry, not the wavelength of light. As a result, nanoparticles can be selectively targeted for modification, sensing, or processing at a scale far below the diffraction limit.

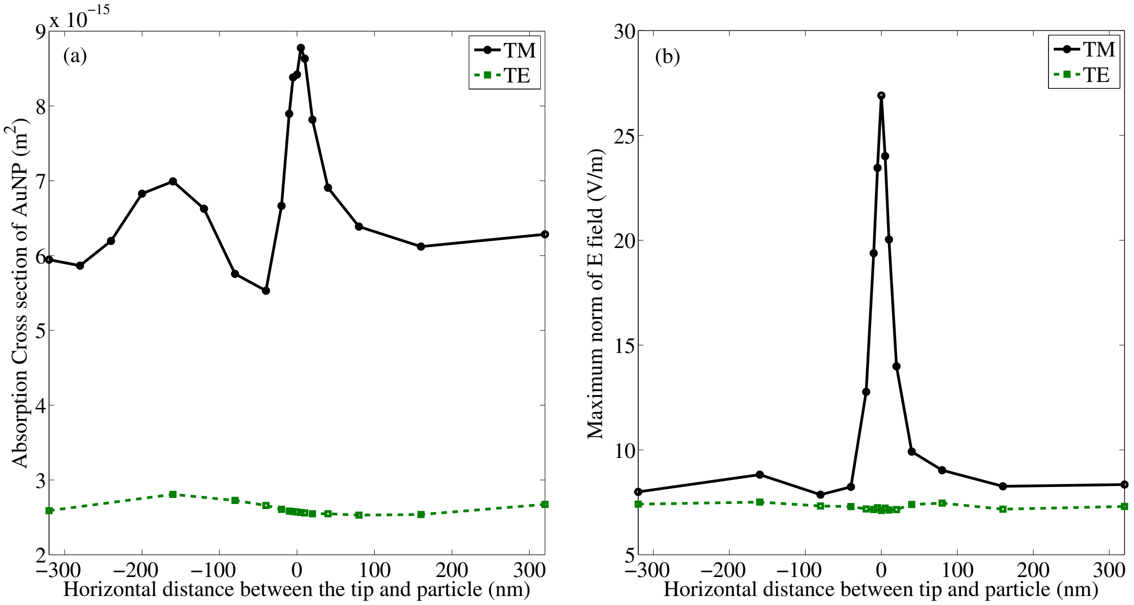

Figure 3.6: (a) Change of C_{abs} of AuNP as a function of lateral tip-nanoparticle separation. Positive values indicate the tip is to the left of the nanoparticle based on the perspective of Figure 4.2. (b) Maximum electric-field enhancement as a function of tip-nanoparticle lateral separation. In both cases, the enhancement is localized to scales far below the diffraction limit of the incident light. Again, the incident wavelength and angle was 532 nm and 50° respectively.

Figure 3.6 (b) plots the field enhancement observed at the top surface of the particle. This was determined by locating the maximum norm of the E field within a rectangular solid domain surrounding the top half of the nanoparticle. In this case, the localization of the effect is even more pronounced. As the tip moves across the top of the particle, both the vertical and horizontal gap between the tip surface and the metal surface are reduced. Thus, the enhancement rapidly increases and is localized to a distance of approximately 40 nm.

Interestingly, although the maximum absorption occurs slightly off axis (the particle is at 5 nm right to the tip), as in Figure 3.6 (a), the field is greatly enhanced when the tip is directly above the particle, as in Figure 3.6 (b). The exponentially decaying incident field and inversely cubed distance decay of the LSPR field interaction may be responsible for that.

Effect of a Si Tip on Field Enhancement:

In the simulations, the amplitude of the incident wave was 1V/m; therefore, the norm of the electric field corresponds directly to the field enhancement. The field enhancement data were sampled at 4394 points in the upper half of the AuNP to evaluate the maximum field because with different relative positions of the tip, the maximum field occurs in different positions around the particle surface. Even with a 1 nm vertical distance, however, the quantum mechanical effect is not taken into account. With that small of a distance, the classical approach should lead to a monotonic increase in the field enhancement. But, tunneling effects may very well modify the optical response and reduce the electric field enhancement in this case [84]. Close to the critical angle, the glass-air interface itself would give a strong field enhancement [85]. Even then, the tip has a significant effect on the C_{abs} as is seen in Figure 3.7.

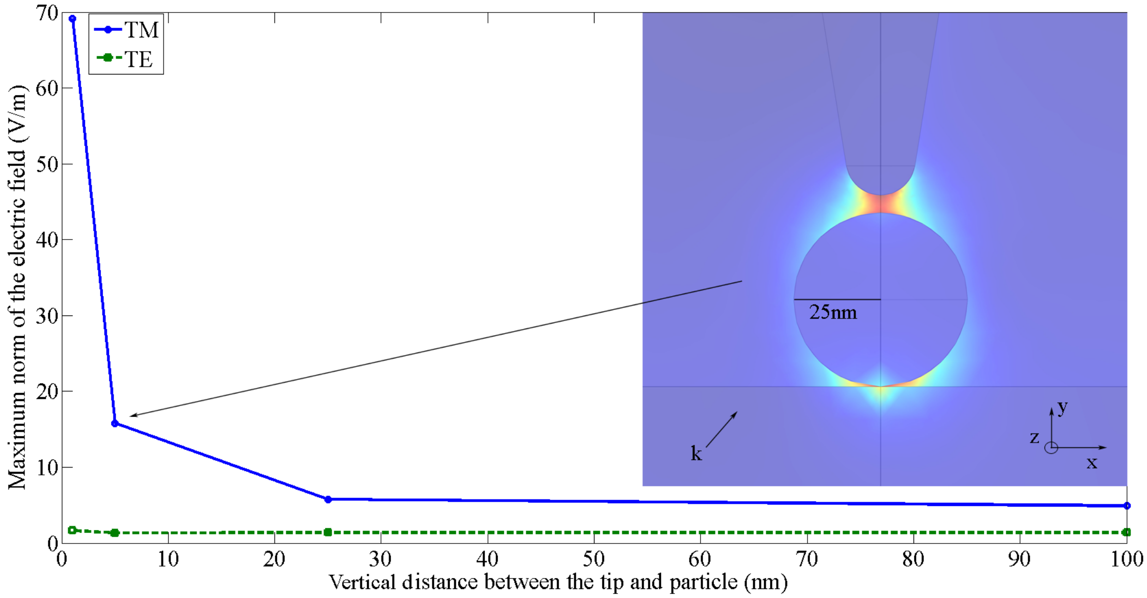

Figure 3.7: Field enhancement as a function of vertical separation between tip and particle. Inset: Cross-sectional plot through the plane of symmetry for the time averaged electric field amplitude with a 5-nm tip-particle separation. Note the localization of the field between tip and particle.

Again for TE polarization, these different vertical distances between tip and particle have little effect. Because of the TE polarization, the electric field is polarized transversely to the tip-particle axis and has little effect on absorption, even at separations approaching 1 nm. Likewise, Figure 3.4 (c) indicates that the absorption spectrum does not change significantly with tip-particle separation for TE polarization. This is expected because of the surface charge distribution, and thus the electric field is concentrated at the sides of the particle and away from the tip. As a result, the tip is only a weak perturbation and does not dramatically affect C_{abs}. In contrast, for TM illumination, the electric field is partially polarized along the tip-particle axis. In this case, charge is concentrated at the top and bottom of the particle, as well as at the silicon tip, and the tip strongly perturbs the electric field around the particle. With decreasing vertical distances between tip and particle, the increasing polarization of the high dielectric constant tip reduces the energy of the configuration [3] and leads to a longer resonance wavelength. As can be seen in Figures 3.4(b and d), the absorption magnitude and resonant wavelength increase and red-shift respectively as the tip approaches the particle.

Effect of a Si tip on AuNP of Different Sizes

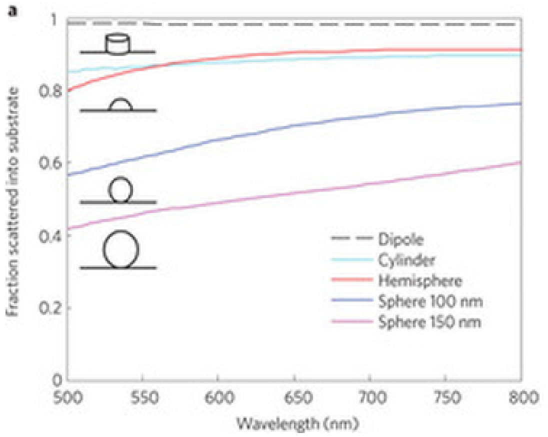

Figure 3.8: Fraction of light, scattered into a silicon substrate for different sizes and shapes of AgNP. Figure reproduced with the permission from Nature Publishing Group [42].

As was described in Sections 2.9.2 and 2.9.3, both absorption and scattering depend on the particle size and shape. This character does not change when the particles are placed on a substrate. In fact, Figure 3.8 shows the fraction of light scattering into a silicon substrate, explaining the dependence of size-shape on coupling efficiency [42]. Likewise, if one is concerned about absorption of a gold nanoparticle sitting on a glass substrate under a silicon tip, different sizes provide different optical absorptions.

For a particle much smaller than the incident wavelength, the absorption cross-section (C_{abs}) is proportional to the radius cubed [36]. A linear increase in the absorption efficiency (Q_{abs}) as a function of diameter is expected because the efficiency is normalized to the geometrical cross-section of the spherical nanoparticle, i.e. $Q_{\text{abs}} = \dfrac{C_{\text{abs}}}{\pi r^2}$. This can be seen in Figure 3.10 for both TE and TM polarization in the absence of the tip. In TE polarization, the presence of the tip does not dramatically alter the absorption of the particle, regardless of size. For TM illumination, the

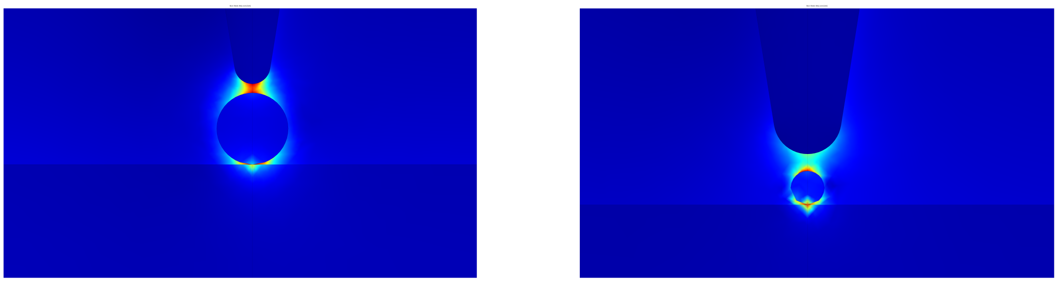

Figure 3.9: Effects of different tip sizes. Left: AuNP diameter 40 nm. Right: AuNP diameter 10 nm. In both cases, the Si tip apex diameter is 20 nm.

tip-induced enhancement in Q_{abs} is significant as shown in Figure 3.10. The greatest enhancement in absorption efficiency is observed when the radius of the particle is smaller than the radius of the tip. This is not surprising because in this case, the tip provides a strong perturbation on the local dielectric environment of the particle. As the particle radius becomes larger than the tip radius, as can be seen from Figure 3.9, the effect of the tip lessens. Still, the tip gives the provision of targeting individual particles from a fabrication point of view. However, a large ratio of tip to particle-radius will sacrifice selectivity if more than one particle is present [86].

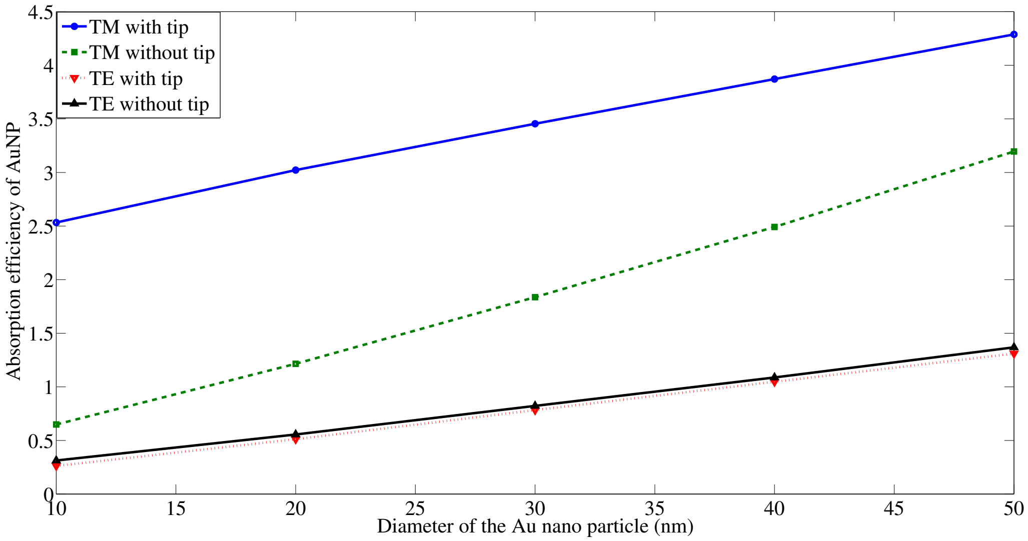

Figure 3.10: Absorption efficiencies of AuNPs of different sizes with a constant 5-nm tip-particle separation. Note the enhancement with the presence of a tip for TM polarization.

3.3.2 Effects of a metallic nanostructure

The tip particle system also shares similarities with coupled plasmonic systems and optical antennas. Related work by Chang et al. reported low absorption losses for self-assembled quasi 1D structures at longer wavelengths [87]. Both absorption and radiation damping for a gold optical antenna and of gold nanoparticle pairs have been analyzed by Kats et al. [88] and Dahmen et al.[89], respectively. However, none of these works explored how the presence of an AFM probe affects the particle absorption at visible wavelengths. Thus, this effort aims to analyze the optical absorption of noble metal nanoparticles, resting on a substrate, under a sharp nanoscale probe, as shown in Figure 1.3.

3.3.3 Temperature modification, caused by the tip

The temperature modification of the tip, along with the field enhancement at the apex of a tip, has attracted much attention, and several groups have measured the temperature changes associated with illuminated tips. McCarthy et al. used Raman Stokes and anti-Stokes scattering from the apex of an AFM tip to characterize the heating dynamics and measure the temperature of the tip [45]. Joule heating at the apex of the tip for TERS applications has been found to be important and has also been studied [90]. Numerically, Chen et al. investigated the near field thermal transport of a metallic tip under laser illumination [21, 91]. In another work, Yue et al. researched non-contact, sub-10 nm temperature measurement in near-field laser heating where they found a 200° C temperature rise for a laser illuminated tip [92]. Also, AFM has been used to probe thermal conductivity with high spatial resolution [93]. In contrast to these efforts, this report focuses on the absorption modulation of a second structure, rather than of the tip itself.

Chapter 4

Simulation setup

4.1 Software used

The RF module of COMSOL Multiphysics 3.5a is used to implement the finite element method (FEM). COMSOL's 3D scattered harmonic propagation mode calculates the difference between a volume source field defined in the absence of a scatterer and the total field in the presence of the scatterer. This difference is referred to as the scattered field, which still provides access to the details of the near field and should not be confused with techniques for calculating the scattered far field.

Comsol Multiphysics can take into account any dispersive, inhomogeneous, anisotropic object. The short description is listed in Table 4.1.

Table 4.1: Brief definitions of material properties.

Property	Constitutive parameters...
Linear	**are not** functions of applied field strength
Homogeneous	**are not** functions of position
Isotropic	**are not** functions of direction
Dispersive	**are** functions of frequency

One can couple the RF module with the Heat transfer module or the Electrostatic module. The Direct solver is very efficient as it has multiple methods to implement, such as Umfpack, Pardiso, and Spooles. All these methods, however, generate a symmetric Jacobina or Stiffness matrix and the system keeps only the upper part after LU factorization. One can accommodate a geometry with triangular, tetrahedral, and hexahedral shaped element. For this problem, as will be discussed in Section 4.4, tetrahedral elements were used [94].

4.2 Geometry

4.2.1 Waveguide in a rectangular domain

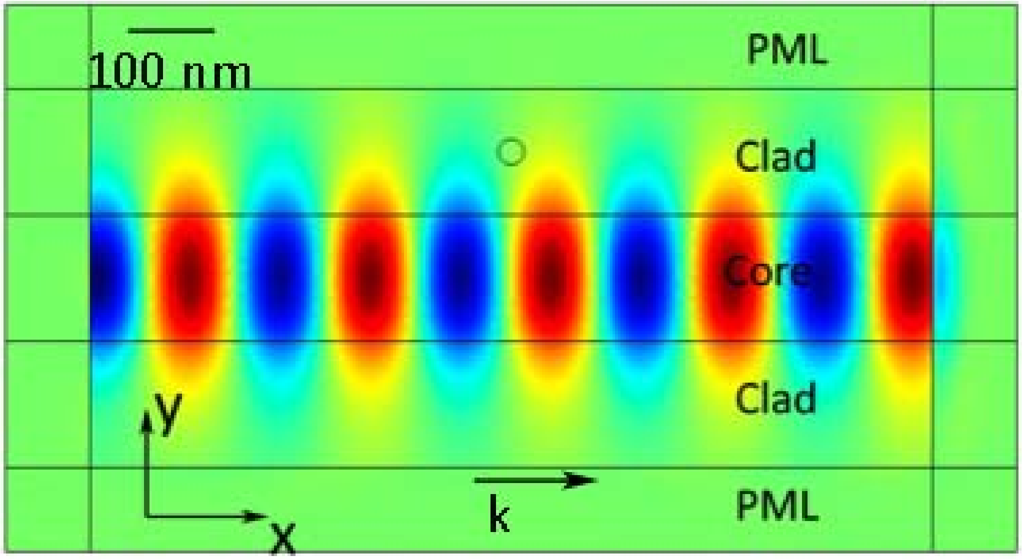

Figure 4.1: Steady state incident electric field inside the structure for single mode propagation. In this simulation, Silicon Nitride is chosen as core, and the clad is BK7 glass, having refractive index of 2.03 and 1.52, respectively at 400 nm incident wavelength. The field is defined everywhere except perfectly matched layer (PML). Inside the core, the maximum intensity of the E field (i.e. deep red) is 0.93 V/m, and minimum (i.e. deep blue) is -0.97 V/m. Note the exponential decay of E field in the clad layers. The entire geometry is covered with a 100 nm thick PML layer that, in conjunction with the absorbing boundary condition, prevents any unwanted reflection

As can be seen from Figure 4.1, a 1200 nm by 600 nm simulation domain has been drawn. The dimensions of the core and cladding has been chosen to allow only single mode propagation through the waveguide. Figure 4.1 shows an x-y cross-section of the excitation field for a 400 nm wavelength (i.e. the geometry is infinite in z-axis). The thickness of the core and each layer is 150 nm. The 100 nm thick PML layer has been chosen depending on author's earlier experience with COMSOL 3.5a. The top and bottom layer is absorbing in y direction only. Likewise, the side layers are absorbing in x direction only, and the corners are absorbing in both x and y directions. One can see from Figure 4.1 that the incident field inside the PML is zero (i.e. light green). Again, the RF module of the software is used to solve for the scattered field everywhere in the domain.

4.2.2 Tip-particle-substrate in a spherical domain

A 600-nm radius spherical simulation domain was divided into two hemispherical half spaces. The lower is the substrate, BK7 glass, and the upper is vacuum, as in Figure 4.2 (b). The domain is surrounded by 100-nm thick perfectly matched layers (PML) [31] backed by scattering boundaries to prevent spurious reflections, which are crucial steps of FEM, as will be discussed in Section A.4.1. A 50-nm diameter gold nanoparticle is placed in contact with the substrate at a single point. In reality, nanoparticles typically contact substrates along a crystal facet; however, simulation of all the varieties of such an interface was impractical for this study. Precaution was taken to limit the search for the maximum electric-field enhancement to the upper hemisphere of the particle. This eliminates any spurious field peaks at the point contact. The details grid dimensions, along with different validations, are provided in Chapter 4.5. The refractive index values for BK7 were taken from Schott [95], while the values for gold were taken from Johnson and Christy [37].

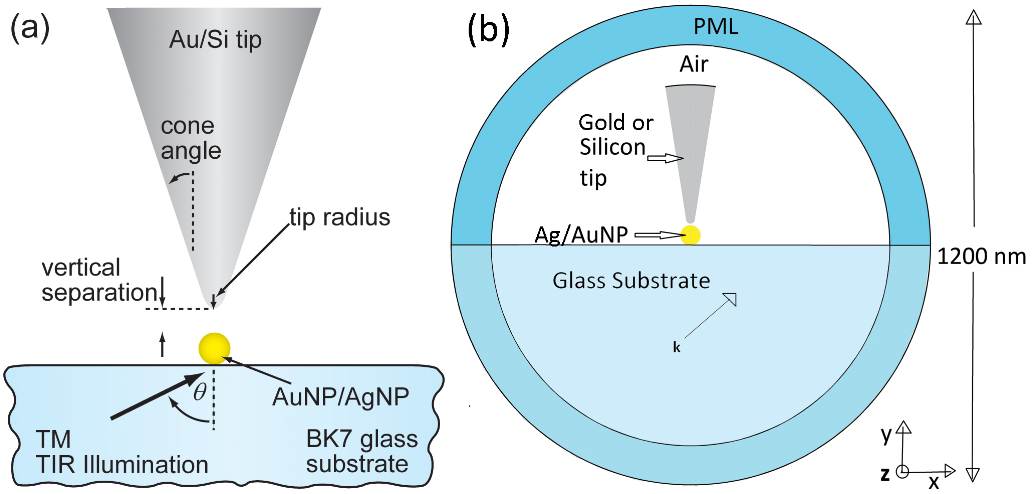

Figure 4.2: (a) Cross-sectional schematic of the geometry of interest. A nanoscale tip is positioned above a nanoparticle and illuminated using total internal reflection. For TM polarization the magnetic field is transverse to the plane of incidence. (b) Cross section of 3D simulation geometry with a truncated Au or Si tip (length= 370 nm, apex radius=10 nm, cone angle θ 10°) suspended 5-nm above a gold or silver nanoparticle on a glass substrate. A 100-nm-thick perfectly matched layer (PML) encloses the simulation domain.

In Figure 4.2, the silicon tip radius is 10 nm and the cone angle is 10° at the apex, based on the nominal dimensions given by the AFM probe manufacturer [26]. The refractive index of silicon was taken from measurements compiled by J. A. Woolam, Inc. and the University of Nebraska, which are very similar to the data listed by Palik [96].

In the simulation, the tip length was truncated to 370 nm. Extending the tip through the PML would have approximated a more realistic structure (several microns in length); however, the scattered field formulation in COMSOL assumes the scattering objects are entirely confined within the physical domain. Illuminating at normal incidence produces a strongly guided wave in the silicon tip. Thus, the choice of tip length can significantly affect the simulation results. However, this wave guiding effect is far weaker when illuminating at oblique incidence beyond the critical angle for glass. The evanescent wave decays exponentially, so by the end of the tip-length the norm of the E field is reduced by more than 30 times compared to the interface under the particle. For example, in TIR illumination, changing the tip length from 370 nm to 670 nm causes no more than only 3.5% difference in C_{abs} of AuNP. Loke and Mengüç have explored the effect of tip truncation using a newly developed Discrete Dipole Approximation with Surface Interactions (DDA-SI) analysis [18].

The gap between the tip and PML was 100 nm or approximately one fifth of a wavelength. This choice of gap allows the mesh elements to remain approximately the same size as in the surrounding vacuum region, and thus has minimal impact on computation time. The vertical and lateral positions of the tip were varied over a range of 1 to 100 nm and -320 to 320 nm respectively. For all the simulations, a single plane of symmetry is used to reduce computation time by half.

4.3 Formulation

To represent the time dependence of an electromagnetic (EM) wave, one can simulate the entire domain for each time step. This method is computationally expensive, and not always required unless there is a relevant time constant, such as if a switch is turned on and off, or if a pulsed excitation is provided. If one can, however, assume that the time variation is sinusoidal and steady state, one can formulate the sinusoidal steady state wave with a frequency domain solution. Contrary to the trigonometric Sine or Cosine formulations of EM wave, complex exponential forms are algebraically easy to deal with; especially when the media is not lossy and the wave is a plane wave. Essentially, the complex value consists both the magnitude and phase of the field, and the frequency is a predefined scaler quantity [94]. Likewise, most of the formulae mentioned in following subsections have time dependent exponential terms, which are omitted. In this dissertation, this kind of solution is referred to as "steady state" solutions. The frequency range was chosen to comfortably accommodate the absorption resonant peak.

The source field is defined based on an infinite plane wave incident from within the substrate, taking advantage of the plane of symmetry as defined before. The source field was defined analytically in the half space, using the Fresnel equations. The software then computes the scattered field at each point of the simulation domain. This approach has two key advantages over launching a wave from a finite source:

$a)$ The computational domain is significantly reduced, because accommodating a plane wave excitation requires the geometry to be extended far enough. This sub-domain formulation makes this system computationally less expensive.

$b)$ The diffraction at the end of the plan or line source is avoided, which would have been far from a realistic system.

Both aspects contrast with two step methods in which one numerically calculates the source field by launching a plane wave from a boundary in the absence of the scatterer, and then uses the resulting field as the input to another simulation to calculate the scattered field [15].

The frequency of the incident, reflected, and transmitted waves are usually the same unless the interface was illuminated with extremely high amplitude causing the oscillator to respond non linearly to the incidence. The process of reflection and transmission is the macroscopic manifestation of scattering occurring on a submicroscopic level. If the transition between two media is gradual, such as over a wavelength or more, the reflection would be very little [39].

Apart from the brief description in Section 2.1, one may consult any fundamental electromagnetic text to understand the boundary conditions. Simple approximations for the materials used in this dissertation for the frequencies of these simulations are as follows.

$a)$ Across an interface, the tangential component of $\vec{E}$ and $\vec{H}$ would be continuous (strictly for relative permeability ≈ 1)

$b)$ Across an interface, the normal component of $\varepsilon\vec{E}$ and $\mu\vec{H}$ would be continuous.

Although the longer wavelengths of light show the wave theory more strongly, and shorter wave exhibits more particle properties [3], most of the simulations are sampled in a range of 200 $\sim$ 400 nm at 5 $\sim$ 7 nm intervals. The time averaged absorbed power was integrated inside the volume of the nanoparticle, and normalized with the incident flux $\frac{1}{2}c_0 n \epsilon_0 E_0^2$, where

n = refractive index of the media the incident wave is coming from, mostly glass,

c_0 = the speed of light,

ϵ_0 = permittivity of the free space, and

E_0 = amplitude of the source field.

The time averaged resistive heating, for example, is defined as follows.

$$\begin{aligned} Q_{\mathrm{av\_rfw}} = 0.5 * \mathrm{Re}(J_{\mathrm{ix\_rfw}} * E'_{\mathrm{x}} - \jmath * \mathrm{Re}(\omega_{\mathrm{rfw}}) * E_{\mathrm{x}} * D'_{\mathrm{x\_rfw}} \; + J_{\mathrm{iy\_rfw}} * E'_{\mathrm{y}} - \\ \jmath\, \mathrm{Re}(\omega_{\mathrm{rfw}}) * E_{\mathrm{y}} D'_{\mathrm{y\_rfw}} + J_{\mathrm{iz\_rfw}} * E'_{\mathrm{z}} - \jmath * \mathrm{Re}(\omega_{\mathrm{rfw}}) * E_{\mathrm{z}} * D'_{\mathrm{z\_rfw}})\ \mathrm{W/m^3} \end{aligned} \tag{4.1}$$

where,

$J_{\mathrm{i\_rfw}}$ = induced current, either x or y or z component A/m,

ω_{rfw} = angular frequency, which is always real,

D_{rfw} = electric displacement, either x or y or z component C/m, and

E is the total electric field component, either x or y or z component.

The primed terms mean complex conjugate. The variables with rfw suffix are readily available from the software. During post-processing, the "recover" option, provided by the software, was selected to yield better accuracy in evaluating the function and its derivative. The post-processing is 2 $\sim$ 5 times slower with this option selected due to the discretization of the variables using Lagrange shape function.

4.3.1 Total Internal Reflection at a glass-air interface

The reflection r_{TE} and transmission t_{TE} coefficients for the TE polarization at the glass-air interface would be:

$$r_{\mathrm{TE}} = \frac{n_1 \cos\theta_1 - n_2 \cos\theta_2}{n_1 \cos\theta_1 + n_2 \cos\theta_2} \tag{4.2}$$

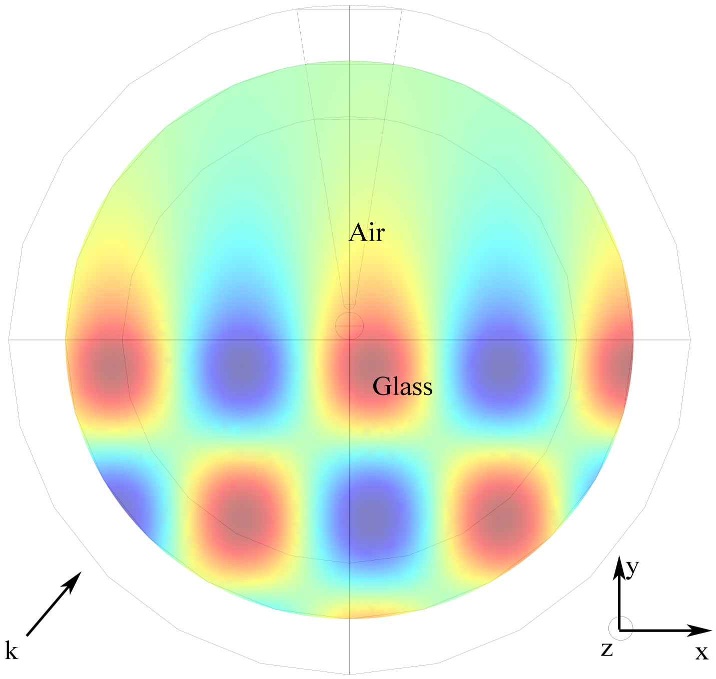

Figure 4.3: TE field excitation at 532 nm and 50° angle of incidence from glass (bottom half-space) to vacuum (top half-space), defined as transverse component of 1 V/m. The juxtaposed pattern is due to the interference between the incident and reflected wave.

$$t_{\mathrm{TE}} = \frac{2n_1 \cos\theta_1}{n_1 \cos\theta_1 + n_2 \cos\theta_2} \tag{4.3}$$

where the refractive index of the glass and vacuum are n_1 and n_2, respectively, and θ_1 and θ_2 are the angles in the first (glass) and the second (vacuum) medium, respectively. Similarly, for the TM polarization, the reflection r_{TM} and transmission t_{TM} coefficients are given by

$$r_{\mathrm{TM}} = \frac{n_2 \cos\theta_1 - n_1 \cos\theta_2}{n_1 \cos\theta_2 + n_2 \cos\theta_1} \tag{4.4}$$

$$t_{\mathrm{TM}} = \frac{2n_1 \cos\theta_1}{n_1 \cos\theta_2 + n_2 \cos\theta_1}. \tag{4.5}$$

Having a complex reflection and transmission coefficient means both the amplitude and phase of the electric field change as the wave reflects or transmits. Some researchers define the volume source field by simulating wave propagation without a scatterer, and using the resulting field as the input to a second simulation with the scatterer present [15]. In this dissertation, however, the source is defined over the entire 3D simulation domain in the absence of the particle and tip. For a TE polarized incident wave, the incident field in first medium (glass) is

$$E_0\Big(\exp^{(-\jmath k_\mathrm{x}x-\jmath k_{\mathrm{y}_1}y)}+r_\mathrm{TE}\exp^{(-\jmath k_\mathrm{x}x+\jmath k_{\mathrm{y}_1}y)}\Big) \tag{4.6}$$

where, $k_\mathrm{x} = k_0 n_1 \sin\theta_1$

$k_{\mathrm{y}_1} = k_0 n_1 \cos\theta_1$

$E_0 = 1$ V/m

the sign is opposite in the second exponential term defining that the reflected wave is going into the negative y direction. As was discussed in Section 3.3.1, the relevant amplitude and phase information is embedded inside the reflection and transmission coefficients, even for a super critical angle with a complex θ_2. The incident field in the second medium (vacuum) for the TE polarized case would be

$$E_0\, t_\mathrm{TE}\exp^{(-\jmath k_\mathrm{x}x-\jmath k_{\mathrm{y}_2}y)} \tag{4.7}$$

where,

$k_{\mathrm{y}_2} = k_0 n_2 \cos\theta_2$.

Figure 4.3 represents the source field.

The TM incident field cannot be described with respect to the transverse component only; rather, the in-plane E_x and E_y components are specified. In the glass medium, the formulae are:

$$E_\mathrm{x} = E_0\cos\theta_1\Big(\exp^{(-\jmath k_\mathrm{x}x-\jmath k_{\mathrm{y}_1}y)}-r_\mathrm{TM}\exp^{(-\jmath k_\mathrm{x}x+\jmath k_{\mathrm{y}_1}y)}\Big) \tag{4.8}$$

$$E_\mathrm{y} = -E_0\sin\theta_1\Big(\exp^{(-\jmath k_\mathrm{x}x-\jmath k_{\mathrm{y}_1}y)}+r_\mathrm{TM}\exp^{(-\jmath k_\mathrm{x}x+\jmath k_{\mathrm{y}_1}y)}\Big). \tag{4.9}$$

Again, the sign is opposite in the second exponential terms being the reflected waves. The E_x component of the TM polarized source field is drawn in Figure 4.7. Likewise, the formulation in the transmission medium (vacuum) are:

$$E_\mathrm{x} = E_0\cos\theta_2\, t_\mathrm{TM}\ \exp^{(-\jmath k_\mathrm{x}x-\jmath k_{\mathrm{y}_2}y)}, \tag{4.10}$$

$$E_\mathrm{y} = -E_0\sin\theta_2\, t_\mathrm{TM}\ \exp^{(-\jmath k_\mathrm{x}x-\jmath k_{\mathrm{y}_2}y)}. \tag{4.11}$$

4.3.2 2D formulation for a symmetric waveguide

The guided mode inside the core, with a thickness of d (centered at the origin), is formulated in cosine for a TE excitation, the field in the core is:

$$E_1 * \cos(k_\mathrm{y} y) \exp(-\jmath\beta x) \qquad \text{for } -\mathrm{d}/2 < \mathrm{y} < \mathrm{d}/2, \tag{4.12}$$

where,

$E_1 = 1$ V/m,

$k_\mathrm{y} = \sqrt{n_\mathrm{core}^2 k_0^2 - \beta^2}$,

where,

$n_\mathrm{core} =$ refractive index of the core,

$k_0 = \dfrac{2\pi}{\lambda}$, free space wavenumber,

$\beta = k_0 n_\mathrm{eff}$, n_eff is the effective refractive index that signifies the allowed modes in the waveguide (i.e. the valid combinations of k_y and γ) [97]. The n_eff for TE should be larger than that for TM, because, TE has more field over the waveguide compared to TM in 2D. At 532 nm, for example, $n_{\mathrm{eff}_\mathrm{TE}} = 1.8$ and $n_{\mathrm{eff}_\mathrm{TM}} = 1.7$ for this configuration. Thus the power propagating in the outer media in TM polarization is larger than that of TE polarization.

The fields in upper and lower claddings should be exponentially decaying, and respectively are:

$$E_2 * \exp(-\gamma y) \exp(-\jmath\beta x) \qquad \text{for y} > \mathrm{d}/2, \text{and} \tag{4.13}$$

$$E_2 * \exp(\gamma y) \exp(-\jmath\beta x) \qquad \text{for y} < -\mathrm{d}/2, \tag{4.14}$$

where,

$E_2 = E_1 \dfrac{\cos(k_\mathrm{y} d/2)}{\exp(\gamma d/2)}$ V/m, because the tangential electric fields should be continuous at the interfaces, and equal at top and bottom interfaces due to the symmetric single mode propagation, and $\gamma = \sqrt{\beta^2 - n_\mathrm{clad}^2 k_0^2}$, n_clad is the refractive index of the clad.

The number of confined modes depends on the waveguide thickness, the frequency, and the refractive indices of core and cladding. Below a specific width, there would be no confined mode, and as the thickness increases, gradually the first and the second order mode propagate [98]. To enforce a single mode propagation, the following value of *M* has to be less than one [33]:

$$M \approx \frac{\sqrt{1 - \left(\frac{n_{\text{clad}}}{n_{\text{core}}}\right)^2}}{\frac{\lambda}{2dn_{\text{core}}}} \tag{4.15}$$

As (4.15) indicates, single mode operation requires low index contrast between core-clad or small core dimension (d). For example, for a $n_{\text{clad}} = 1.52$, $n_{\text{core}} = 2.02685$, and $\lambda = 532$ nm, a core thickness of 150 nm will allow a single mode propagation. Unlike symmetric waveguides, a cutoff frequency exists for asymmetric waveguides, where the upper and lower cladding refractive indexes are unequal. A higher mode has a higher cut off frequency [98].

4.3.3 Surface Plasmon polaritons at a single interface

To excite surface plasmon polaritons between a metal, (an infinite gold substrate), and a dialectic (glass), the electric fields at x and z directions are formulated. The ”idea” is to excite a surface wave (also known as a slow wave, or a surface plasmon). This is supported by a TM mode.

The visible wavelength range ensures the negative real part of the permittivity of gold, as was shown in Figure 2.2. With regard to Figure 4.4, inside the upper hemisphere (vacuum), where $z > 0$, the defined electric field components are

$$E_{\text{x}}(z) = \jmath E_0 \frac{1}{\omega\varepsilon_0\varepsilon_2} k_2 \exp^{\jmath\beta x} \exp^{-k_2 z}, \text{ and} \tag{4.16}$$

$$E_{\text{z}}(z) = -E_0 \frac{\beta}{\omega\varepsilon_0\varepsilon_2} \exp^{\jmath\beta x} \exp^{-k_2 z} \tag{4.17}$$

where,

$\varepsilon_2 = 1$ (dielectric constant of vacuum),

$\varepsilon_0 = 8.854 \times 10^{-12}$ F.m^{-1} (permittivity of vacuum),

$\omega =$ the angular frequency, in terms of wave velocity and wavelength,

$k_2 =$ the component of the wave vector perpendicular to the interface of the two media, dictating the decay length of the field perpendicular to the interface, where

$k_2^2 = \beta^2 - k_0^2\varepsilon_2,$

where,

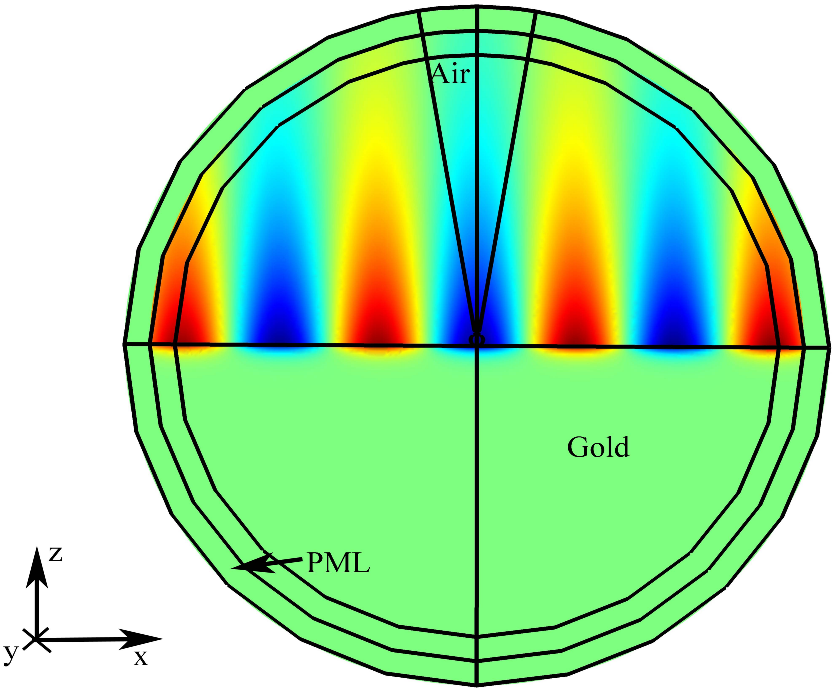

Figure 4.4: Excited SPP (H_y) at a single interface between gold and vacuum. The tip and particle are defined as vacuum and the field is defined inside each sub domain except a 100 nm thick perfectly matched layer (PML). While calculating scattering, the conical structure was defined as the gold tip above the gold nanoparticle. Appendix A.1 shows that the field decays much slower in dielectric than in metal. As was described in Section 2.5.5, the field decays much slower in vacuum than in gold. This is one of the exceptions, where the geometry is drawn in x-z plane.

$$k_0 = \frac{2\pi}{\lambda_0}, \qquad \beta = k_0\sqrt{\frac{\varepsilon_1\varepsilon_2}{\varepsilon_1+\varepsilon_2}},$$

where,

$\varepsilon_1 =$ the permittivity of metal.

With regard to Figure 4.4, in the lower half plane, where $z < 0$, the defined electric field components are [34]:

$$E_\mathrm{x}(z) = -\jmath E_0 \frac{1}{\omega\varepsilon_0\varepsilon_1} k_1 \exp^{\jmath\beta x} \exp^{-k_1 z}, \text{ and} \tag{4.18}$$

$$E_\mathrm{z}(z) = -E_0 \frac{\beta}{\omega\varepsilon_0\varepsilon_1} \exp^{\jmath\beta x} \exp^{-k_1 z} \tag{4.19}$$

where,

$$k_1^2 = \beta^2 - k_0^2\varepsilon_1.$$

However, unlike most other geometrical configuration covered in this report, the substrate is considered to be an infinite gold substrate.

To calculate the absorption cross section, the actual incident flux needed to be calculated. The incident flux was calculated assuming the maximum field enhancement. Weber et al. formulated a general upper limit of field enhancement on the basis of energy conservation [99]. Since the original wave was defined directly as a SPP, this enhancement formulation allowed the calculation of the incident field and hence, the incident flux to evaluate the absorption cross sections.

$$\frac{|E_\mathrm{SP}(0^+)|^2}{|E_0|^2} \simeq \frac{2(-\varepsilon_1')^{\frac{1}{2}}(-\varepsilon_1' - \varepsilon_\mathrm{glass})}{\varepsilon_\mathrm{glass}^{\frac{1}{2}}\varepsilon_1''} \tag{4.20}$$

Equation (4.20) was valid whenever $\varepsilon_1' >> \varepsilon_\mathrm{glass}$. Equation (4.20) provided the maximum field enhancement for the optimum angle of illumination and that gives access to the incident flux based on the formulation outlined above.

4.3.4 Multilayer: water, ITO, and glass

In this section, the formulation for a collaborative project, where a localized surface plasmon resonance sensor is simulated, is detailed. For the corresponding simulations, the light needed to propagate through three different media. In this section the working plane is again the x-y plane. The above formulations must be modified for a three layer medium. Water, indium tin oxide (ITO), and glass, as indicated in Figure 4.5 as medium 1, 2,and 3, respectively, all are transparent to incident light. As is shown in Figure 4.5, for an incidence from inside water, the wave would partially reflect from water-ITO interface. The remaining transmitted wave will have a phase shift once it reaches the ITO-glass interface, and will again partially reflect and transmit the remaining wave into the glass. The transmission matrix takes the individual interface reflection and transmission coefficients as input, and outputs the amplitude at individual medium. The relatively simpler formulation for TE polarization is as follows:

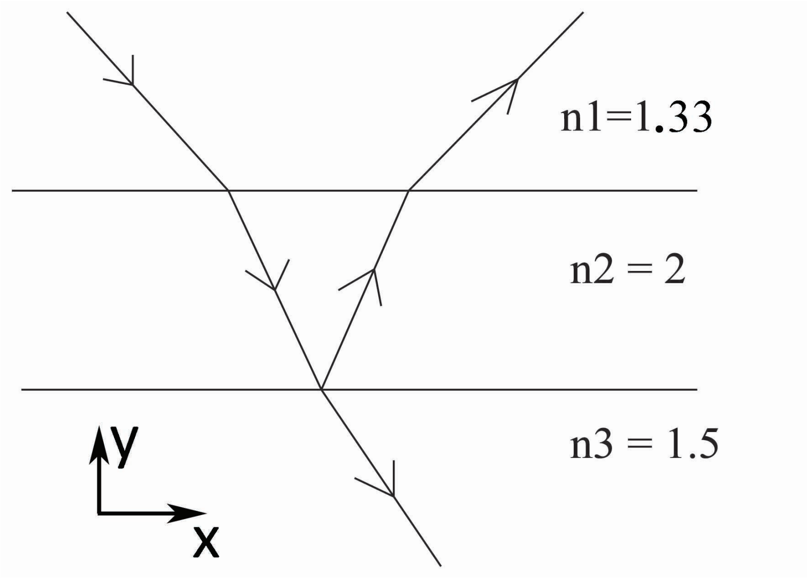

Figure 4.5: Simplified schematic of the multilayer simulation because upon each incidence, there is a corresponding reflection. The formulation derived in this section, however, takes into account all the possible reflection transmissions and is represented at corresponding directions. The thickness of ITO, having the refractive index of 2, is 60 nm. As will be shown in (4.27), the phase shift, as the wave reaches the ITO-glass interface because of the phase lag compared to the free space propagation, is a function of the traversed length through the dielectric medium. Again, the tangential wave vector component k_x will be same across all the interfaces, but the vertical components of wave vector will be $k_{\mathrm{y}1}, k_{\mathrm{y}2}, k_{\mathrm{y}3}$ in first, second, and third medium, respectively.

$$r_{12} = \frac{n_1 \cos\theta_1 - n_2 \cos\theta_2}{n_1 \cos\theta_1 + n_2 \cos\theta_2} \tag{4.21}$$

$$t_{12} = \frac{2n_1 \cos\theta_1}{n_1 \cos\theta_1 + n_2 \cos\theta_2} \tag{4.22}$$

where,

r_{12} = reflection coefficient between water-ITO,

t_{12} = transmission coefficient between water-ITO,

$n_1 = 1.33$, refractive index of water,

$n_2 = 2$ refractive index of ITO, and

$\theta_1 = 43.3833°$, angle of incidence, which is calculated based on the objective used in the experiment.

Similarly, the reflection and transmission coefficients for ITO-glass interface can be defined as

$$r_{23} = \frac{n_2 \cos\theta_2 - n_3 \cos\theta_3}{n_2 \cos\theta_2 + n_3 \cos\theta_3} \tag{4.23}$$

$$t_{23} = \frac{2n_2 \cos\theta_2}{n_2 \cos\theta_2 + n_3 \cos\theta_3} \tag{4.24}$$

where,

$\theta_2 = \Big(\arcsin(\frac{n_1 \sin\theta_1}{n_2})\Big)'$, the refracted angle in ITO, and

$n_3 = 1.5$, refractive index of glass.

Using the transmission matrix, one can derive the individual amplitude of the electric field in each medium. In water, to start with, the incident electric field would be

$$E_1 = A_1^+ \exp^{-\jmath k_\mathrm{x} x + \jmath k_\mathrm{y1} y} + A_1^- \exp^{-\jmath k_\mathrm{x} x - \jmath k_\mathrm{y1} y} \ \mathrm{V/m} \tag{4.25}$$

where,

A_1^+ = the amplitude of the wave incident on water-ITO interface, and

A_1^- = the amplitude of the reflected wave, going back to the positive y direction.

As before, k_x and k_y1 are the directional components of the wave vector; horizontal wave vectors should be continuous and be the same across all the media, and vertical wave vectors should be discontinuous, having different expressions in different media.

Similarly, the incident field at the second and third media, respectively, would be

$$E_2 = A_2^+ \exp^{-\jmath k_\mathrm{x} x + \jmath k_\mathrm{y2} y} + A_2^- \exp^{-\jmath k_\mathrm{x} x - \jmath k_\mathrm{y2} y} \ \mathrm{V/m} \tag{4.26}$$

$$E_3 = A_3^+ \exp^{-\jmath k_\mathrm{x} x + \jmath k_\mathrm{y3}(y + \mathrm{ito})} \ \mathrm{V/m} \tag{4.27}$$

where,

ito $= 60$ nm, the thickness of the ITO layer (the interface is at $y = -$ ito),

$k_{\mathrm{y3}} = k_0 n_3 \cos\theta_3$, and

$\theta_3 = \Big(\arcsin(\frac{n_2 \sin\theta_2}{n_3})\Big)'$, the transmitted angle in glass.

Here, the conjugation is due to the sign convention of the software for the propagating wave expressions, and for corresponding material properties. As a result, if this complex angle were not conjugated, the evanescent field would have increased exponentially, instead of decreased exponentially. However, this conjugation is not necessary when the refractive index of the second media is complex.

The amplitude of the first medium, $A_1^+ = 1$ V/m, and with regard to Figure 4.5, the remaining derived amplitudes are

$$A_1^- = A_3^+ \frac{r_{12}\exp^{\jmath k_{\mathrm{y2}}\,\mathrm{ito}} + r_{23}\exp^{-\jmath k_{\mathrm{y2}}\,\mathrm{ito}}}{t_{12}t_{23}},$$

$$A_2^+ = (1 - \frac{r_{12}(r_{12} - A_1^-)}{r_{12}^2 - 1})t_{12},$$

$$A_2^- = \frac{(r_{12} - A_1^-)t_{12}}{r_{12}^2 - 1},$$

$$A_3^+ = A_1^+ (\frac{\exp^{\jmath k_{\mathrm{y2}}\,\mathrm{ito}} + r_{12}r_{23}\exp^{-\jmath k_{\mathrm{y2}}\,\mathrm{ito}}}{t_{12}t_{23}})^{-1}, \text{ and}$$

$A_3^- = 0$, because there is no further interface to reflect off.

Similarly, one can derive the three media TM formulation for individual x and y components, as was done assuming half space in Section 4.3.1.

4.3.5 Benchmarking discrete dipole approximation with surface interaction

The dispersion of the refractive indices of the materials used in the models for this collaborative project are calculated using continuous functions instead of measured data; for Au, the Drude-critical points [100] formula is used and for BK7 borosilicate glass, the Sellmeier equation [101] is used, as in Figure 4.6. The reason behind using the analytical function for the dispersion is to

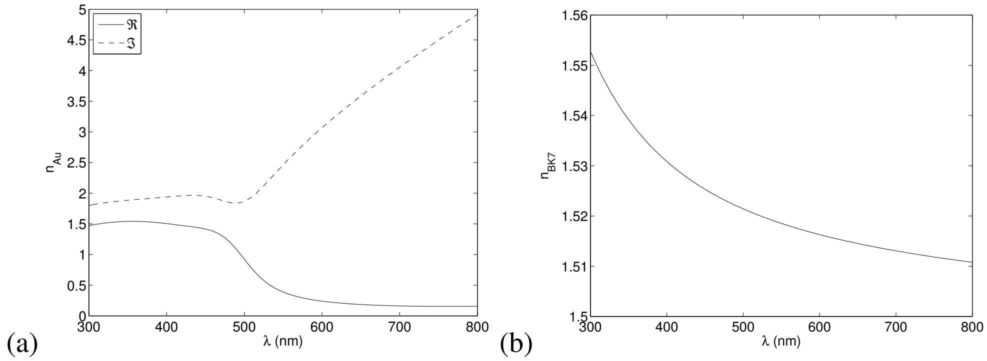

Figure 4.6: Refractive index dispersions of (a) Au calculated using the Drude-critical points model and of (b) BK7 glass calculated using the Sellmeier equation. Figure courtesy of Vincent Loke.

address the fundamental incompatibility between the frequency domain measured dispersion data versus the FDTD method which is a time domain method [102].

Unlike most of the simulations of this dissertation where an evanescent illumination was used, for this section, some simulations were conducted with a normal (0°) illumination. The linearly polarized incident wave, as was described in Section 2.2, descended normal to the substrate.

As before, the absorption cross-section is calculated using $C_{\text{abs}} = 2 * Q_{\text{av}}\_\text{rfw}/\text{P0}$, where Q_{av}_rfw is a COMSOL variable for the resistive heating, volume integrated in half of the particle and

$\text{P0} = \text{E0}^2 * 0.5 * \text{c0\_rfw} * \text{epsilon0\_rfw} * \text{n1}$ is the incident flux. Here the variables with the 'rfw' suffix are inherently available in COMSOL [94]. To calculate the scattering cross section, scattered normal flux is integrated over a fictitious boundary enclosing the nanoparticle:

$C_{\text{sca}} = 2 * \text{nscPoav}/\text{P0}$

where

x, y and z-components of the scattered flux,

$\text{scPoxav} = 0.5 * \text{Re}(\text{sc}E_{\text{y}} * \text{sc}H'_{\text{z}}\text{-sc}E_{\text{z}} * \text{sc}H'_{\text{y}})$,

$\text{scPoyav} = 0.5 * \text{Re}(\text{sc}E_{\text{z}} * \text{sc}H'_{\text{x}}\text{-sc}E_{\text{x}} * \text{sc}H'_{\text{z}})$,

$\text{scPozav} = 0.5 * \text{Re}(\text{sc}E_{\text{x}} * \text{sc}H'_{\text{y}}\text{-sc}E_{\text{y}} * \text{sc}H'_{\text{x}})$,

scattered normal flux,

nscPoav =onx*scPoxav+ony*scPoyav+onz*scPozav,

sign factor for the outward normals to interior boundary,

ofact = if(nx*x+ny*y+nz*z>= $0, 1, -1$), which forces the normal vector to be outgoing, and the x, y and z-components of the outward normals to interior boundary:

onx = nx*ofact,

ony = ny*ofact, and

onz = nz*ofact.

Here, the 'sc' prefix means the scattered field component and primed components are the complex conjugates. With regard to Figure 4.3, the fictitious boundary is the innermost circle enclosing the geometry of interest. As is shown in Section 2.10.1, however, a couple of simulations were still conducted at total internal reflection at a 60 ° angle of illumination. For further clarification of the geometry, formulation, and results, readers are requested to consult the original article of Loke et al [64].

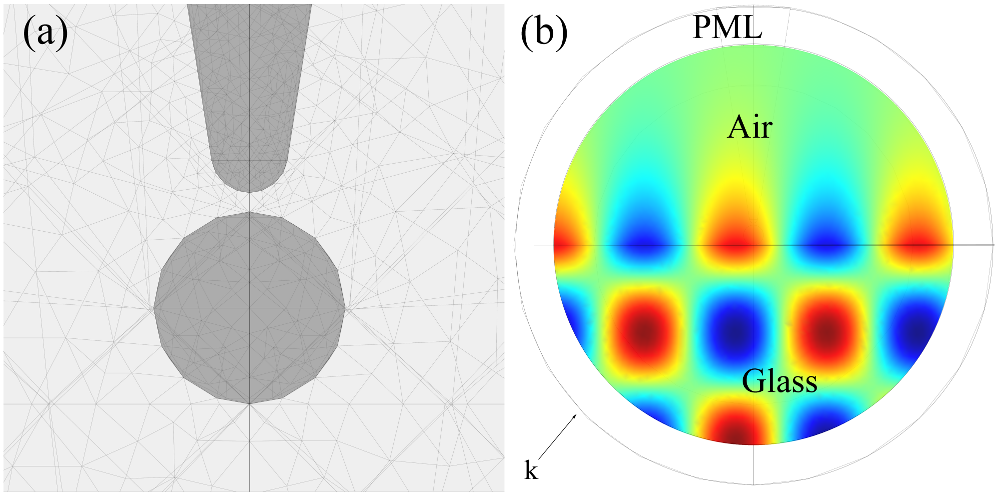

Figure 4.7: (a) Magnified cross section of the mesh elements in and around the nanoparticle. There are 359 tetrahedral mesh elements inside the nanoparticle where the absorption was integrated. There are 2745 elements inside the truncated tip. The number of elements within and between the tip and particle was varied to ensure convergence of C_{abs}. (b) Cross sectional electric-field plot of the E_{x} component of a TM polarized incident wave without the tip and particle present. The source field is defined throughout the simulation volume, except within the perfectly matched layer, by using the Fresnel equations. Then the scattered and total fields are calculated after inserting the particle and tip.

4.4 Meshing

By default, the maximum element size is $\frac{1}{15}$ th of the longest length of the geometry. The usual practice is to set the mesh size to be $\frac{1}{6}$ th of the wavelength in that medium. Furthermore, at the vicinity of the metal surface, the mesh needed to be finer. However, when there is a curvature, mesh curvature is the factor, providing the active constraint. It is recommended to avoid sharp corners, because that would increase the calculation time significantly and may cause a singularity. There are two ways of looking at this: one may want to avoid sharp corners from a physical point of view. That is, corners will have a different impact on field enhancement. In such a case, one would want to model them accurately. Or, if one has a smooth surface, one should avoid a sharp corner due to poor discretization (or meshing).The same geometry was used for all simulations in order to ensure consistent meshing, an example of which is shown in Figure 4.7 (a). Therefore, to model a suspended particle in free space, every subdomain except for AuNP is defined with refractive index, n =1. Likewise, for simulations without the tip, the tip subdomain was defined with refractive index 1. The AuNP had 359 mesh elements. In the software, the maximum mesh element sizes in the tip, PML, and remaining sub domains were 50 nm, 150 nm, and 75 nm respectively. Mesh element sizes were varied because the free space wavelength will change upon entering a medium with higher refractive index. These chosen numbers provided the sufficient number of elements to yield enough accuracy, as described in Figure 4.7 (a) and Chapter 4.5. Table 4.2 describes a mesh example, used for most of the simulations.

Table 4.2: An example of mesh statistics

Extended mesh:	
Number of degrees of freedom	245282
Base mesh:	
Number of mesh points	7248
Number of elements Tetrahedral Prism Hexahedral	37122 37122 0 0
Number of boundary elements Triangular Quadrilateral	8246 8246 0
Number of edge elements	641
Number of vertex elements	34
Minimum element quality	0.2449
Element volume ratio	1.67×10^{-5}

The data of table 4.2 was the result of using mostly predefined mesh elements. The element volume ratio is the ratio of the smallest to largest volume in a given layer of the model. Minimum element quality is a measure of the mesh quality, and should always be 0.01 or higher. Ideally, one wants to have a regular mesh with nodes roughly on the surface of a sphere and with even length edges, such that small displacements are roughly equally distributed among all sub-items. Furthermore, the gradient of the variables, intended to solved, should not be significant over the element volume, such that the gradient can be captured with sufficient precision. For the more accurate results, one needs the higher number of nodes per elements along with the higher shape functions and highest mesh quality. Often, to achieve sufficient precision, one must dedicate ample computational time. Larger computational times, however, can be mitigated by enforcing a plane of symmetry in the simulation [94]. To achieve symmetric E field, a perfect magnetic conductor (PMC), and for symmetric H field, a perfect electric conductor (PEC) has been used. Rather for an even electric field about the plane of symmetry (relative to the tangential field), a PMC is placed in the plane of symmetry For an odd electric field, a PEC is placed in the plane of symmetry.

The relative density of the meshing in different domains can be seen in Figure 4.7. These parameters were optimized to run a single wavelength simulation using dual Intel Xeon quad core processors (2.27 GHz and 24GB RAM) in 128 s. Refining the mesh further or inserting more elements between the tip and particle did not change the optical absorption by more than 5%. Inserting 1000 elements instead of 1 between the tip and particle did not change the C_{abs} of AuNP more than 1%. Reducing the maximum element size from 75 nm to 50 nm in the substrate and vacuum domains reduced the error compared to Mie theory from 5%, as is plotted in Figure 3.4, to 2% but required 27 times longer simulations, as was described in Table 4.3.

Table 4.3: Error with respect to Mie for different meshing size in different domain.

Maximum element size		For the simulation of a specific angle at 532 nm wavelength			
Sub domain	PML	Degrees of freedom	Time for one simulation (s)	Number of elements in AuNP	Error compared to Mie
75 nm	150 nm	402478	660	359	+/- 5%
50 nm	100 nm	1236108	18000	1841	+/- 2%

4.5 Validation of simulation

4.5.1 Comparison to Mie Theory

First, the simulations were compared with Lorenz-Mie [27] theory, as was briefly mentioned in Section 3.2.1, for a 50 nm diameter gold particle surrounded by vacuum. The geometry is shown in Figure 4.8(a). The C_{abs} was calculated for both TE and TM polarization waves (defined with respect to the symmetry plane, but physically indistinguishable). Over the wavelength range from 450 to 650 nm, the worst-case deviation between the analytical and finite element absorption cross sections was 5%, as will be shown by the results in Figure 3.4.

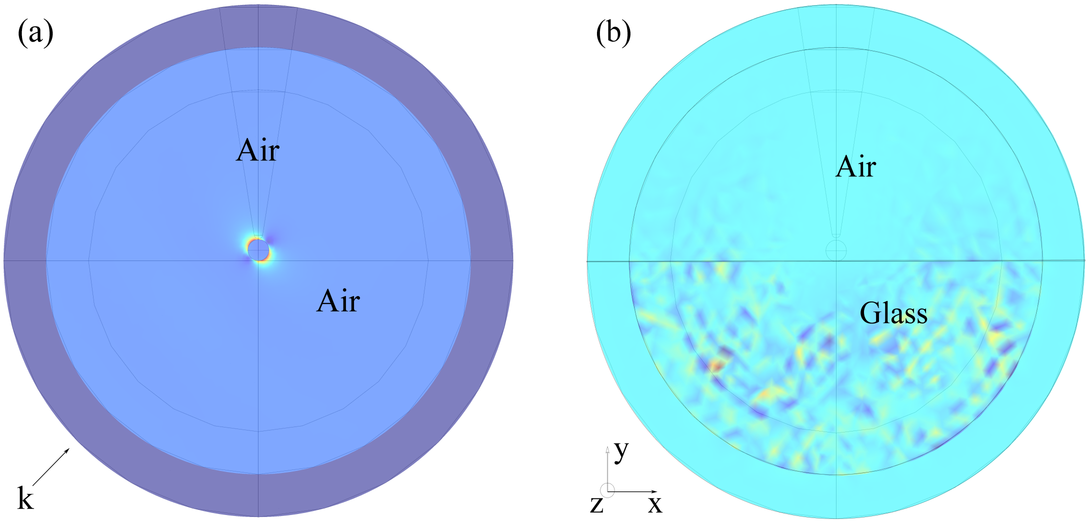

Figure 4.8: (a) Norm of the electric field ($\sqrt{E_{\text{x}}E_{\text{x}}^{*} + E_{\text{y}}E_{\text{y}}^{*} + E_{\text{z}}E_{\text{z}}^{*}}$) for Mie validation, as plotted in Figure 3.4 (a), with values ranging from (blue) zero to (red) 3.724 V/m. The substrate and tip regions were defined as vacuum (refractive index n =1). Note the orientation of field around the AuNP due to the oblique 1 V/m amplitude of E_{x} and E_{y} incidence. (b) Scattered magnetic field (H_{z}) for a perfectly smooth glass substrate only without AuNP. Tip and particle were defined as vacuum (refractive index, n =1). The maximum value ranges between +/- 6.77 $\times 10^{-7}$ A/m for incident E field amplitude of $E_{\text{x}} = 6.43 \times 10^{-1}$ V/m and $E_{\text{y}} = 7.66 \times 10^{-1}$ V/m incidence at 532 nm. In both (a) and (b), the magnitude of field inside PML is very small, implying almost no reflection off the outermost scattering boundary, cutting off the simulation domain.

4.5.2 Zero Scattered Field

Next, the simulation was run with the lower half-space as BK7 but without any scatterer in the simulation domain as shown in Figure 4.8(b). In this case, any non-zero scattered field is the result of numerical errors or unphysical reflections from the boundaries. In fact, the maximum magnitude of the scattered field was found to be 3 orders of magnitude lower than the source field in this case of Figure 4.8(b). The mean of the norm of the electric field ($\sqrt{E_{\mathrm{x}}E_{\mathrm{x}}^{*} + E_{\mathrm{y}}E_{\mathrm{y}}^{*} + E_{\mathrm{z}}E_{\mathrm{z}}^{*}}$) was found to be 3 orders of magnitude lower.

4.5.3 Normal Incidence for TE and TM polarization

The geometry, with or without a tip, is azimuthally symmetric, provided the tip is not laterally offset from the nanoparticle. For normally incident illumination, as in Figure 4.9, there is no physical difference between TE and TM polarized waves; however, the electric field is oriented differently with respect to the symmetry plane. Thus, it is important to confirm that the polarization does not significantly affect the results. In fact, with only a particle on the substrate, the absorption in the AuNP at normal incidence differed by no more than 0.2% between TE (4.9(a)) and TM (4.9(b)). The simulations were conducted from 450 to 650 nm wavelengths.

It was intended to formulate the TM polarization with the help of the magnetic field only to avoid the extended in-plane formulation of x and y components of electric field. Further, the corresponding reflection and transmission coefficients were derived. However, for unknown reasons, H field formulation resulted in about 15% difference between the normal incidence for TE and TM. Therefore, the E field formulations were used for both TE and TM.

4.5.4 Convergence of results

The complete geometry (tip, particle, and substrate) was checked for convergence by enlarging the domain from a 600 nm radius to 1.4 μm radius incrementally by 200 nm for each polarization. In the worst case with a 60° angle of incidence, it deviated less than 0.6% between 600 nm and 800 nm, listed in Table 4.4. Therefore, 600 nm was chosen to reduce the computational time [103].

Table 4.4: Convergence check for TE polarized illumination at 532 nm and 60° angle of incidence with tip-particle-substrate present. C_{abs}: absorption cross-section of 50-nm-diameter AuNP.

Radius of the domain	$C_{\mathrm{abs}} \times 10^{-15}(\mathrm{m}^2)$
600 nm	1.34
800 nm	1.35
1 μm	1.34
1.2 μm	1.35
1.4 μm	1.35

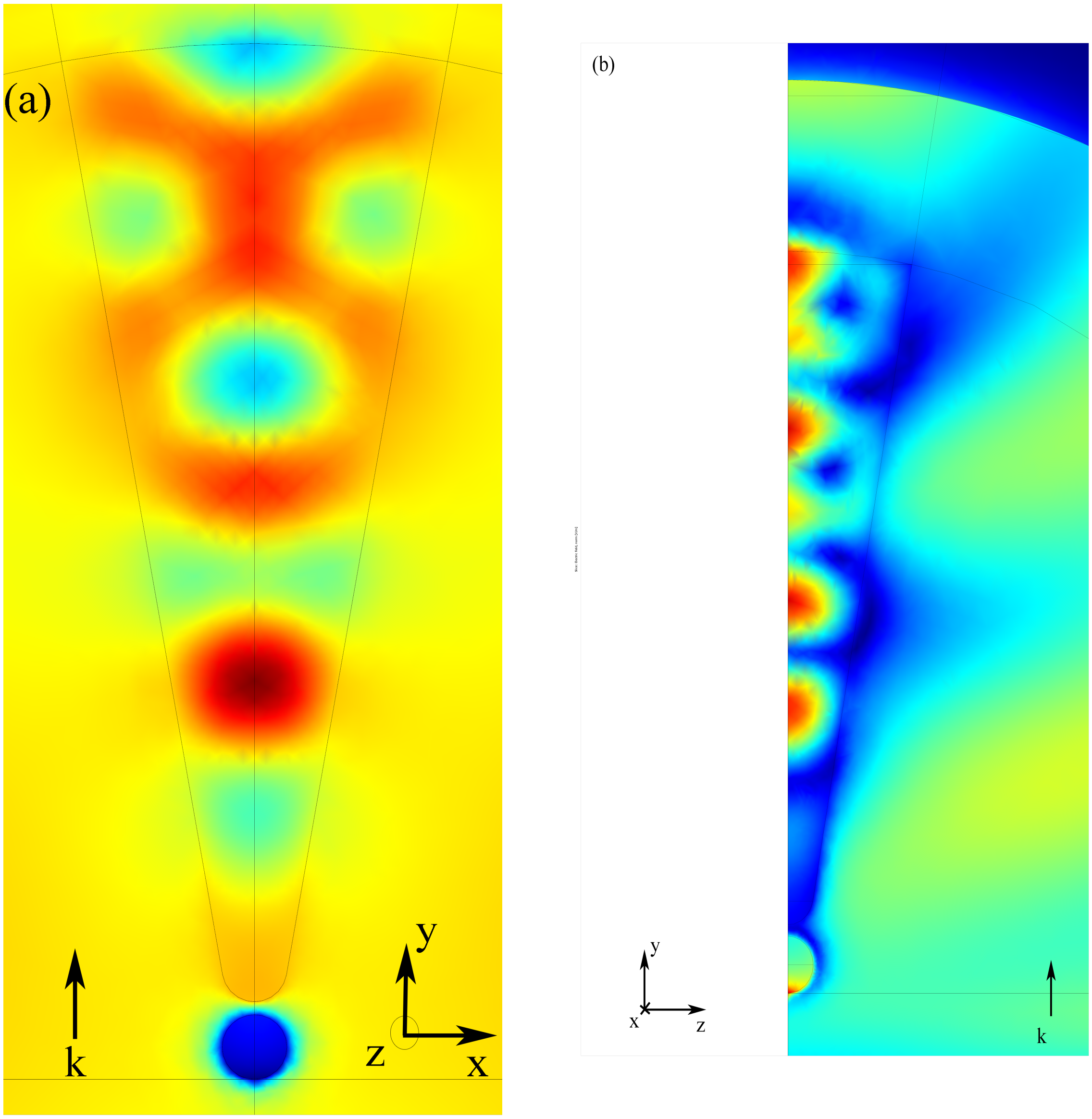

Figure 4.9: (a) Norm of the electric field ($\sqrt{E_\mathrm{x}E_\mathrm{x}^* + E_\mathrm{y}E_\mathrm{y}^* + E_\mathrm{z}E_\mathrm{z}^*}$) for TE illumination. (b) Norm of the electric field for TM illumination. In both cases, the incident was 0°. TE and TM should give the same result in a plane rotated by 90-degrees. Here the output fields in the rotated plane is shown to compare (x-y vs. z-y). The tip, particle and substrate were defined according to the description in Section 4.2. The strong waveguide effect at normal incidence of the Si tip is notable in both cases.

4.6 Parameters for curve fitting

With regard to the harmonic oscillator model, as is discussed in Section 5.1.1, this section describes the corresponding calculated parameters to fit the harmonic oscillator equation. The volume of a 50 nm particle is $\frac{4}{3}\pi(25e^{-9})^3 = 6.545e^{-23}\ \mathrm{m}^3$. With regard to this particle, different starting values as well as the limits for the fitting Equation (5.1) will be derived in the following two subsections.

4.6.1 Calculating upper limits

As was mentioned in Table 2.3, the free electron density of silver is $5.86{\times}10^{28}\ \mathrm{m}^{-3}$, therefore, number of free electrons in a 50 nm AgNP are, $5.86 \times 10^{28} \times 6.55e \times 10^{-23} = 3.84 \times 10^6$, hence, upper limit of participating charge is $3.84 \times 10^6 \times\ 1.6 \times 10^{-19} = 6.14 \times 10^{-13}$ C.

To limit the number of fitting parameters, one can express mass, *m*, in terms of charge, *q*; because, the ratio of charge and mass should be a constant.

$$\frac{q}{m} = \frac{1.6 \times 10^{-19}}{9.11 \times 10^{-31} \times \mathrm{m_0}}.$$

Again, using the value from Table 2.3, the ratio $\frac{q}{m} = 1.83 \times 10^{11}$, and $m = 5.45 \times 10^{-12} q$, because the effective mass is assumed to be 0.96.

The resonant frequency, ω_0, was inserted manually from the simulated data while fitting the equation. The remaining variables of the harmonic osccilatowere equation was fitted by the Matlab Curve Fitting Toolbox. One example parameter list is shown in Table 4.5.

Table 4.5: Example Fit options of Curve Fitting Toolbox of Matlab R2011b [104].

Unknonws	StartPoint	Lower	Upper
E	1	-Inf	Inf
β	$5.15e^{14}$	0	Inf
q	$9e^{-14}$	0	$6.14e^{-13}$

Similar calculations were conducted for gold nanoparticles. Apart from the surface plasmon polaritons, however, gold has a very asymmetric absorption spectrum, compared to silver. Therefore, the entire wavelength range was not utilized, as is shown in Figure 5.7.

It will be described in Section 5.1.4, that since the values of β and q have a difference of around 27 orders of magnitude, the individual starting values of Table 4.5 were varied manually for best possible fit.

Chapter 5

Results and Discussion

5.1 Absorption modification under different geometric conditions

5.1.1 Harmonic oscillator model for particle absorption

In the context of the perturbation caused by the tips, a deeper understanding of these absorption modifications can be obtained by modeling the system as a harmonic oscillator (HO) and considering the probe's effect on both the driving force and damping of the oscillation. As has been demonstrated by Nordlander's group, one can often model the absorption of a plasmonic system with a damped harmonic oscillator [105]. In this case, the numerically calculated absorption data were compared with the HO equation of time-averaged absorption.

$$< P(t) >= \frac{F_0^2 \beta}{2m} \frac{\omega^2}{[(\omega_0^2 - \omega^2) + (\beta\omega)^2]} \tag{5.1}$$

where,

$F_0 =$ driving force,

$\beta =$ total damping,

$m =$ total electron mass, and

$\omega_0 =$ the resonant frequency.

In addition, $F_0 = qE$,

where,

$q =$ the total free electron charge, and

$E =$ the driving electric field.

As the effective masses for electrons in Ag and Au, 0.96 m_0 and 1.0 m_0 were used, respectively [37]. According to the HO model in (5.1), absorption enhancement can result from an increased driving force (F_0) and/or a reduced damping factor (β). β contains both absorptive/resistive and radiative damping terms; as a result, an increase in the radiative component (due to scattering from the tip) could reduce the absorption of the particle (not the absorptive damping term, but the actual absorption). The AgNP has a more symmetric Lorentzian line-shape for absorption and offers a better fit to the HO model. However, AuNPs can also be well fitted provided the spectrum is truncated near the interband transition.

To better understand the interaction between β and F_0, first the well-understood configuration of a spherical particle in a homogenous medium is considered. Specifically, the absorption of a AgNP and a AuNP surrounded by vacuum and glass is considered. The calculated C_{abs}, as shown in Figure 5.1, is found to have a $\approx 20\%$ suppression of C_{abs} along with a significant red shift compared to a AgNP suspended in vacuum. Since the incident field was 1 V/m, in the absence of a perturbing structure, F_0 is directly proportional to q.

The red shifting can be explained in terms of a reduced restoring force, k, due to the change of permittivity of the surrounding media [106]. Using the harmonic oscillator model, as will be discussed in Section 5.1.1, the absorption suppression for the AgNP can be described as a result of increased damping, which dominates over the increased charge participation and driving force. When the AgNP is surrounded by a higher dielectric constant material, both the charge participation and scattering from the particle increase. However, the additional damping from the scattering leads to a reduced absorption, implying that the scattering and hence damping has increased sufficiently to suppress the absorption of a AgNP.

In contrast, when glass surrounds the AuNP, the increased driving force (through increased charge participation) and the slightly reduced damping both contribute to a four times higher absorption. The scattering from the gold particle increases slightly, but the damping due to absorption is slightly reduced because the resonance moves away from gold's interband transition. Once the AuNP is surrounded by glass, and the absorption peak is red shifted about 40 nm, the absorption curves appear closer to the Lorentzian shape, as can be seen from Figure 5.1(b). Of course, these

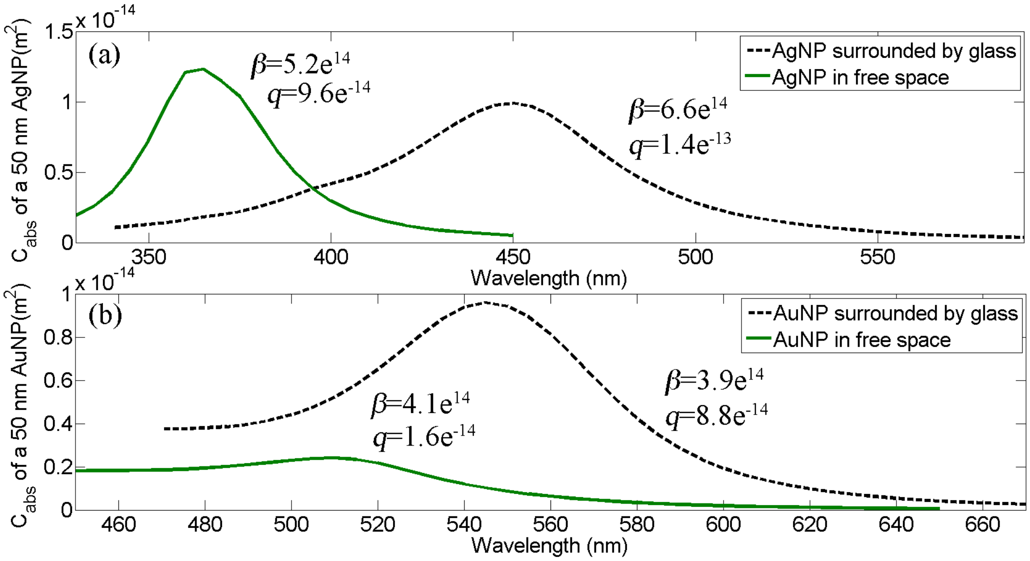

Figure 5.1: (a) C_{abs} of a AgNP suspended in vacuum (green) and in glass (black), and (b) C_{abs} of AuNP suspended in vacuum (green) and in glass (black). The red shifting results from the reduced force constant, *k*, in the harmonic oscillator model. The absorption is directly related to the participating charge, q, and damping, β. For (a), the absorption suppression is a result of increased damping, which overcomes the increased charge participation. However, the absorption is enhanced when the increased charge participation overcomes the increased damping.

observations can also be explained in terms of the dielectric constant of the materials; however, the harmonic oscillator model provides physical insight into how the material properties combine with the particle geometry to yield the well-known absorption and scattering results.

The R^2, which is a measure of the goodness of fit, is defined as

$$R^2 = 1 - \frac{SS_{\text{resid}}}{SS_{\text{total}}} \tag{5.2}$$

where,

SS_{resid} = the sum of the squared residual value from the regression, and

SS_{total} = the sum of the squared differences from the mean of the dependent variable [104].

The closer R^2 is to 1, the better is the fit.

When these observations are connected to the tip-particle system, one will see that the increased scattering introduced by the tip contributes to the modification of the absorption of the AgNP and the AuNP by modulating the driving field and increasing damping. The first two rows of Table 5.1

Table 5.1: Fitted parameters for the harmonic oscillator model for different geometries. All cases are compared to the unperturbed case. The top two grey rows show the comparison with particles suspended in vacuum. The bottom four rows show the comparison with particles on a substrate but in the absence of a tip. The dominant factor influencing C_{abs} is identified, and Both indicates that both factors influence C_{abs} in the same way.

Case	F_0	β	C_{abs}	Dominant factor	R^2
AuNP in glass	470% ↑	4.9% ↓	300% ↑	Both	0.97
AgNP in glass	50%↑	28% ↑	20% ↓	β	0.97
AuNP Si tip	15% ↑	3.6% ↑	20% ↑	F_0	0.98
AuNP Au tip	14% ↓	2.4% ↓	25% ↓	F_0	0.98
AgNP Si tip	4.4% ↓	31% ↑	25% ↓	Both	0.90
AgNP Au tip	9.9% ↓	14% ↑	25% ↓	Both	0.99

show the comparison of the fitted components compared to those in glass. The bottom four rows show the comparison with the tip being present as discussed later.

5.1.2 Dielectric vs metallic tips

On a gold substrate under SPP for a gold nanoparticle only

This section focuses on the effect of a tip above a particle that is submerged in the electric field of an SPP. In the context of the formulations, defined in Section 4.3.3, a silicon tip had quite a different effect on a gold nanoparticle, compared to that of a gold tip. As was described in Section 4.2.2, the truncated tip is suspended on the SPP submerged nano particle, and the setup looks like Figure 4.4. The goal is to study the comparative effects of dielectric and metallic tips on the particle absorption.

Figure 5.2 represents the simulated data points (dot) with the fitted equations (lines). The red dashed line corresponds to the fitted HO equation with the fitted parameters under a silicon tip. The data under “no tip” and Au tip corresponds to the blue solid and black dash-dot lines, respectively. The fitted values for individual variables are listed in Table 5.2.

Table 5.2: Fitted parameters, with regard to Figure 5.2.

Combination	β	F_0	Comparison	R^2
AuNP and no tip	1.8×10^{14}	7.32×10^{-12}	Reference	0.96
AuNP and Si tip	2.0×10^{14}	9.05×10^{-12}	Absorption increases	0.99
AuNP and Au tip	2.5×10^{14}	4.46×10^{-12}	Absorption decreases	0.92

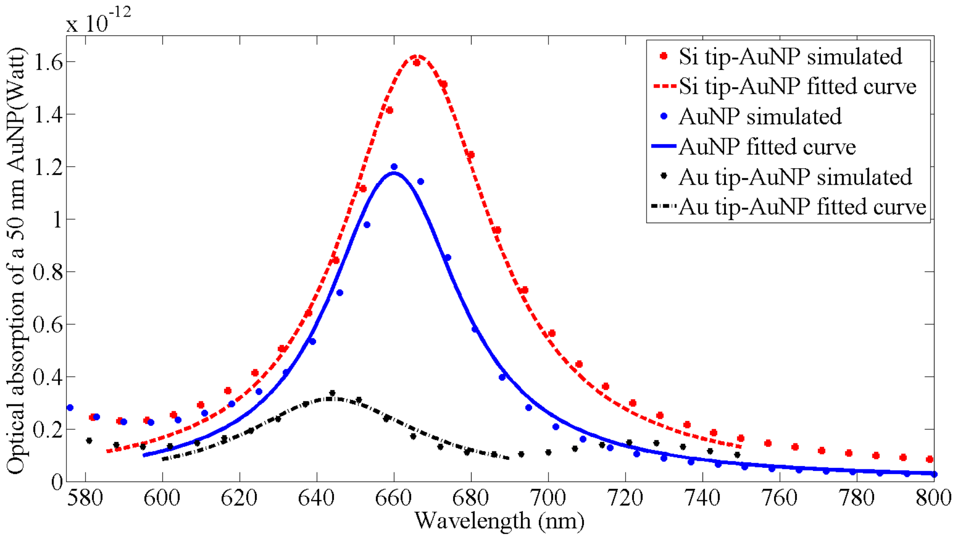

Figure 5.2: Simulated absorption data of a gold nano particle on a gold substrate under different material tips. The Gaussian shaped lines are the fitted plots of the Harmonic Oscillator equation. Compared to "no tip" (blue), a Si tip (red) enhances and the Au tip (black) suppresses the absorption. The dots represent the integrated absorbed power and the lines represent the fitted models, from which the corresponding F_0 and β of (5.1) have been extracted.

As can be seen from Figure 5.2, although a Au tip localizes and enhances the field around the apex, the C_{abs} of a AuNP near the resonant peak gets suppressed. In the following subsections, a similar effect under a totally internally reflected wave on a BK7 glass substrate will be discussed. Later, this absorption modification will be explained in terms of a harmonic oscillator model.

The logarithmic plot in Figure 5.3 shows different absorption cross sections under different illumination conditions. The top right three lines represent the C_{abs} under a surface plasmon polariton. Except for "suspended", the bottom four lines correspond to the glass substrate at a super critical angle illumination (50°). The wavelength ranges are different for each set of data because of the position of the resonant peaks. With regard to the equations described in Section 4.3.3, the incident flux was calculated assuming the maximum field enhancement, as formulated by Weber et al. [99].

Absorption suppression of AuNP under a gold tip of different tip radius

Figure 5.4 shows the absorption suppression of a AuNP under the gold tip at two different wavelengths. Until the tip apex becomes three times as large as the particle, the absorption is cross section is lower than without having any tip. In both cases, the tip apex was 5 nm above the particle surface and the incident angle was 50 degrees from the normal.

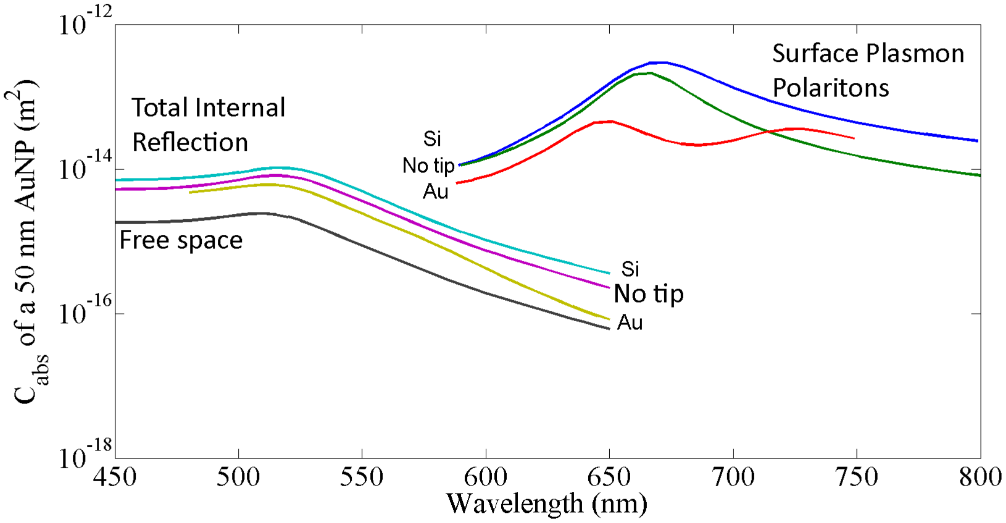

Figure 5.3: Comparison of absorption cross section under a total internally reflected and a surface plasmon polariton wave. SPP wave increases the optical absorption cross section of a AuNP significantly, compared to a TIR illumination. The black line indicates the absorption cross section in free space, and provided for reference.

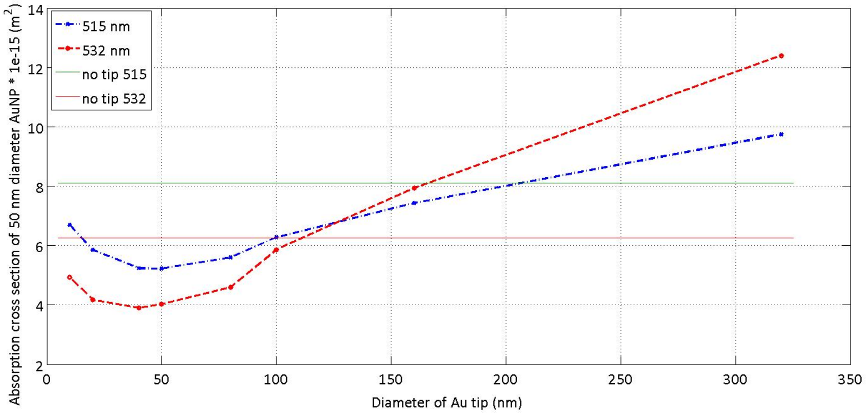

Figure 5.4: Absorption cross-section as a function of gold tip diameter for 515 and 532 nm incident wave. The green and red horizontal lines show the corresponding absorption cross section with a tip being absent. Note the AuNP optical absorption gets suppressed when the Au tip diameter is below 150 nm.

On a glass substrate at super critical angle for both silver and gold nanoparticle

In this Section, the particle absorption modification under metallic and dielectric tip will be studied. Unlike Section 5.1.2, however, although the particle is submerged in evanescent wave, the illumination is caused by the total internal reflection. In Figure 5.5, the individual absorption-scattering of gold - silicon tip and gold nanoparticles are shown. It appears that the power reflected from the tip-particle system increases when a tip is introduced.

In addition, Si and Au tips have very different effects on the absorption of a AuNP. As can be seen from Figure 5.7, a Si tip increases the absorption of the AuNP while a Au tip suppresses it. F_0 and β were extracted from the fitted curves in Figure 5.7, and the changes are shown in Table 5.1. The relative changes in each parameter reveal the origin of the different absorption behaviors. Specifically, C_{abs} strongly depends on F_0, which is strongly influenced by the material of the tip. In both cases, small changes in damping for the AuNP oppose the effect of F_0, but the change in F_0 dominates. Each effect becomes more pronounced as the radius of the tip apex increases. This dependence is plotted in Figure 5.6(a).

Since total internal reflection is used for illumination, the evanescent field at the interface of glass and vacuum is larger than the field of the incident wave in glass. The result of this can be seen in both Figure 5.7 and Figure 5.8, where the blue lines (particle on a substrate without any tip) correspond to almost twice the absorption of the green lines (particle suspended in free space).

In contrast, when a Au or Si tip is introduced above a silver particle, in spite of the field enhancement at the apex of a nanoscale probe, the absorption cross section of a 50 nm AgNP is suppressed in both cases. To better understand this phenomenon, consider two sets of data for the AgNP shown in Figure 5.8: one pair with a substrate (blue-black) and another pair without a substrate (green-red). In both of those cases, when the tip was introduced, the driving force (F_0) was reduced and the damping (β) was increased. When the sharp tip is brought closer to the nanoparticle, scattering from the tip increases the damping, β. Thus, a tip acts as an effective load in this oscillator model. Although present in most of the data, increased damping is particularly visible in Figure 5.8(a), where the introduction of the Si tip clearly broadens the absorption curve.

The driving force F_0, however, is the product of the participating charge (q) and the driving field (E). According to Figure 5.8, either tip reduces the driving force. This can be attributed to

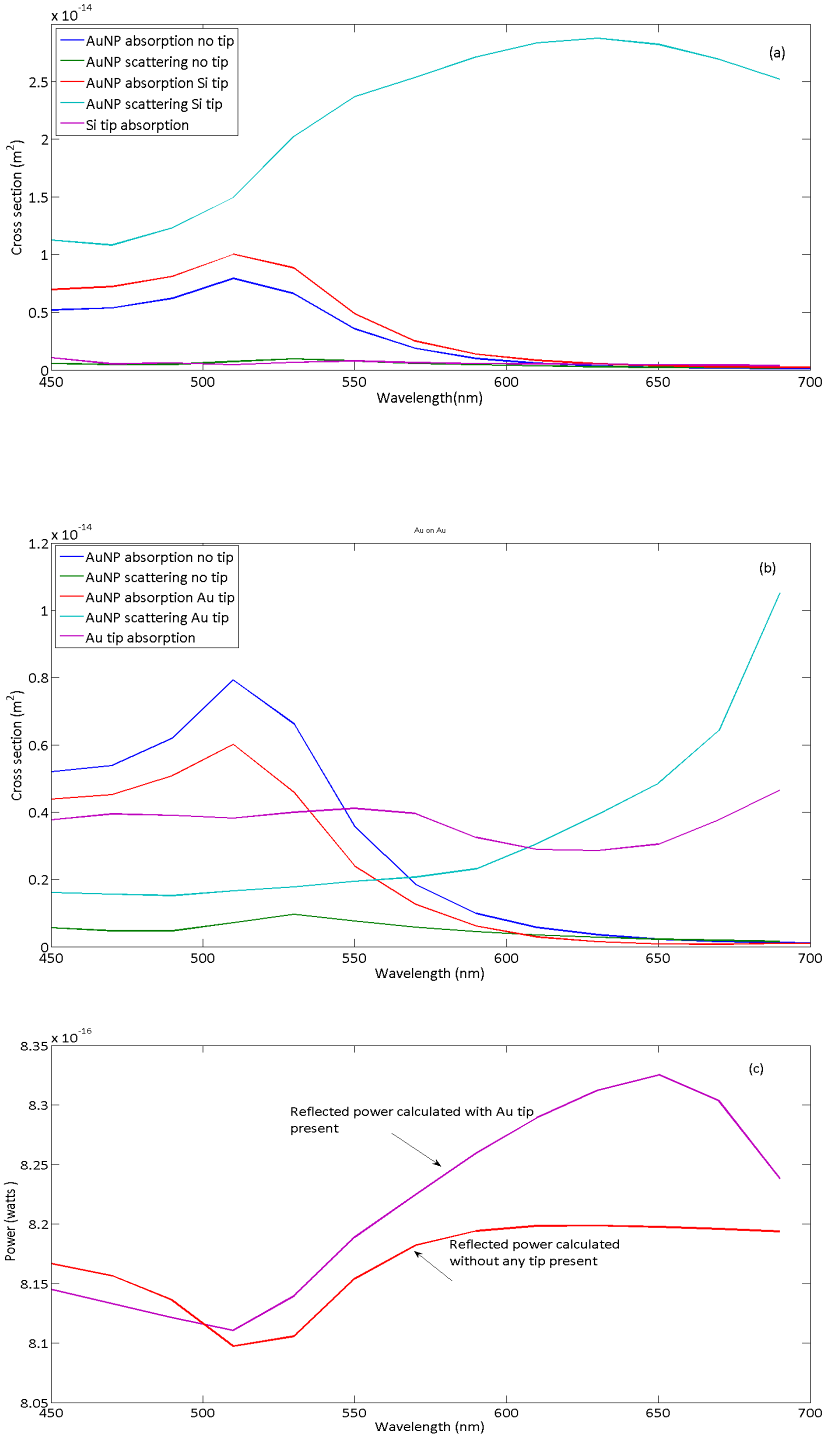

Figure 5.5: (a) Absorption of gold nanoparticle under Si tip in comparison to that of no tip. Si tip enhances the absorption and scattering cross section. The absorption of Si tip is much smaller than that of AuNP. (b) Absorption of AuNP under Au tip. The C_{abs} gets suppressed under gold tip. (c) Reflected power has a dip at the wavelengths where absorption peaks.

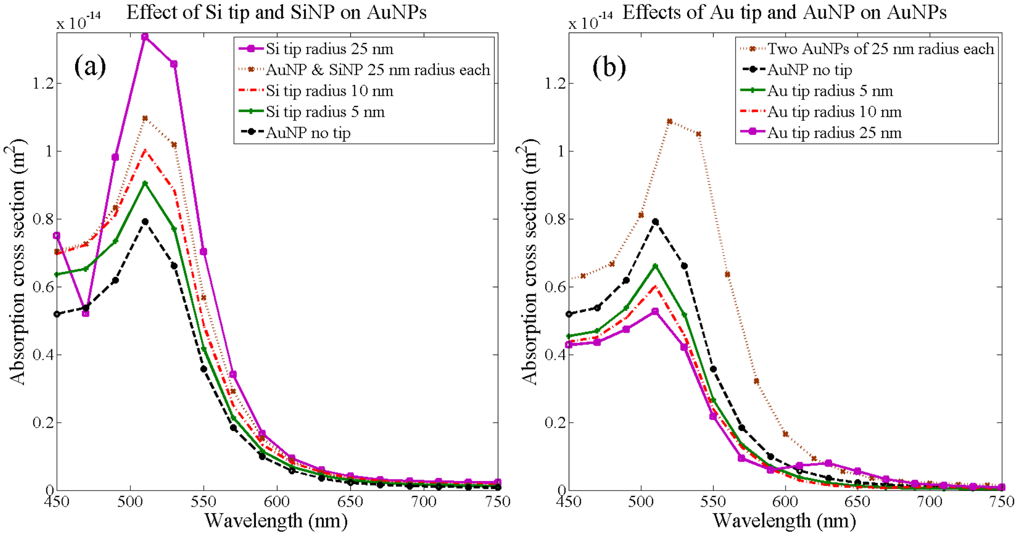

Figure 5.6: Absorption cross section (C_{abs}) of a 50-nm gold nanoparticle (AuNP), sitting on a glass substrate, located below Au and Si tips having 5 (green), 10 (red), and 25 (magenta) - nm radii of curvature. The black dashed line corresponds to the absorption of AuNP, sitting on a glass substrate without any tip. (a) A 25 nm radius Si tip (magenta) enhances the C_{abs} of AuNP more than a 25 nm radius SiNP does (brown). (b) However, a 25 nm AuNP has a drastically different effect on C_{abs} of AuNP than same apex sized Au tip (brown vs. magenta).

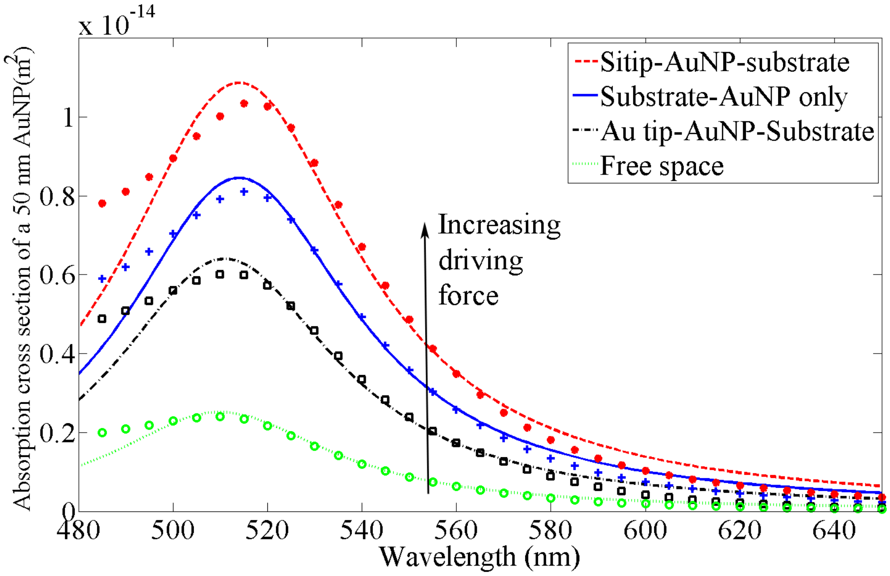

Figure 5.7: Simulated C_{abs} of a AuNP under Si and Au tip along with corresponding fitted curves using HO model. Absorption cross sections were numerically integrated inside the volume of the AuNP. The lines are fitted using (5.1). Curves for the isolated particle and the particle on a substrate without a tip are also shown for reference. A Si tip enhances the C_{abs} of AuNP while a Au tip suppresses it.

either reduced charge participation and/or a reduced driving field. In this model two effects are quantitatively indistinguishable, but either is reasonable when the field is localized near the tip apex. Such as the field throughout the body of the particle could be reduced and/or the charge affected by the localized field could be reduced when compared to an isolated particle.

As with the AuNP, the presence of a substrate enhances absorption when compared to the particle in free space. At first, it might seem surprising that a low dielectric constant substrate enhances absorption while a high dielectric constant tip suppresses it. This is especially true given the suppression of absorption by a uniform change in dielectric constant surrounding a AgNP. However, as mentioned earlier, the enhanced absorption of the particle on a substrate can be attributed to the field enhancement associated with TIR illumination, and the perturbation of the substrate seems to be a secondary factor. However, the silver particle size and separation from tip has not been optimized, and the investigation can not answer what effects that might have.

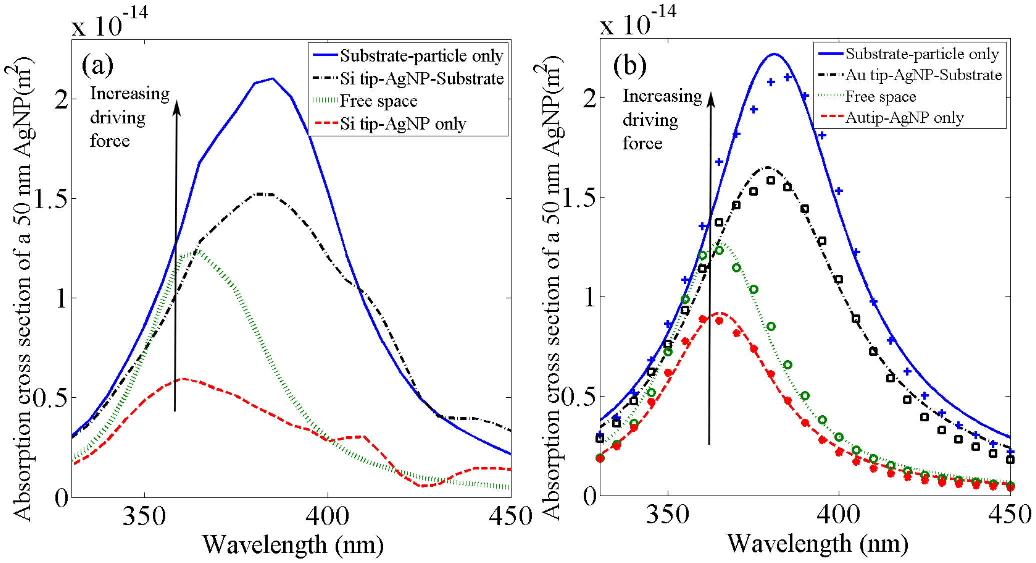

Figure 5.8: C_{abs} of AgNP for different geometric configurations: (a) simulated data points under a silicon tip; and (b) simulated data points under a gold tip and corresponding fitted curves. Whether the particle is suspended in vacuum (green-red curves) or rests on a BK7 glass substrate (blue-black curves), the introduction of a tip reduces the driving force (F_0), and increases the damping (β), resulting in an overall lower absorption.

Again, Table 5.1 summarizes Figures 5.6, 5.7, and 5.8, where one can see that both β and F_0 control the absorption in different cases. For a AgNP under either tip, the driving force is reduced and damping increased such that absorption decreases. For the AuNP, absorption is controlled primarily by F_0, with weak contributions from β, but the two different tips affect F_0 differently.

Therefore, to control the absorption of a nanoparticle, one has to examine the mutual interaction of β and F_0.

5.1.3 Modeling the tip apex with a nanoparticle

Since the illumination is at total internal reflection, the evanescent field is reduced significantly at the end of the truncated tip. Simulating a longer tip does not change the C_{abs} of the nanoparticle more than 5% [86]. Here, the author wishes to consider whether a second sphere could replace the tip apex for the purpose of analysis, which is a common approach used to describe the field modification caused by a tip. For example, while describing near field microscopy by elastic light scattering from a tip, Keilman et al. replaced the probing tip with a point dipole [14]. Chen et al. studied apertureless SNOM numerically using an extended diploe-image dipole for gold nanoparticles on a silicon surface at visible frequencies. To understand the tip interaction, the researchers replaced the tip with a dipole [107]. Similarly, to explain different C_{abs} under different tips, the tip apex is replaced with a particle of the same radius, material, and position. As can be seen in Figure 5.6, a SiNP and a Si tip both enhance the C_{abs} of the AuNP in a qualitatively similar manner. However, unlike the Au tip, a AuNP enhances, rather than suppresses, the C_{abs} of AuNP. Thus, a suspended metal particle is found to act quite differently than a metal tip on the C_{abs} of a AuNP. Therefore, under an evanescent field illumination, and when the particle absorption is of prime concern, a comparable sized particle does not appear to be a good approximation of a tip apex.

5.1.4 Notable assumption and limitation of the proposed simulation method

The finite element solution assumes a truncated tip. Unlike having an infinite tip, a finite tip length may seem to be unphysical. However, since the evanescent field decreases exponentially above the glass substrate, at the end of the truncated side of the tip, the incident field reduces by 23 times that of glass-vacuum interface. Also the domain was made much larger with a truncated tip and the results did not change significantly.

Another possible point of error might have been at the particle-substrate interface, because in the simulation, a point contact has been assumed. This is not ideal since a particle sits on a facet and not on a point, and that interface gives rise to a larger field. However, when the field data were collected, a rectangular fictitious window was chosen, encompassing the upper hemisphere of the nanoparticle and lower part of the tip. Thus, those spurious point contact enhanced fields were avoided.

While (5.1) was fitted with E,q and β, due to the wide variance of values, the software was not automatically able to detect the global error minima; rather, it was successful in determining the local error minima for different starting values of q and β. The author took extensive care while choosing different values of β and q to find the highest R^2 and least sum of squares due to errors, keeping the same upper and lower limits as was listed in Table 4.5. As will be explained in Subsection 5.1.2, the fitting was accurate enough to determine the impacts of individual variables. Also, in the same section, it will be described how changing E and q had the same effect on fitting, because both contribute to the driving force, F_0, as was clarified in (5.1).

5.2 LSPR sensor

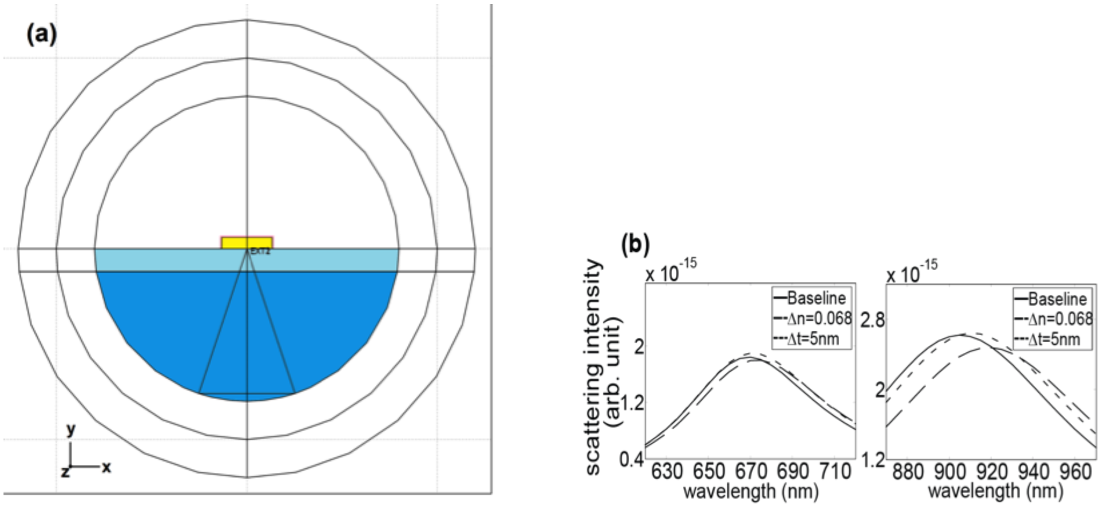

Figure 5.9: (a) Cross section of the simulation domain used for scattering measurements in COMSOL. The incident wave is coming from bottom and the scattered light is collected at the bottom surface of the upside-down cone. The upper hemisphere is water, having a refractive index of 1.33. (b) Calculated transverse (left) and longitudinal (right) resonance of gold nanorod on Indiam Tin Oxide (ITO) coated glass substrate. The shift in wavelength is due to the change in the solution index by 0.068 or due to the absorption of 5 nm thick layer, surrounding the nanorod. Figure courtesy of Neha Nehru.

The developed 3D plasmonics simulation has been used to solve similar problems. Figure 5.9, for example, shows a scattering implementation, where the primary goal is to design a Localized

Surface Plasmon Resonance (LSPR) sensor, which could effectively distinguish between surface binding interactions from interfering bulk effects. As can be seen from Figure 5.9 (b), the collected scattered light from the nanorod depends on the refractive index of the surrounding media and shows distinct peak for different interactions. This may result in a better sensor, and the research intends to continue exploring scattering applications where more modes can be studied to further distinguish even more specific materials or molecules with accuracy.

5.3 Preliminary results for the on chip sensor

In earlier works, it was shown that even a complex plasmonic system, consisting of a tip, a particle, and a substrate, can be expressed in terms of a simple harmonic oscillator (HO) equation. Since the optical absorption of nanoparticles is extensively studied, the driven damped HO model will help explain how the power is being channeled away from the optical waveguide. Here, the intention is to calculate the normalized transmission in term of input and output electric field to evaluate the attenuation caused by the neighboring plasmonic nanostructure:

$$\frac{|\iint E_{\text{in}} E_{\text{out}} dxdy|^2}{\iint |E_{\text{in}}|^2 dxdy \iint |E_{\text{out}}|^2 dxdy}, \tag{5.3}$$

where,

E_{in} = total field calculated at the left side of the waveguide, and

E_{out} = total field calculated at the right side of the waveguide.

Both absorption and scattering from the nanostructure's electron cloud contribute to the damping of the HO model. An attachment of biomolecules to the nanostructure would cause a change in refractive index. This change should affect both the absorption and scattering of the system. Ideally, when the scattered signal off the nanostructure couples destructively into the propagating wave in the waveguide, the power at the end of the optical waveguide would drastically attenuate; ideally, there should not be any signal at all. Therefore, for a perfectly "tuned" condition, a certain molecule should be detected depending on the "attenuated" condition of the waveguide. The goal of the project is to sweep the parameters to achieve this “tuned” condition. This kind of particle sensor provides an advantage, in terms of volume, compared to thin film sensors.

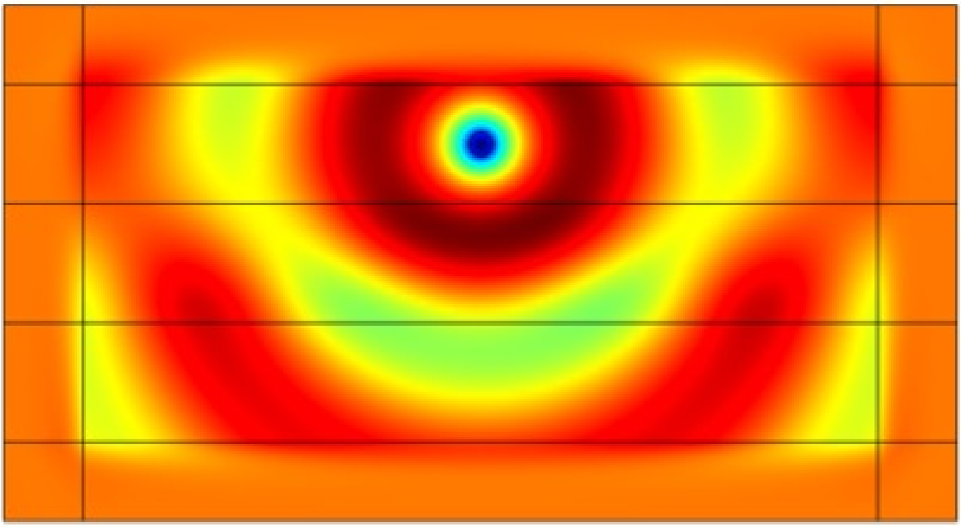

Figure 5.10: The scattered field solution in response to the excitation shown in Figure 4.1. The maximum intensity of the scattered field, caused by the 30 nm diameter gold cylinder (i.e. the circle inside the upper clad layer) is 0.02 V/m.

Figure 5.10 shows the z component of the scattered electric field for the 2D geometry. For this instance, the material properties were selected for a 532 nm wavelength. One can see that the field is stronger below the nano particle. This is because:

- The core below the nano particle is of higher refractive index, and
- The incident field is decaying across the nano particle.

5.3.1 100 nm diameter silver cylinder embedded inside glass cladding above silicon nitride core

Jalal Khan analytically proved in his dissertation that at most 50% of the energy can be transferred to the resonator, 25% can be reflected, and 25% can be transmitted [108]. Using the same geometry as above but replacing the gold cylinder with a silver, the simulations were run in a wider wavelengths rage. In the context of Figure 5.11, the field around the nano structure somewhat resembles a quadruple resonance at the dip close to 500 nm. At the dips around 700 nm, the field around the nano structure looks close to a dipole resonance.

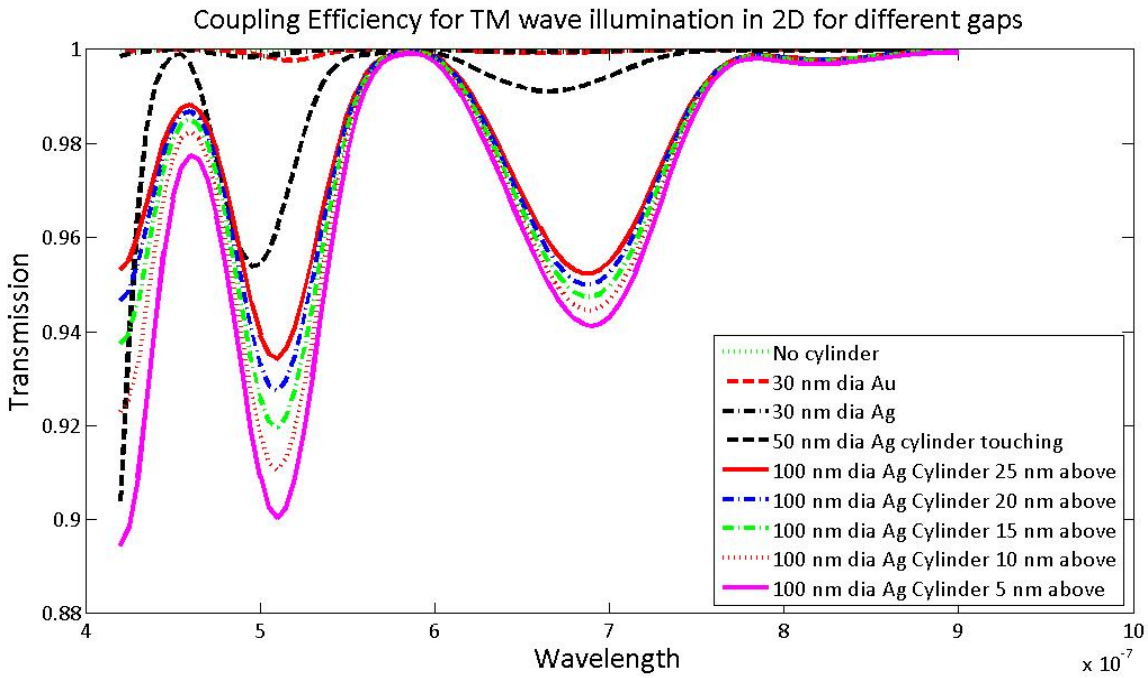

Figure 5.11: Normalized transmission calculated for different vertical gaps between different sized nano structures and silicon nitride core using (5.3).

As one may see from Figure 5.11, the normalized transmission is 1 without any cylinder, because there is no scatterer present, and the input field closely resembles the output field. As the cylindrical nano structure is brought closer to the core, the transmission is reduced more and more. Just to put it in context, a 100 nm diameter silver cylinder in air has a peak at 326 nm wavelength (at 360 nm when embedded inside glass), and no secondary peak between 300 to 1000 nm.

5.3.2 On resonance of different diameter silver cylinders with 5, 10, 15, and 20 nm gaps

Silver was chosen due to its narrower resonance than gold. Similar to Figure 5.11, the minimum gap resulted in the minimum transmission, but the reduction is stronger in Figure 5.12 at resonant wavelength.

Figure 5.13 shows the z component of the scattered magnetic field of a 100 nm diameter silver cylinder above a 100 nm thick silicon nitride core. BK7 glass has been used as the upper and lower cladding in all these waveguide investigations. At a very large wavelength, when the incident wavelength is 7∼8 times larger than the nano structure diameter, the resonance at 700-800 nm wave-

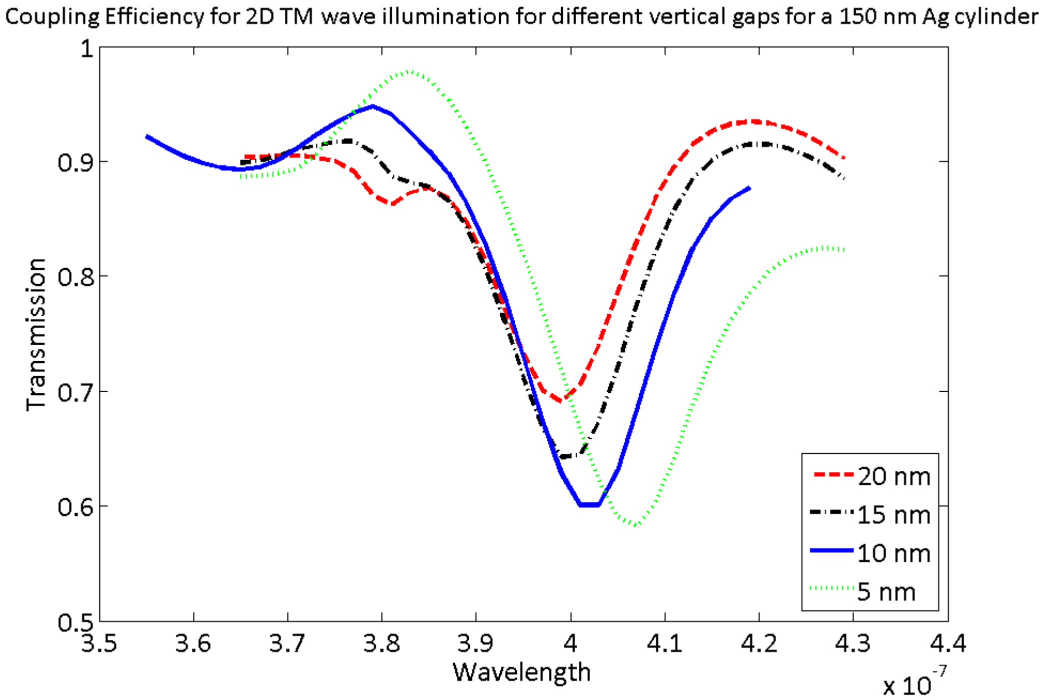

Figure 5.12: The calculated normalized transmission using (5.3) with different gaps between the 150 nm diameter silver cylinder and the silicon nitride core. With reduced gaps, the transmissions are reduced more and more accompanied with red shifts of peaks.

length appears to be a dipole resonance. For the snapshot of scattered fields at other wavelengths, readers may consult the supplemental file of this dissertation.

The transmission reduction is not always monotonous with smaller gaps. As can be seen from Figure 5.14, the minimum transmission is at 10 nm gap and transmission goes back up at 5 nm gap. This is what couple mode theory predicts - that there is an optimum coupling strength between the resonator and waveguide, and that maximum coupling (waveguide to particle) does not necessarily give minimum transmission.

Table 5.3 summarizes the minimum transmissions for different gaps and diameters. As one may expect, a larger nanostructure attenuates more of the incoming wave; hence, the right most column of Table 5.3 is minimum compared to the rest of the columns only with the exception of 20 nm gap.

In the context of Engheta and Watt groups' works mentioned in Section 3.1.2, this effort is more focused on transmission for sensing purpose, and not on nanoantenna radiation. The author, however, intends to continue this waveguide investigation to find the optimum combination of gap and structure to minimize the transmission.

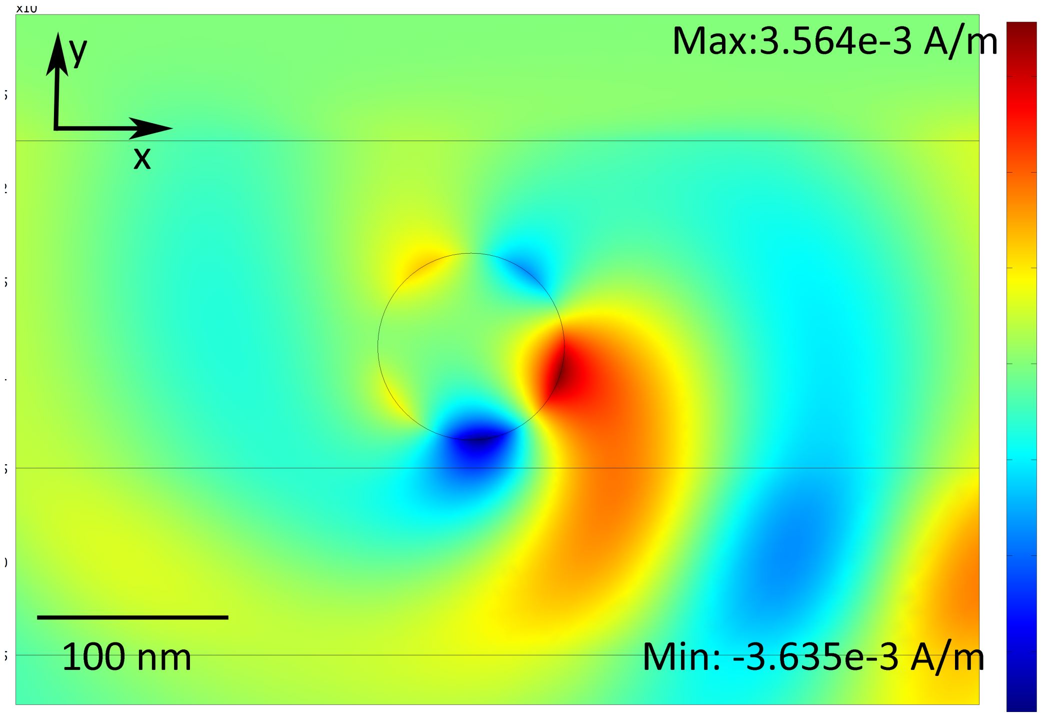

Figure 5.13: The scattered magnetic field's z component of a 100 nm diameter silver cylinder. This snapshot corresponds to the minimum transmission where it somewhat looks like consisting of three maximas and three minimas. Note the strong scattered field along the direction of actual propagation (i.e. left to right), and the incident field is 1/377 A/m. The readers are requested to consult the supplement file for a movie of this simulation.

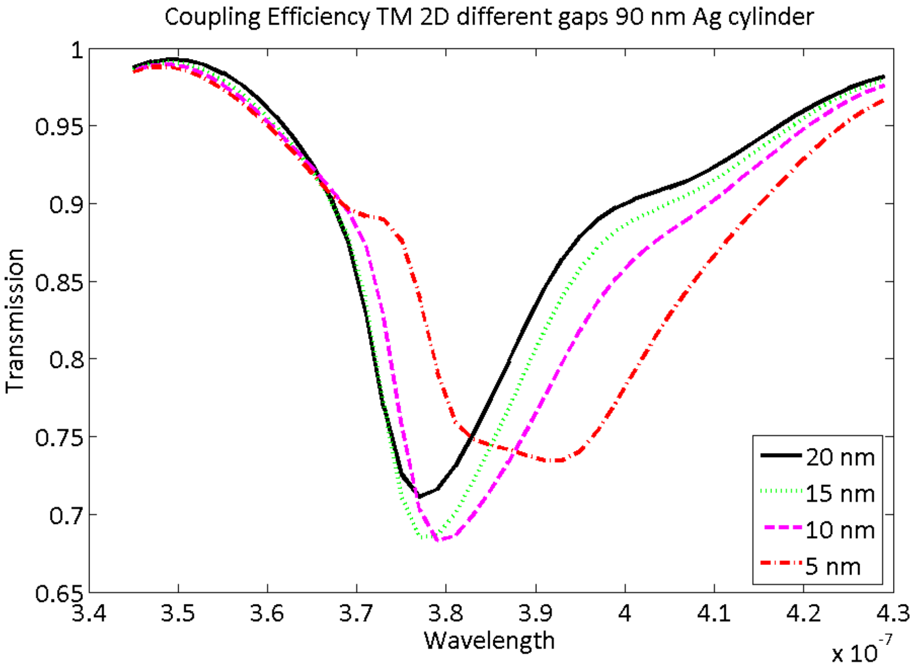

Figure 5.14: The calculated transmission using (5.3) with different gaps between the 90 nm diameter silver cylinder and the silicon nitride core. Unlike Figure 5.12, the minimum transmission does not correspond to the minimum gap between the waveguide core and the nano structure.

Table 5.3: Comparison of minimum transmissions for different combinations of silver cylinder diameters and vertical gaps. Although the minimum transmission corresponds to the minimum gap, the 100 nm diameter silver cylinder has a minima at 15 nm, which is smaller than those of 10 and 5 nm gaps.

Ag Cylinder diameter Gap	10 nm	50 nm	100 nm	150 nm
5 nm	0.99	0.82	0.76	0.58
10 nm	0.99	0.84	0.66	0.60
15 nm	0.99	0.85	0.66	0.64
20 nm	0.99	0.86	0.68	0.69

Chapter 6

Conclusions and Future Work

6.1 Conclusions

The effects of metallic and dielectric tips on the absorption of silver and gold nanoparticles on a glass-substrate (gold superstrate for SPP) are simulated in this research. Increasing the permittivity of the surrounding media directly impacts the optical absorption of nanoparticles. With respect to the formulation of the absorption cross section, when a substrate is introduced under the particle or a dielectric tip is brought closer to the nanoparticle, C_{abs} of a AuNP increases. However, the absorption modification of AgNP can not be explained this way, and the author used the harmonic oscillator equation to model the absorbed power inside the nanoparticles. The advantage of harmonic oscillator model is that it further helps to explain the numerical results in terms of physical phenomena. the absorption under metallic tips for both AuNP and AgNP. Although a Au tip enhances the field near both the particles, the particle absorption is suppressed. The use of a harmonic oscillator model allows one to see that the probe works as a damping load by increasing the scattering. However, for a Si tip the absorption is enhanced for a AuNP, but is suppressed for a AgNP. In this case the tips' effects are qualitatively similar to a change in the refractive index of the entire dielectric environment or to the introduction of a second sphere. Given the optical properties of silver and gold in this wavelength range, one would expect the observed behavior from a simple dielectric perturbation. However, the harmonic oscillator model further reveals that the silicon tip increases damping in both cases, but changes the driving force in such a way that absorption is increased in one case and suppressed in the other. In all cases, the relative changes in the driving force and damping of the oscillator affect the absorption of the particle-tip systems differently. This work emphasizes that optical absorption in nanoscale structures behaves differently from scattering and electric field enhancement, and harmonic oscillator models provide insight into the relevant competing physical mechanisms.

6.2 Future Work

Although the author does not have a quantifiable result to comment on the improvement of the waveguide sensor performance, the proposed device should alleviate the requirement of spectrometer, which is often the largest component of integrated optical devices. The accomplishment of this research should make the device small, portable, and reliable. Unlike the traditional concept of analyzing the scattered signal, one can just look into the output light of the waveguide to decide the existence of a specific molecule in the sample. For example, this sensor should be applicable to control pesticide residue, reduce analysis cost, and be less time consuming. Thus, the device should help alleviate food contamination, along with the existing applicability for sensing purposes in lab.

To prove this hypothesis, in the context of Figure 5.10 one needs to know in what conditions the scattered light off the nanostructure would couple with the propagating wave inside the waveguide destructively. The possible parameters include:

- Shape of the structure: spherical, cylindrical, or rod shape.
- Material of the metallic nanostructure: gold or silver.
- Material combination of the waveguide: the selection of core and clad to facilitate single mode propagation.
- Dimension of the waveguide: allowing single mode propagation.
- Size of the nanostructure: for example, the optimum radius of the sphere or lengths of the longitudinal and transverse axes.
- Distance of the nanostructure: how close the structure should be to the core inside the clad, to understand how much overlapping of the evanescent field is necessary for an efficient destructive coupling.

- Wavelength of excitation: largely depending on the size, shape and material of the selected structure, because the change in refractive index would cause the resonance peak to shift.

After a comprehensive numerical investigation, it should be clearer under which geometric combinations the destructive light coupling inside the waveguide would be possible. One can use the equation of driven damped harmonic oscillator model to explain both the absorption and scattering off the nanostructure. More specifically, the HO model would help understand how the optical absorption and scattering contribute to the damping of the electron cloud oscillation inside the metallic nanostructure. With the help of simulations, the author can correlate the damping quantity with the portion of the scattering that couples back into the waveguide that would be out of phase with the propagating wave inside the waveguide.

Chapter 7

Appendix

A.1 Conditions and properties of SPP

As was briefly mentioned in Section 2.5.5, for a surface mode to exist at the interface of two media, having the permittivities of $\varepsilon_1(\omega)$ and $\varepsilon_2(\omega)$, the following two conditions have to be met:

$$\varepsilon_1(\omega).\varepsilon_2(\omega) < 0, \text{and} \tag{A.1.1}$$

$$\varepsilon_1(\omega) + \varepsilon_2(\omega) < 0; \tag{A.1.2}$$

meaning that one of the dielectric functions must be negative and the absolute value of the dielectric function must be greater than the other. Therefore, specific noble metals such as silver and gold, who have a larger negative real part of the dielectric function and a small imaginary part, can excite a surface plasmon polaritons having interfaces with glass or vacuum. (A.1.1) and (A.1.2) were derived by solving the Maxwell's equations and imposing the boundary conditions. The dispersion relation along the direction of propagation is

$$k_{\mathrm{x}}^2 = \frac{\varepsilon_1 \varepsilon_2}{\varepsilon_1 + \varepsilon_2} k^2, \tag{A.1.3}$$

where,

k_x = the wave vector of the SPP along the direction of propagation, x in this case, and

k = the wave vector of free space.

From (A.1.3), one can see that the free space wave vector can not be equal to the k_x at any frequencies, meaning the SPP can not be excited by a light wave at an interface directly. Instead, one has to excite an evanescent wave to provide the additional momentum for the SPP, as is shown in Figure A.1.1 [3].

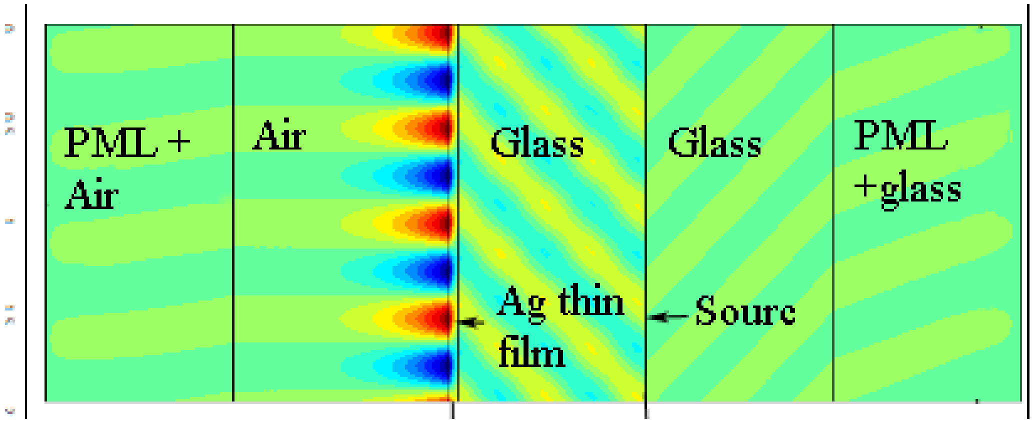

Figure A.1.1: Simulation of SPP at a Ag-air interface. The entire geometry is 5 μm long and 1 μm wide. The port boundary is emitting 1 watt TM polarized wave towards the Ag film. As is shown in figure A.1.2, at 43.9° angle of incidence, the energy is transformed into surface plasmon polaritons and trapped in a much smaller scale than the incident 532 nm wavelength. Port boundary launches the wave and lets the reflected wave go through uninterrupted.

Figure A.1.1 is a 2D contour plot of the z component of the magnetic field of Surface Plasmon Polaritons (SPP). The SPP is excited at the interface of silver and vacuum. The boundary conditions of the sides were Floquet periodic. There is a discontinuity between the glass-glass horizontal interface where on one side a 532 nm TM polarized wave was launched at an angle of 43.9° from the normal. Despite the discontinuity, the reflected wave from the Ag film propagated across that boundary unimpeded and was absorbed in PML. Note the high amplitude of the SPP field for a 1 watt incident field and its confinement is smaller than the incident wavelength. In Figure A.1.2, the reflectivity drops down sharply at the angle, where the SPP is strongly excited. One interpretation is that the missing energy is converted into surface plasmon waves at the interface at that angle of incidence. Another interpretation is that the reflected light destructively interferes with the SPP emitted light [3].

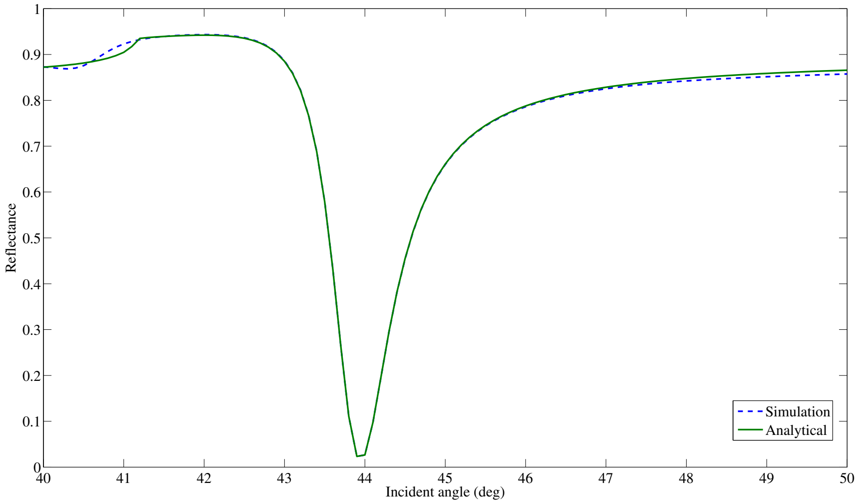

Figure A.1.2: Reflectivity curve with respect to the incident angle.

Mathematically, the glass prism serves the momentum mismatch needed to excite the surface mode. With regard to the charge oscillation mechanism, the SPP can be described as the field being perfectly aligned with the thin metallic layer. If the wave directly impinges on the layer, the buildup charge would meet the next wave peak destructively, and no SPP would excite. However, one can excite the surface mode by launching a perfectly aligned TM polarized wave in a perfectly polished metallic layer. This process is significantly more difficult than a prism coupling, where for a specific angle the alignment matches vertically with the metallic layer. Thus, one can make sure that the built-up charges meet the subsequent wave peak constructively to result in an excited SPP mode.

A.2 Comparison between SPR and LSPR sensors from application point of view

As was described in Sections 2.5.3 and 2.5.5, by principle a tiny modification of the refractive index of the surrounding media close to a propagating or localized surface plasmon can be detected at the scattering and/or extinction spectra. This phenomena is being widely used to detect analyte binding at or near a metal surface, such as a broad range of analyte-surface binding interaction including the adsorption of molecules and protein, DNA-RNA hybridization, antibody-antigen binding, and

DNA-protein interactions. SPR sensors have been used for about two decades now, but LSPR sensors have the potential to be widely used for specific applications [109]. The relationship of LSPR and SPR sensors is compiled in Table A.2.1.

Table A.2.1: Comparison of SPR and LSPR sensors. Table reproduced with the permission from Springer [109].

Feature/characteristic	SPR	LSPR
Label-free detection	Yes	Yes
Distance dependence	$\approx$ 1000 nm	$\approx$ 30 nm (size tunable)
Refractive index sensitivity	2×10^6 nm RIU^{-1}	2×10^2 nm RIU^{-1}
Modes	Angle shift, wavelength shift, imaging	Extinction, scattering, imaging
Temperature control	Yes	No
Chemical identification	SPR-Raman	LSPR-SERS
Field portability	No	Yes
Commercially available	Yes	No
Cost	USD 150000 $\sim$ 300000	USD 5000 for multiple particles, 50000 for single nanoparticle
Spatial resolution	$\approx 10 \times 10 \mu$m	One nanoparticle
Nonspecific binding	Minimal (determined by surface chemistry and rinsing)	Minimal (determined by surface chemistry and rinsing)
Real-time detection	Time scale $= 10^{-1} \sim 10^3$ s, planar diffusion	Time scale $= 10^{-1} \sim 10^3$ s, radial diffusion
Multiplexed capabilities	Yes	Yes-possible
Small molecule sensitivity	Good	Better
Microfluidics compatibility	Yes	Possible

However, both sensors response can be described by

$$\Delta\lambda_{\mathrm{max}} = m\Delta n(1 - \exp^{-\dfrac{2d}{l_{\mathrm{d}}}}), \tag{A.2.1}$$

where,

$\Delta\lambda_{\mathrm{max}}$ = the wavelength shift response,

Δn = change in refractive index induced by an adsorbate,

d = the effective adsorbate layer thickness, and

l_{d} = the characteristic electromagnetic field decay length.

A.3 Mie calculations

Mie theory allows one to calculate the scattering coefficients of a non magnetic spherical particle embedded in a homogenous media. The idea is to add the scattered field to the incident field to get the total field. For example,

$$E_{\mathrm{i}} + E_{\mathrm{s}} = E_1, \qquad H_{\mathrm{i}} + H_{\mathrm{s}} = H_1. \tag{A.3.1}$$

Where,

'i' suffix means incident and 's' means scattering.

The $\mathrm{a_n}$ and $\mathrm{b_n}$ of (A.3.2) and (A.3.3) below are referred to as the Mie coefficients which determine the relative amplitudes of the vector spherical harmonics when excited by a specific wavelength:

$$a_{\mathrm{n}} = \frac{\bar{n}^2 j_{\mathrm{n}}(\bar{n}x)[xj_{\mathrm{n}}(x)]' - \bar{\mu} j_{\mathrm{n}}(x)[\bar{n}xj_{\mathrm{n}}(\bar{n}x)]'}{\bar{n}^2 j_{\mathrm{n}}(\bar{n}x)[xh_{\mathrm{n}}^{(1)}(x)]' - \bar{\mu} h_{\mathrm{n}}^{(1)}(x)[\bar{n}xj_{\mathrm{n}}(\bar{n}x)]'} \tag{A.3.2}$$

$$b_{\mathrm{n}} = \frac{\bar{\mu} j_{\mathrm{n}}(\bar{n}x)[xj_{\mathrm{n}}(x)]' - j_{\mathrm{n}}(x)[\bar{n}xj_{\mathrm{n}}(\bar{n}x)]'}{\bar{\mu} j_{\mathrm{n}}(\bar{n}x)[xh_{\mathrm{n}}^{(1)}(x)]' - h_{\mathrm{n}}^{(1)}(x)[\bar{n}xj_{\mathrm{n}}(\bar{n}x)]'} \tag{A.3.3}$$

where,

$a =$ radius of the sphere,

$\lambda =$ the wavelength in vacuum,

$j_{\mathrm{n}} =$ the spherical Bessel function of order n,

$h_{\mathrm{n}} =$ the spherical Hankel function of order n,

the relative refractive index, $\bar{n} = n_1/n_2$, where

$n_1 =$ complex refractive index of the particle,

$n_2 =$ refractive index of the surrounding media,

the relative permeability, $\bar{\mu} = \mu_1/\mu_2$, where

$\mu_1 =$ complex relative magnetic permeability of the particle,

$\mu_2 =$ complex relative magnetic permeability of the surrounding media, and

the size parameter, $x = 2\pi n_2 a/\lambda$.

The primed terms indicate differentiation of the functions with respect to their arguments. Thus a_{n} and b_{n} include the particle size, permittivity, and permeability [49]. Since a_{n} and b_{n} tend to zero as $\bar{n}$ approaches unity, it follows that the scattered field tends to be zero if there were no particle present.

With regard to the definition described in Section 2.9.1, one can calculate the extinction cross section,

$$P_{\mathrm{ext}} = \frac{W_{\mathrm{ext}}}{I_{\mathrm{i}}} = \frac{2\pi}{k^2} \sum_{\mathrm{n}=1}^{\infty} (2n+1) Re(a_{\mathrm{n}} + b_{\mathrm{n}}) \tag{A.3.4}$$

where,

$W_{\mathrm{ext}} = \frac{1}{2} \,\mathrm{Re} \int_0^{2\pi} \int_0^{\pi} (E_{\mathrm{i}\phi} H^*_{\mathrm{s}\theta} - E_{\mathrm{i}\theta} H^*_{\mathrm{s}\phi} + E_{\mathrm{s}\phi} H^*_{\mathrm{i}\theta}) r^2 \sin\theta \, \delta\theta \, \delta\phi.$

With regard to the description in Section 2.9.3, the scattering cross section is,

$$P_{\mathrm{s}} = \frac{W_{\mathrm{s}}}{I_{\mathrm{i}}} = \frac{2\pi}{k^2} \sum_{\mathrm{n}=1}^{\infty} (2n+1)(|a_{\mathrm{n}}|^2 + |b_{\mathrm{n}}|^2) \tag{A.3.5}$$

where,

$W_{\mathrm{s}} = \frac{1}{2} \,\mathrm{Re} \int_0^{2\pi} \int_0^{\pi} (E_{\mathrm{s}\theta} H^*_{\mathrm{s}\phi} - E_{\mathrm{s}\phi} H^*_{\mathrm{s}\theta}) r^2 \sin\theta \, \delta\theta \, \delta\phi.$

Furthermore, the absorption cross section can be calculated by subtracting (A.3.5) from (A.3.4). As was explained in Figure 2.7, the scattering off of a particle depends on the size *a*, relative permittivity ϵ_{r} and hence, the refractive index *n*, as is shown in (A.3.2) and (A.3.3) [36]. In this dissertation, the Mie code was used from ScattPort.org [110].

A.4 Fundamentals of different computational EM methods

A.4.1 FEM

Finite Element Method solves the scattered field problem in frequency by discretizing the Helmholtz wave equations:

$$\bigtriangledown^2 E + k^2 E = 0 \tag{A.4.1}$$

$$\bigtriangledown^2 H + k^2 H = 0 \tag{A.4.2}$$

where,

$$k^2(r) = \omega^2\varepsilon(r)\mu(r)/c^2. \tag{A.4.3}$$

The material property is incorporated by (A.4.3). The general idea is to solve the Helmholtz equations in free space such that the fields satisfy the boundary conditions:

- The tangential field components are continuous across the surface of the particle and

- The fields decays into the far field no slower than $1/r$ for large r.

The entire sub-domain is discretized in a smaller mesh domain, often with a tetrahedral shape. The E and H fields are approximated in each element by a local function. In the simulations of this dissertation, only the scattered electric field was computed and superimposed on the source field to evaluate the total field. Although it is hard to accommodate a spherical surface with tetrahedral shaped elements, one can achieve enough accuracy with sufficiently small size. Often times, more elements are inserted where there are larger field gradients. For example, at and near the sharp nanoscale probe, in between the tip and particle, and nearby regions the elements are denser, as was shown in Figure 4.7.

In FEM, the analysis takes place in an unbounded media. Since conducting numerical simulation in infinite region is unrealistic, the computation domain needs to be limited in size, while large enough, to accommodate the structure of interest. To restrict the computation into a finite time, the domain needs to be truncated by a specialized boundary condition, which absorbs the impinging wave without producing reflection; so that, the reflected wave off the computational boundary can not contaminate the results [49]. To achieve this goal, an artificial sub domain called perfectly matched layer (PML) is used. The major characteristics of PML are:

- It is a lossy medium, matched with the adjacent medium, to reduce any reflection from the interface.

- Both the propagating and evanescent wave should attenuate rapidly inside the medium, regardless of the angle, frequency, and polarization. [31]

At the outer side of PML, the scattering boundary condition is utilized to avoid the unwanted reflections, as was described in Section 4.2. This Scattering Boundary Condition is simply an absorbing boundary condition to absorb the remaining unwanted reflection at the end of PML. PMLs, as the name suggests, were defined with the same properties as the adjacent media to absorb most of the incident wave. In this dissertation, PMLs are mostly absorbing in the radial direction, due to spherical geometries. PML provides good performance in a wide range of incident angles and is not particularly sensitive to the shape of the wavefront [59, 94].

A.4.2 Discrete dipole approximation (DDA)

The generic concept of DDA is that each particle is visualized as an assembly of finite array of cubic elements so that, the field can be calculated by evaluating the interaction with the incident field and the neighboring induced fields [49]. The DDA approach essentially treats the arbitrarily-shaped scatterer(s) as being composed of Rayleigh scatterers, i.e, polarizable dipoles stacked in a lattice formation, which usually is cubic. The dipoles not only react to the excitation from the incident field but also to the re-radiation from the other dipoles. DDA assumes the steady state condition and calculation are performed for one wavelength at a time [64].

A.4.3 Null-field method with discrete sources (NFM-DS)

With regard to the description in Section 2.10.1, in the NFM-DS, the internal field is calculated using the expansion of multiple discrete sources. This allows for the computation of the T-matrix for particles with high aspect ratios. Furthermore, the NFM-DS is not restricted to axisymmetric scatterers and also allows for particle-surface light scattering. With this method, the exact solution for a particle positioned on or in the vicinity a planar substrate can be attained [111].

A.5 Time required to melt a nanostructure: theoretical calculation

With regard to the description in Section A.6.1, the tightest beam size is 4 μm in diameter, and the power of that beam is 26 mW.

Therefore the beam intensity, $\dfrac{26 \times 10^{-3}}{\pi(2 \times 10^{-6})^2} = 2.07 \times 10^9\ \mathrm{W/m^2}$.

According to Jain et al. the absorption cross section of a 40 nm diameter gold nanoparticle is $2.93 \times 10^{-15}\ \mathrm{m^2}$ at 528 nm wavelength of illumination [112].

Therefore, the power absorption by a 40 nm diameter AuNP is $2.07 \times 10^9 \times 2.93 \times 10^{-15} =$

6.06×10^{-6} W;

volume of a 40 nm AuNP is $\dfrac{4}{3}\pi(20 \times 10^{-9})^3\,\mathrm{m}^3$;

and the density of gold is 19.3 $\times 10^3$ $\mathrm{Kg/m^3}$.

Hence, mass of a 40 nm AuNP is $3.35 \times 10^{-23} \times 19.3 \times 10^3 = 6.47 \times 10^{-19}$ Kg.

According to engineeringtoolbox.com, the specific heat of gold is 0.13 KJ/Kg.K.

Which implies, heat required to completely melt a 40 nm AuNP is $0.13 \times 6.47 \times 10^{-19} = 8.41 \times 10^{-20}$ KJ.

Therefore, the time required to completely melt the sphere is $\dfrac{8.41 \times 10^{-17}}{6.06 \times 10^{-6}} = 1.39 \times 10^{-11}$ s.

As was shown in Figure 2.12, the experimental procedure also took the time on the order of picoseconds.

Similarly, the calculation is repeated for a nanorod with an effective radius of 21.86 nm and an aspect ratio of 3.9 at 842 nm. The reported absorption cross section is 1.97 $\times 10^{-14}\,\mathrm{m}^2$ [112].

Therefore with regard to the power intensity of the laser, the energy absorbed by the nanorod is 2.07 $\times 10^9 \times 1.97 \times 10^{-14} = 4.08 \times 10^{-5}$ J

Considering the rod as a perfect cylinder, the volume is $\pi \times (21.86 \times 10^{-9})^2 \times 85.25 = 1.28 \times 10^{-22}\mathrm{m}^2$.

Given the density of gold, the mass of this rod would be $1.28\times10^{-22} \times 19.3 \times 10^3 = 2.47 \times 10^{-18}\,\mathrm{Kg}$

The required heat to melt the rod is 3.21×10^{-19} KJ.

Hence the time required to completely melt the rod is $\dfrac{3.21 \times 10^{-16}}{4.08 \times 10^{-5}} = 7.88$ picosecond.

A.6 Experimental setup

A.6.1 Laser

A continuous wave solid-state green laser of 532 nm wavelength was used. This diode-pumped single mode laser uses a Fabry-Perot cavity. Its output power is 530 mW and generates a linearly polarized light, as was found in cnilaser.com. The laser uses a thermoelectric cooling mechanism.

A.6.2 Sample

The sample is a a known pattern, made on the indiam tin oxide (ITO) coated glass substrate. The pattern was created using electron beam lithography. The parameters are listed in Table A.6.1. The dwell times were automatically calculated by the software.

Table A.6.1: EBL parameters, used to create the drawn pattern on ITO layered glass substrate.

Beam energy	30 kV
Aperture	20 μm
Working Distance	7 mm
Beam Current	177.11 pA
Area Dose	300 μC/cm^2
Line Dose	900 pC/cm
Area dwell time	0.000271 ms
Line dwell time	0.002033 ms

After the patterning was successful, the sample was washed in a PMMA developer, methyle isobutyle ketone. After about 60 seconds, the sample was washed in isopropanol to stop the solution process. With the help of a thermal evaporator, the gold rods were deposited on the sample. A gold pellet was heated resistively while the sample was held upside down above it; whereas the sample was held upside down by a clip where the gold was deposited in a controlled way.

The sample was attached to the holder firmly with screws during laser illumination. Under the AFM stage, three poles with magnets attached to their ends hold the sample tightly. To achieve the sample's proper position, the poles' vertical movement were controlled. The AFM camera was used to focus the laser beam (where the spot size was smallest), and external camera was used to make sure that the sample is at same distance.

A.6.3 Optical path

As can be seen from the optical diagram, the laser was followed by a half wave plate and polarizer. This arrangement was made to control the power. The filter was used to cut off the optical path, whenever necessary. The half wave plate, as it changes the direction of polarization, rotates the linearly polarized beam to let the desired power flow through the polarizer. If the half wave plate is rotated by θ, the polarization will rotate 2θ. The unused power was directed outward and safe-

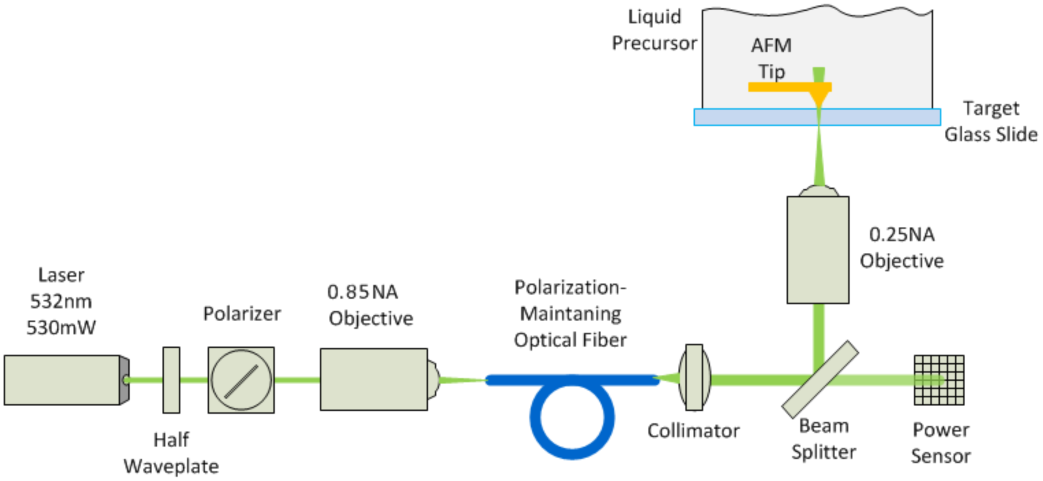

Figure A.6.1: Optical diagram of the laser system of the project: Nanorod melting. Figure Courtesy: Carlos A. Jarro.

guarded from the user. The assembly was necessary because the power was too high for an absorber filter, and the optical fiber used can sustain only up to 300 mW.

The 20x objective focuses the beam such that most of the power fits inside a polarization maintaining optical fiber (OF) core. This refractive objective was coupled with the OF with an efficiency around 30%, because the core of the optical fiber was only 3μm and the beam needed to be aligned either with the fast or slow axis of the OF. A single mode fiber cleans the beam so that it behaves more like a pure Gaussian beam. The collimator was connected to a hollow tube, which was held by a three-axis stage to have better control in all three axes for proper alignment with the AFM. A beam splitter, which nominally transmits 30% of the beam and reflects 70%, was placed following the collimator.

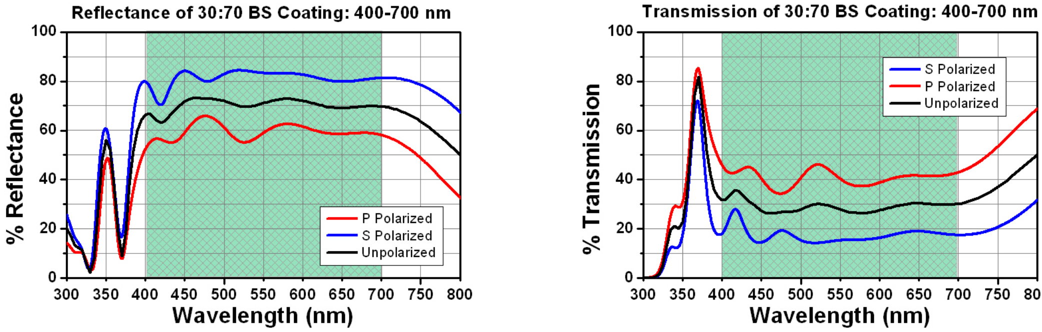

Figure A.6.2: (a) Reflectance and (b) transmittance of the beam splitter, used in the setup. Since the operating wavelength was 532 nm, the transmission was 15% for S-polarization. Figures from Thorlabs.com.

However, polarization needed to be vertical with respect to the beam splitter. For the P polarization there would be a component parallel to the beam splitter axis. With any other polarization except S, more light will pass through. With regard to the blue line of Figure A.6.2 (b), the 15% light was measured through a photovoltaic power sensor. Following the splitter, a 10x objective was placed. The sample was not precisely at the focal point, and the working power at the sample was around 20∼27 mW.

A.7 Results of nanorod deformation under CW laser

With regard to the experimental setup, described in Section A.6.2, an array of nanorods was patterned on an ITO-glass substrate. As can be seen from Figure 7.1(a), the rods were arranged in such a way that one set of rods may use the strong localized fields at the ends of other rods. The primary goal was to achieve structural deformation at the places where the field enhancement was strongest. However, Figure 7.1(b) suggests that the attempt of deformation was not successful. The reason might be the rate of heat absorption under a CW laser is insufficient to deform permanently. The experimental setup did not have enough provision and resource to accommodate a pulse laser, which might be able to melt the rods.

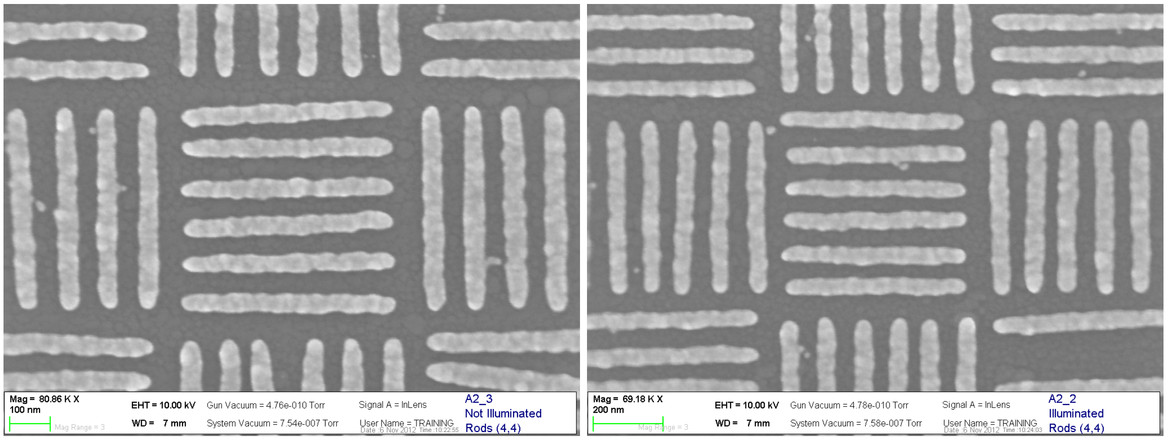

Figure A.7.1: (left) The nanorod structure before the laser illumination. (right) The nanorod structure after laser illumination. The CW laser illumination did not make any structural deformation.

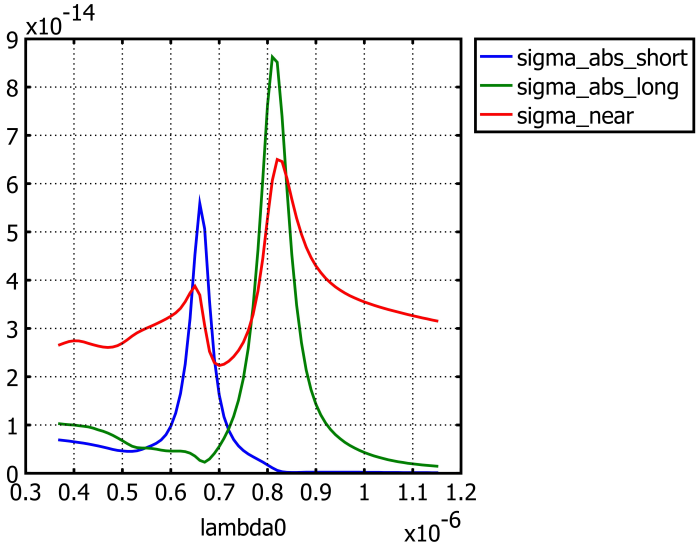

Figure A.8.1: Cross sections of two unequal dimers on a glass substrate. Dimensions for longer rod: height 20 nm, width 58 nm, and length 136 nm. Dimensions for shorter rod: height 20nm, width 50 nm, and length 85 nm. The gap between the rods is 30 nm. The polarization of the incident wave is TE (i.e. electric filed is aligned with the longitudinal axes). The red line shows the scattering cross section of the entire structure. Comparing the blue and green lines, the longer rod should absorb significantly more than the shorter rod close to 1 μm wavelength. The opposite combination can be achieved at around 665 nm.

A.8 Results of plane wave illumination on unequal dimers

The motivation of having two unequal rods on a substrate was that one rod should absorb more than the other at a given wavelength. Therefore, if the illumination wavelength was chosen such that it coincides with the absorption resonance peak of a specific rod, that rod should absorb significantly higher power than the other. Thus one may have a local heat source, and the unheated structure works as a heat sink. This structure should allow a way to understand the heat transportation between the two nanorods.

Figure A.8.1 shows preliminary results of two rods having 136 nm and 85 nm lengths, and sitting on a BK7 glass substrate. Near the resonance peak of the longer rod, the absorption cross section is almost eight times higher than that of the shorter rod. At this wavelength, the longer rod should get heated and transfer heat to its neighboring unheated shorter rod. Varying the gap between the two rods, one can comment on the comparative contributions of conduction and radiation in nanoscale heat transfer.

References

[1] G. E. Moore, “Cramming more components onto integrated circuits,” *Electronics*, vol. 38, no. 8, April 1965.

[2] M. Kaku, *Physics of the Future: How Science Will Change Daily Life by 2100*. Knopf Doubleday Publishing Group, 2011. [Online]. Available: http://books.google.com/books?id=lGS9Lbv0PdsC

[3] L. Novotny and B. Hecht, *Principles of Nano-Optics*. Cambridge University Press, 2008.

[4] M. Mansuripur, A. R. Zakharian, A. Lesuffleur, S.-H. Oh, R. J. Jones, N. C. Lindquist, H. Im, A. Kobyakov, and J. V. Moloney, “Plasmonic nano-structures for optical data storage,” *Opt. Express*, vol. 17, no. 16, pp. 14 001–14 014, Aug 2009. [Online]. Available: http://www.opticsexpress.org/abstract.cfm?URI=oe-17-16-14001

[5] E. H. Synge, “A suggested model for extending microscopic resolution into the ultra-microscopic region,” *Phil. Mag.*, vol. 6, pp. 356–362, 1928.

[6] E. A. Hawes, J. T. Hastings, C. Crofcheck, and M. P. Mengüç, “Spatially selective melting and evaporation of nanosized gold particles,” *Opt. Lett.*, vol. 33, no. 12, pp. 1383–1385, 2008.

[7] W. Whitten and H. Ross, “Time-of-flight optical spectroscopy with fiber optic waveguides,” *Quantum Electronics, IEEE Journal of*, vol. 15, no. 9, pp. 1025–1025, 1979.

[8] T. Vo-Dinh, B. M. Cullum, and D. L. Stokes, “Nanosensors and biochips: frontiers in biomolecular diagnostics,” *Sensors and Actuators B: Chemical*, vol. 74, no. 1–3, pp. 2 – 11, 2001, ¡ce:title¿Proceedings of the 5th European Conference on Optical Chemical Sensors and Biosensors¡/ce:title¿. [Online]. Available: http://www.sciencedirect.com/science/article/pii/S092540050000705X

[9] S. Lal, S. Link, and N. Halas, “Nano-optics from sensing to waveguiding,” *Nature Photonics*, vol. 1, pp. 641–648, November 2007.

[10] D.-K. Qing, I. Yamaguchi, K. Itoh, and M. Murabayashi, “Coupling-wave structures for optical waveguide sensors,” *Optical Review*, vol. 4, no. 5, pp. 578–583, 1997.

[11] J. Li and N. Engheta, “Core-shell nanowire optical antennas fed by slab waveguides,” *Antennas and Propagation, IEEE Transactions on*, vol. 55, no. 11, pp. 3018–3026, 2007.

[12] R. Zia, J. A. Schuller, A. Chandran, and M. L. Brongersma, “Plasmonics: the next chip-scale technology,” *Materials Today*, vol. 9, no. 7-8, pp. 20–27, 2006.

[13] R. L. Stiles, K. A. Willets, L. J. Sherry, J. M. Roden, and R. P. Van Duyne, “Investigating tip-nanoparticle interactions in spatially correlated total internal reflection plasmon spectroscopy and atomic force microscopy,” *The Journal of Physical Chemistry C*, vol. 112, no. 31, pp. 11 696–11 701, 2008.

[14] R. Hillenbrand, F. Keilmann, P. Hanarp, D. S. Sutherland, and J. Aizpurua, “Coherent imaging of nanoscale plasmon patterns with a carbon nanotube optical probe,” *Applied Physics Letters*, vol. 83, no. 2, pp. 368–370, jul 2003.

[15] M. W. Knight, Y. Wu, J. B. Lassiter, P. Nordlander, and N. J. Halas, “Substrates matter: Influence of an adjacent dielectric on an individual plasmonic nanoparticle,” *Nano Letters*, vol. 9, no. 5, pp. 2188–2192, 2009.

[16] C. E. Talley, J. B. Jackson, C. Oubre, N. K. Grady, C. W. Hollars, S. M. Lane, T. R. Huser, P. Nordlander, and N. J. Halas, “Surface-enhanced raman scattering from individual au nanoparticles and nanoparticle dimer substrates,” *Nano Letters*, vol. 5, no. 8, pp. 1569–1574, 2005. [Online]. Available: http://pubs.acs.org/doi/abs/10.1021/nl050928v

[17] P. G. Venkata, M. M. Aslan, and M. P. Mengüç, “Surface plasmon scattering by gold nanoparticles and two-dimensional agglomerates,” *Journal of Heat Transfer*, vol. 129, p. 60, January 2007.

[18] V. L. Y. Loke and M. P. Mengüç, “Surface waves and atomic force microscope probe-particle near-field coupling: discrete dipole approximation with surface interaction,” *Journal of the Optical Society of America A*, vol. 27, no. 10, October 2010.

[19] D. M. Schaadt, B. Feng, and E. T. Yu, “Enhanced semiconductor optical absorption via surface plasmon excitation in metal nanoparticles,” *Applied Physics Letters*, vol. 86, no. 6, p. 063106, 2005. [Online]. Available: http://link.aip.org/link/?APL/86/063106/1

[20] R. M. Roth, N. C. Panoiu, M. M. Adams, R. M. Osgood, C. C. Neacsu, and M. B. Raschke, “Resonant-plasmon field enhancement from asymmetrically illuminated conical metallic-probe tips,” *Opt. Express*, vol. 14, no. 7, pp. 2921–2931, Apr 2006. [Online]. Available: http://www.opticsexpress.org/abstract.cfm?URI=oe-14-7-2921

[21] X. Chen and X. Wang, “Near-field thermal transport in a nanotip under laser irradiation,” *Nanotechnology*, vol. 22, no. 7, p. 075204, 2011.

[22] P. L. Stiles, J. A. Dieringer, N. C. Shah, and R. P. Van Duyne, “Surface-enhanced raman spectroscopy,” *Annual Review of Analytical Chemistry*, vol. 1, no. 1, pp. 601–626, 2008.

[23] A. Rasmussen and V. Deckert, “Surface- and tip-enhanced raman scattering of dna components,” *Journal of Raman Spectroscopy*, vol. 37, no. 1-3, pp. 311–317, 2006. [Online]. Available: http://dx.doi.org/10.1002/jrs.1480

[24] Wikipedia. [Online]. Available: http://en.wikipedia.org/wiki

[25] A. Tseng, *Tip-Based Nanofabrication: Fundamentals and Applications*, ser. SpringerLink : Bücher. Springer New York, 2011. [Online]. Available: http://books.google.com/books?id=Y4pIHsPsI0YC

[26] B. Sensors, “Afm probe model tap 300ai-g,” ”http://www.budgetsensors.com/tapping_mode_afm_aluminium.html”.

[27] G. Mie, “Contributions on the optics of turbid media, particularly colloidal metal solutions,” *Annalen der Physik*, vol. IV, 25, no. 3, 1908.

[28] C. Balanis, *Antenna theory: analysis and design*, ser. Harper & Row series in electrical engineering. Wiley, 1982. [Online]. Available: http://books.google.com/books?id=wARTAAAAMAAJ

[29] W. Chew, M. Tong, and B. Hu, *Integral Equation Methods for Electromagnetic and Elastic Waves*, ser. Synthesis Lectures on Computational Electromagnetics Series. Morgan & Claypool Publishers, 2009. [Online]. Available: http://books.google.com/books?id=PJN9meadzT8C

[30] R. G. Martin, *Electromagnetic field theory for physicists and engineers: Fundamentals and Applications*. Universidad de Granada, 2009.

[31] S. Gedney, *Introduction to the Finite-Difference Time-Domain (Fdtd) Method for Electromagnetics*, ser. Synthesis Lectures on Computational Electromagnetics Series. Morgan & Claypool, 2011. [Online]. Available: http://books.google.com/books?id=sdwbsMAztKIC

[32] J. Renger, S. Grafström, L. M. Eng, and V. Deckert, “Evanescent wave scattering and local electric field enhancement at ellipsoidal silver particles in the vicinity of a glass surface,” *J. Opt. Soc. Am. A*, vol. 21, no. 7, pp. 1362–1367, Jul 2004. [Online]. Available: http://josaa.osa.org/abstract.cfm?URI=josaa-21-7-1362

[33] B. Saleh and M. Teich, *Fundamentals of Photonics*, ser. Wiley Series in Pure and Applied Optics. Wiley, 2007. [Online]. Available: http://books.google.com/books?id=Ve8eAQAAIAAJ

[34] S. Maier, *Plasmonics: Fundamentals and Applications*. Springer, 2007. [Online]. Available: http://books.google.com/books?id=yT2ux7TmDc8C

[35] U. Kreibig and M. Vollmer, *Optical properties of metal clusters*, ser. Springer series in materials science. Springer, 1995, no. v. 25. [Online]. Available: http://books.google.com/books?id=jYhRAAAAMAAJ

[36] C. F. Bohren and D. R. Huffman, *Absorption and Scattering of Light by Small Particles*. John Wiley and Sons, 1983.

[37] P. B. Johnson and R. W. Christy, “Optical constants of the noble metals,” *Physical Review B*, vol. 6, no. 12, p. 4370, 1972, copyright (C) 2011 The American Physical Society Please report any problems to prolaaps.org PRB.

[38] A. Trügler, *Optical Properties of Metallic Nanoparticles: Basic Principles and Simulation*. Springer, 2014.

[39] E. Hecht, *Optics*, 4th ed. Addison-Wesley, 2002.

[40] M. Fox, *Optical Properties of Solids*, ser. Oxford Master Series in Condensed Matter Physics. Oxford University Press, USA, 2002. [Online]. Available: http://books.google.com/books?id=-5bVBbAoaGoC

[41] K. A. Willets and R. P. Van Duyne, "Localized surface plasmon resonance spectroscopy and sensing," *Annual Review of Physical Chemistry*, vol. 58, no. 1, pp. 267–297, 2007. [Online]. Available: http://www.annualreviews.org/doi/abs/10.1146/annurev.physchem.58.032806.104607

[42] H. A. Atwater and A. Polman, "Plasmonics for improved photovoltaic devices," *Nat Mater*, vol. 9, no. 3, pp. 205–213, 03 2010. [Online]. Available: http://dx.doi.org/10.1038/nmat2629

[43] S. H. Lim, W. Mar, P. Matheu, D. Derkacs, and E. T. Yu, "Photocurrent spectroscopy of optical absorption enhancement in silicon photodiodes via scattering from surface plasmon polaritons in gold nanoparticles," *Journal of Applied Physics*, vol. 101, no. 10, p. 104309, 2007. [Online]. Available: http://link.aip.org/link/?JAP/101/104309/1

[44] P. Prasad, *Nanophotonics*. Wiley, 2004. [Online]. Available: http://books.google.com/books?id=wc7l8rBumg0C

[45] B. McCarthy, Y. Zhao, R. Grover, and D. Sarid, "Enhanced raman scattering for temperature measurement of a laser-heated atomic force microscope tip," *Applied Physics Letters*, vol. 86, no. 11, p. 111914, 2005. [Online]. Available: http://link.aip.org/link/?APL/86/111914/1

[46] R. C. Maher, L. F. Cohen, J. C. Gallop, E. C. Le Ru, and P. G. Etchegoin, "Temperature-dependent anti-stokes/stokes ratios under surface-enhanced raman scattering conditions," *The Journal of Physical Chemistry B*, vol. 110, no. 13, pp. 6797–6803, 2006, pMID: 16570987. [Online]. Available: http://pubs.acs.org/doi/abs/10.1021/jp056466r

[47] C. D. S. Brites, P. P. Lima, N. J. O. Silva, A. Millan, V. S. Amaral, F. Palacio, and L. D. Carlos, "Thermometry at the nanoscale," *Nanoscale*, vol. 4, pp. 4799–4829, 2012. [Online]. Available: http://dx.doi.org/10.1039/C2NR30663H

[48] W. Murray and W. Barnes, "Plasmonic materials," *Advanced Materials*, vol. 19, no. 22, pp. 3771–3782, 2007. [Online]. Available: http://dx.doi.org/10.1002/adma.200700678

[49] J. Parsons, C. P. Burrows, J. R. Sambles, and W. L. Barnes, "comparison of techniques used to simulate the scattering of electromagnetic radiation by metallic nanostructures." *Journal of Modern Optics*, vol. 57, no. 5, pp. 356–365, 2010.

[50] T. Wriedt, *Generalized multipole techniques for electromagnetic and light scattering*. Elsevier, 1999.

[51] J. Bladel, *Electromagnetic fields*, ser. IEEE Press series on electromagnetic wave theory. Wiley-Interscience, 2007. [Online]. Available: http://books.google.com/books?id=1tPotI3DJuEC

[52] T. Rhee, *Advanced study of the method of moment distribution*. Kansas State University, 1967. [Online]. Available: http://books.google.com/books?id=9tXGNwAACAAJ

[53] C. Guardasoni, *Wave Propagation Analysis with Boundary Element Method*. Ledizioni, 2010. [Online]. Available: http://books.google.com/books?id=NeS83ABwOw4C

[54] V. Loke, E. U. Donev, G. M. Huda, J. T. Hastings, M. P. Mengüç, and T. Wriedt, "Discrete dipole aproximation of gold nanospheres on substrates: Considerations and comparision with other discretization methods," *AAPP — Physical, Mathematical, and Natural Sciences*, vol. 89, no. S1, 2011.

[55] M. Sukharev and T. Seideman, "Optical properties of metal tips for tip-enhanced spectroscopies," *The Journal of Physical Chemistry A*, vol. 113, no. 26, pp. 7508–7513, 2009, pMID: 19354241. [Online]. Available: http://pubs.acs.org/doi/abs/10.1021/jp900877m

[56] J. Muller, G. Parent, S. Fumeron, G. Jeandel, and D. Lacroix, "Near-field and far-field modeling of scattered surface waves. application to the apertureless scanning near-field optical microscopy," *Journal of Quantitative Spectroscopy and Radiative Transfer*, vol. 112, no. 7, pp. 1162 – 1169, 2011, ¡ce:title¿Sixth International Symposium on Radiative Transfer¡/ce:title¿. [Online]. Available: http://www.sciencedirect.com/science/article/pii/S0022407310003407

[57] I. Notingher and A. Elfick, "Effect of sample and substrate electric properties on the electric field enhancement at the apex of spm nanotips," *The Journal of Physical Chemistry B*, vol. 109, no. 33, pp. 15 699–15 706, 2005. [Online]. Available: http://pubs.acs.org/doi/abs/10.1021/jp0523120

[58] M. Micic, N. Klymyshyn, Y. D. Suh, and H. P. Lu, "Finite element method simulation of the field distribution for afm tip-enhanced surface-enhanced raman scanning microscopy," *The Journal of Physical Chemistry B*, vol. 107, no. 7, pp. 1574–1584, 2003. [Online]. Available: http://pubs.acs.org/doi/abs/10.1021/jp022060s

[59] J. Jin, *The Finite Element Method in Electromagnetics*, 2nd ed. John Wiley and Sons, 2002.

[60] T. Grosges, A. Vial, and D. Barchiesi, "Models of near-field spectroscopic studies: comparison between finite-element and finite-difference methods," *Opt. Express*, vol. 13, no. 21, pp. 8483–8497, Oct 2005. [Online]. Available: http://www.opticsexpress.org/abstract.cfm?URI=oe-13-21-8483

[61] D. W. Mackowski, "A generalization of image theory to predict the interaction of multipole fields with plane surfaces," *Journal of Quantitative Spectroscopy and Radiative Transfer*, vol. 111, no. 5, pp. 802 – 809, 2010. [Online]. Available: http://www.sciencedirect.com/science/article/B6TVR-4XSJVXC-2/2/9d8ff1f7079a704b0025c2ee0e09cb32

[62] B. T. Draine, "The discrete-dipole approximation and its application to interstellar graphite grains," *Astrophysical Journal Part 1*, vol. 333, pp. 848–872, Oct 1988.

[63] V. L. Loke, M. P. Mengüç, and T. A. Nieminen, "Discrete dipole approximation with surface interaction: Computational toolbox for matlab," *Journal of Quantitative Spectroscopy and Radiative Transfer*, vol. In Press, Corrected Proof, 2011.

[64] V. Loke, G. Huda, E. Donev, V. Schmidt, J. Hastings, M. Mengüç, and T. Wriedt, "Comparison between discrete dipole approximation and other modelling methods for the plasmonic response of gold nanospheres," *Applied Physics B*, pp. 1–10, 2013, submitted for peer review.

[65] S. Link, C. Burda, B. Nikoobakht, and M. A. El-Sayed, "Laser-induced shape changes of colloidal gold nanorods using femtosecond and nanosecond laser pulses," *The Journal of Physical Chemistry B*, vol. 104, no. 26, pp. 6152–6163, 2000. [Online]. Available: http://pubs.acs.org/doi/abs/10.1021/jp000679t

[66] O. Ekici, R. K. Harrison, N. J. Durr, D. S. Eversole, M. Lee, and A. Ben-Yaker, "Thermal analysis of gold nanorods heated with femtosecond laser pulses," *Journal of Physics D Applied Physics*, vol. 41, no. 185501, p. 11, August 2008.

[67] A. Verma, Y. Prajapati, S. Ayub, J. Saini, and V. Singh, “Analytical analysis of sensitivity of optical waveguide sensor,” *International Journal of Engineering, Science and Technology*, vol. 3, no. 3, pp. 36–40, 2011.

[68] A. Yimit, A. G. Rossberg, T. Amemiya, and K. Itoh, “Thin film composite optical waveguides for sensor applications: a review,” *Talanta*, vol. 65, no. 5, pp. 1102 – 1109, 2005, ¡ce:title¿Optical waveguide analysis¡/ce:title¿. [Online]. Available: http://www.sciencedirect.com/science/article/pii/S003991400400596X

[69] J. Dostálek, J. Čtyroký, J. Homola, E. Brynda, M. Skalský, P. Nekvindová, J. Špirková, J. Škvor, and J. Schröfel, “Surface plasmon resonance biosensor based on integrated optical waveguide,” *Sensors and Actuators B: Chemical*, vol. 76, no. 1-3, pp. 8–12, 2001.

[70] U. K. Chettiar, R. F. Garcia, S. A. Maier, and N. Engheta, “Enhancement of radiation from dielectric waveguides using resonant plasmonic coreshells,” *Opt. Express*, vol. 20, no. 14, pp. 16 104–16 112, Jul 2012. [Online]. Available: http://www.opticsexpress.org/abstract.cfm?URI=oe-20-14-16104

[71] L. Arnaud, A. Bruyant, M. Renault, Y. Hadjar, R. Salas-Montiel, A. Apuzzo, G. Lérondel, A. Morand, P. Benech, E. L. Coarer, and S. Blaize, “Waveguide-coupled nanowire as an optical antenna,” *J. Opt. Soc. Am. A*, vol. 30, no. 11, pp. 2347–2355, Nov 2013.

[72] A. Yaacobi and M. R. Watts, “Frequency-chirped subwavelength nanoantennas,” *Opt. Lett.*, vol. 37, no. 23, pp. 4979–4981, Dec 2012. [Online]. Available: http://ol.osa.org/abstract.cfm?URI=ol-37-23-4979

[73] H. C. Hulst, *Light Scattering by Small Particles*. Dover Publications, Inc, 1981.

[74] N. Nehru, E. U. Donev, G. M. Huda, L. Yu, Y. Wei, and J. T. Hastings, “Differentiating surface and bulk interactions using localized surface plasmon resonances of gold nanorods,” *Opt. Express*, vol. 20, no. 7, pp. 6905–6914, Mar 2012. [Online]. Available: http://www.opticsexpress.org/abstract.cfm?URI=oe-20-7-6905

[75] S. Berweger, J. M. Atkin, R. L. Olmon, and M. B. Raschke, “Adiabatic tip-plasmon focusing for nano-raman spectroscopy,” *The Journal of Physical Chemistry Letters*, vol. 1, no. 24, pp. 3427–3432, 2010. [Online]. Available: http://pubs.acs.org/doi/abs/10.1021/jz101289z

[76] N. Mishra and G. V. P. Kumar, “Near-field optical analysis of plasmonic nano-probes for top-illumination tip-enhanced raman scattering,” *Plasmonics*, vol. 7, no. 2, pp. 359–367, June 2012.

[77] R. Esteban, R. Vogelgesang, and K. Kern, “Full simulations of the apertureless scanning near field optical microscopy signal: achievable resolution and contrast,” *Opt. Express*, vol. 17, no. 4, pp. 2518–2529, Feb 2009. [Online]. Available: http://www.opticsexpress.org/abstract.cfm?URI=oe-17-4-2518

[78] R. Fikri, T. Grosges, and D. Barchiesi, “Apertureless scanning near-field optical microscopy: numerical modeling of the lock-in detection,” *Optics Communications*, vol. 232, no. 1-6, pp. 15 – 23, 2004. [Online]. Available: http://www.sciencedirect.com/science/article/B6TVF-4B9DDTH-4/2/d8714f0c0f9cb08aab72930383afaadc

[79] D. Sadiq, J. Shirdel, J. S. Lee, E. Selishcheva, N. Park, and C. Lienau, "Adiabatic nanofocusing scattering-type optical nanoscopy of individual gold nanoparticles," *Nano Letters*, vol. 0, no. 0, 0. [Online]. Available: http://pubs.acs.org/doi/abs/10.1021/nl1045457

[80] M. Quinten, "Evanescent wave scattering by aggregates of clusters – application to optical near-field microscopy," *Applied Physics B: Lasers and Optics*, vol. 70, pp. 579–586, 2000, 10.1007/s003400050865. [Online]. Available: http://dx.doi.org/10.1007/s003400050865

[81] S. Benrezzak, P. M. Adam, J. L. Bijeon, and P. Royer, "Observation of nanometric metallic particles with an apertureless scanning near-field optical microscope," *Surface Science*, vol. 491, no. 1–2, pp. 195 – 207, 2001. [Online]. Available: http://www.sciencedirect.com/science/article/pii/S0039602801014042

[82] X. Hong, W. Xu, X. Li, C. Zhao, and X. Tang, "Field enhancement effect of metal probe in evanescent field," *Chin. Opt. Lett.*, vol. 7, no. 1, pp. 74–77, Jan 2009. [Online]. Available: http://col.osa.org/abstract.cfm?URI=col-7-1-74

[83] J. Homola, *Surface Plasmon Resonance Based Sensors*, ser. Springer Series on Chemical Sensors And Biosensors. Springer, 2006. [Online]. Available: http://books.google.com/books?id=Lhd_JVZW7D0C

[84] J. Zuloaga, E. Prodan, and P. Nordlander, "Quantum description of the plasmon resonances of a nanoparticle dimer," *Nano Letters*, vol. 9, no. 2, pp. 887–891, 2009, pMID: 19159319. [Online]. Available: http://pubs.acs.org/doi/abs/10.1021/nl803811g

[85] F. Fornel, *Evanescent waves: from Newtonian optics to atomic optics*, ser. Springer series in optical sciences. Springer, 2001. [Online]. Available: http://books.google.com/books?id=-Eklx2aMY5AC

[86] G. M. Huda, E. U. Donev, M. P. Mengüç, and J. T. Hastings, "Effects of a silicon probe on gold nanoparticles on glass under evanescent illumination," *Opt. Express*, vol. 19, no. 13, pp. 12 679–12 687, Jun 2011. [Online]. Available: http://www.opticsexpress.org/abstract.cfm?URI=oe-19-13-12679

[87] W.-S. Chang, B. A. Willingham, L. S. Slaughter, B. P. Khanal, L. Vigderman, E. R. Zubarev, and S. Link, "Low absorption losses of strongly coupled surface plasmons in nanoparticle assemblies," *Proceedings of the National Academy of Sciences*, vol. 108, no. 50, pp. 19 879–19 884, 2011. [Online]. Available: http://www.pnas.org/content/108/50/19879.abstract

[88] M. A. Kats, N. Yu, P. Genevet, Z. Gaburro, and F. Capasso, "Effect of radiation damping on the spectral response of plasmonic components," *Opt. Express*, vol. 19, no. 22, pp. 21 748–21 753, Oct 2011. [Online]. Available: http://www.opticsexpress.org/abstract.cfm?URI=oe-19-22-21748

[89] C. Dahmen, B. Schmidt, and G. von Plessen, "Radiation damping in metal nanoparticle pairs," *Nano Letters*, vol. 7, no. 2, pp. 318–322, 2007. [Online]. Available: http://pubs.acs.org/doi/abs/10.1021/nl062377u

[90] C. Kumar, *Raman Spectroscopy for Nanomaterials Characterization*. Springer, 2012. [Online]. Available: http://books.google.com/books?id=Ptr6e2GnbTIC

[91] X. Chen and X. Wang, "Near-field thermal transport in a nanotip under laser irradiation," *Nanotechnology*, vol. 22, no. 7, p. 075204, 2011. [Online]. Available: http://stacks.iop.org/0957-4484/22/i=7/a=075204

[92] Y. Yue, X. Chen, and X. Wang, "Noncontact sub-10 nm temperature measurement in near-field laser heating," *ACS Nano*, vol. 5, no. 6, pp. 4466–4475, 2011. [Online]. Available: http://pubs.acs.org/doi/abs/10.1021/nn2011442

[93] D. Sarid, B. McCarthy, and R. Grover, "Scanning thermal-conductivity microscope," *Review of Scientific Instruments*, vol. 77, no. 2, pp. 023 703 –023 703–7, Feb 2006.

[94] C. Multiphysics. (2008) Rf module user's guide. [Online]. Available: www.comsol.com

[95] A. Optics, "Schott," "http://www.us.schott.com/advanced_optics/english/download/schott_optical_glass_jan_2011_us.pdf", 2011.

[96] E. Palik and G. Ghosh, *Handbook of optical constants of solids: five-volume set*, ser. Academic Press Handbook. Academic Press, 1998, no. v. 4. [Online]. Available: http://books.google.com/books?id=VpuVttd2cuEC

[97] H. Haus, *Waves and fields in optoelectronics*, ser. Prentice-Hall Series in Solid State Physical Electronics. Prentice Hall, Incorporated, 1984. [Online]. Available: http://books.google.com/books?id=AQUpAQAAMAAJ

[98] A. Yariv and P. Yeh, *Photonics: Optical Electronics in Modern Communications*, ser. The Oxford Series in Electrical and Computer Engineering. Oxford University Press, Incorporated, 2007. [Online]. Available: http://books.google.com/books?id=B2xwQgAACAAJ

[99] W. H. Weber and G. W. Ford, "Optical electric-field enhancement at a metal surface arising from surface-plasmon excitation," *Opt. Lett.*, vol. 6, no. 3, pp. 122–124, Mar 1981. [Online]. Available: http://ol.osa.org/abstract.cfm?URI=ol-6-3-122

[100] A. Vial and T. Laroche, "Comparison of gold and silver dispersion laws suitable for fdtd simulations," *Applied Physics B: Lasers and Optics*, vol. 93, pp. 139–143, 2008, 10.1007/s00340-008-3202-4. [Online]. Available: http://dx.doi.org/10.1007/s00340-008-3202-4

[101] Sellmeier, "Zur erklärung der abnormen farbenfolge im spectrum einiger substanzen," *Annalen der Physik*, vol. 219, no. 6, pp. 272–282, 1871. [Online]. Available: http://dx.doi.org/10.1002/andp.18712190612

[102] R. Luebbers, F. Hunsberger, K. Kunz, R. Standler, and M. Schneider, "A frequency-dependent finite-difference time-domain formulation for dispersive materials," *Electromagnetic Compatibility, IEEE Transactions on*, vol. 32, no. 3, pp. 222–227, Aug 1990.

[103] G. M. Huda, "Effect of a silicon tip on absorption cross section, field enhancement, and localized surface plasmon resonance of different sized gold nanoparticles under evanescent wave illumination," Master's thesis, University Of Kentucky, May 2011.

[104] MATLAB, *MATLAB: 2011*. The MathWorks Inc., 2011.

[105] J. Zuloaga and P. Nordlander, "On the energy shift between near-field and far-field peak intensities in localized plasmon systems," *Nano Letters*, vol. 11, no. 3, pp. 1280–1283, 2011. [Online]. Available: http://pubs.acs.org/doi/abs/10.1021/nl1043242

[106] M. Duval Malinsky, K. L. Kelly, G. C. Schatz, and R. P. Van Duyne, "Nanosphere lithography: effect of substrate on the localized surface plasmon resonance spectrum of silver nanoparticles," *The Journal of Physical Chemistry B*, vol. 105, no. 12, pp. 2343–2350, 2001. [Online]. Available: http://pubs.acs.org/doi/abs/10.1021/jp002906x

[107] W. Chen, A. Kimel, A. Kirilyuk, and T. Rasing, "Apertureless snom study on gold nanoparticles: Experiments and simulations," *physica status solidi (b)*, vol. 247, no. 8, pp. 2047–2050, 2010. [Online]. Available: http://dx.doi.org/10.1002/pssb.200983940

[108] M. J. Khan, "Integrated optical filters using bragg gratings and resonators," Ph.D. dissertation, Massachusetts Institute of Technology, 2002.

[109] A. J. Haes and R. P. Van Duyne, "A unified view of propagating and localized surface plasmon resonance biosensors," *Analytical and Bioanalytical Chemistry*, vol. 379, pp. 920–930, 2004, 10.1007/s00216-004-2708-9. [Online]. Available: http://dx.doi.org/10.1007/s00216-004-2708-9

[110] T. Wriedt. Light scattering information portal. [Online]. Available: http://www.scattport.org/index.php/scattport-page-information

[111] A. Doicu, Y. Eremin, and T. Wriedt, "Convergence of the t-matrix method for light scattering from a particle on or near a surface," *Optics Communications*, vol. 159, no. 4–6, pp. 266 – 277, 1999. [Online]. Available: http://www.sciencedirect.com/science/article/pii/S0030401898005860

[112] P. K. Jain, K. S. Lee, I. H. El-Sayed, and M. A. El-Sayed, "Calculated absorption and scattering properties of gold nanoparticles of different size, shape, and composition: applications in biological imaging and biomedicine," *The Journal of Physical Chemistry B*, vol. 110, no. 14, pp. 7238–7248, 2006, pMID: 16599493. [Online]. Available: http://pubs.acs.org/doi/abs/10.1021/jp057170o

VITA

Gazi M. Huda was born in Dhaka, Bangladesh. He earned his B.Sc. in Electrical and Electronic Engineering (EEE) from Bangladesh university of engineering and technology (BUET), Dhaka in 2008, and M.S. in Electrical Engineering (EE) from University of Kentucky (UK), Lexington in 2011. His MS thesis was nominated by UK to compete at the Conference of Southern Graduate School in Math, Physical science and Engineering category.

In 2009, he started his graduate school, being appointed as a Teaching Assistant in the department of electrical and computer engineering (ECE), and joined Hastings Research Group in 2010. He received the Harrison D. Brailsford Graduate Fellowship from the College of Engineering and the Research Challenge Trust Fund Fellowship from the ECE dept. of UK, and nominated by the DGS to compete for the Dissertation year fellowship for his achievements as a Graduate Research Assistant in 2011. Before coming to the United States, Gazi was appointed as a lecturer at a private college, Presidency University in Dhaka. Currently, he is an intern in the ANSYS Signal Integrity Research and Development at Pittsburgh.

Mr. Huda is a student member of the Institute of Electrical and Electronic Engineerings (IEEE) and Kentucky Society of Professional Engineers (KSPE).

Journal articles:

- G. Huda and J. Hastings, *Absorption modulation of plasmon resonant nanoparticles in the presence of an AFM tip*, Huda, G.; Hastings, T.; Selected Topics in Quantum Electronics, IEEE Journal of , vol. PP, no. 99, pp. 1, 0
- G. Huda, E. Donev, M. Mengüç, and J. Hastings, *Effects of a silicon probe on gold nanoparticles on glass under evanescent illumination*, Opt. Express 19, 12679-12687 (2011)
- V.L.Y. Loke, G.M. Huda, E. U. Donev, V. Schmidt, J. T. Hastings, M. P. Mengüç, and T. Wriedt. *Comparison between discrete dipole approximation and other modeling methods for the plasmonic response of gold nanospheres,* Applied Physics B: Lasers and Optics (2013)

- N. Nehru, E. Donev, G. Huda, L. Yu, Y. Wei, and J. Hastings, *Differentiating surface and bulk interactions using localized surface plasmon resonances of gold nanorods*, Opt. Express 20, 6905-6914 (2012)

Conference papers:

- G. Huda and J. Hastings, *Gold nanoparticle absorption under a nanoscale tip illuminated by surface-plasmon polaritons*, Proc. SPIE 8619, Physics and Simulation of Optoelectronic Devices XXI, 86191F (March 14, 2013)

- G. Huda and J. Hastings, *Absorption suppression of silver nanoparticles in the presence of an AFM tip: a harmonic oscillator model*, AIP Conf. Proc. 1475, pp. 134-136

- V.L.Y. Loke, E. U. Donev, G.M. Huda, J. T. Hastings, M. P. Mengüç, and T. Wriedt. *Discrete dipole approximation of gold nanosphere on substrates: Considerations and comparison with other discretization method*, AAPP Vol 89, Supplement No 1 (2011); ELS XIII Conference